

Dissertation

submitted to the
Combined Faculty of Natural Sciences and Mathematics
of **Heidelberg University**, Germany
for the degree of
Doctor of Natural Sciences

put forward by

Farshad Shobeiry

born in Tehran (Iran)

Oral examination: 2 February, 2021

Attosecond Electron-Nuclear Dynamics in Photodissociation of H₂ and D₂

Referees:

Priv.-Doz. Dr. Robert Moshhammer

Prof. Dr. Andreas Wolf

Abstract - In this work the dynamics of molecular hydrogen (H_2) and molecular deuterium (D_2) are investigated in a series of kinematically complete experiments on an attosecond time scale using the RABBIT technique. To achieve this, a high-repetition rate attosecond beamline has been designed and constructed. A Mach-Zehnder interferometer configuration is used to perform pump-probe XUV+IR experiments with the help of a sub-8-fs 150-kHz fiber laser to produce XUV light using high harmonic generation. The beamline is combined with a state-of-the-art reaction microscope and coincident electron and ion detection is used to uncover the molecular fragmentation dynamics. The electron localization in the molecular frame of reference in photo-dissociation of H_2 and D_2 is demonstrated. A semi-classical simulation supports the observed phenomena. The localization of the electron can be manipulated by the number of absorbed photons in the system as well as the delay between the pump and probe pulses. Moreover, phases of the electronic wavepackets in the vicinity of resonant doubly-excited states are extracted, and isotope effects are presented.

Zusammenfassung. In dieser Arbeit wird die Dynamik von molekularem Wasserstoff (H_2) und molekularem Deuterium (D_2) in einer Reihe von kinematisch vollständigen Experimenten auf der Attosekunden-Zeitskala mithilfe des RABBIT-Verfahrens untersucht. Zu diesem Zweck wurde eine Attosekunden-Beamline mit hoher Repetitionsrate aufgebaut. Ein Mach-Zehnder-Interferometer wird zur Durchführung von Pump-Probe (XUV+IR) Experimenten mithilfe eines 150-kHz-Faserlasers (Pulsdauer < 8-fs) verwendet, um XUV-Licht mit hohen harmonischen Strahlung zu erzeugen. Die Beamline ist mit einem hochmodernen Reaktionsmikroskop kombiniert. Zur Aufdeckung der molekularen Fragmentationsdynamik werden Ionen und Elektronen koinzident detektiert. Die Elektronenlokalisierung im molekularen Bezugssystem bei der Photodissoziation von H_2 und D_2 wird demonstriert. Eine halbklassische Simulation unterstützt die beobachteten Phänomene. Die Lokalisierung des Elektrons kann durch die Anzahl der absorbierten Photonen im System sowie durch die Verzögerung zwischen Pump- und Probepuls manipuliert werden. Darüber hinaus werden Phasen der elektronischen Wellenpakete in der Nähe von resonanten, doppelt angeregten Zuständen extrahiert und Isotopeneffekte beobachtet.

Contents

1	Introduction	1
2	Interaction of Atoms with Light	5
2.1	Atoms in Strong Light Fields and High Harmonic Generation	5
2.1.1	High Harmonic Generation (HHG)	6
2.1.2	Phase of HHG	8
2.1.3	Macroscopic Properties of High Harmonic Generation	8
2.1.4	Attosecond pulse trains (APT)	9
2.2	Single-Photon ionization using XUV light	10
2.2.1	Attosecond photoelectron interferometry	12
3	Hydrogen Molecule	17
3.1	The Born-Oppenheimer Approximation	17
3.2	Molecular Time Scale	19
3.3	Molecular Orbital and Electronic States Nomenclature	19
3.4	Symmetry, Group Theory, and Selection Rules	20
3.5	The Franck-Condon principle	24
3.6	WKB Approximation	25
3.7	The Floquet Picture (Laser-Dressed Molecular Potentials)	26
3.7.1	Bond Softening, Hardening and above-threshold dissociation	27
3.8	Electron Localization	29
4	Experimental Setup	33
4.1	Laser System	33
4.2	Interferometer	33
4.2.1	High-Harmonic Generation (HHG)	38
4.3	Reaction Microscope	40
4.3.1	Supersonic Gas Target	40
4.3.2	Spectrometer and Detectors	41
4.3.3	Momentum Reconstruction	44
4.3.4	Spectrometer Acceptance	47
4.3.5	Momentum Resolution	47
4.3.6	Molecular Frame	48

5	Nuclear-Electron related Dynamics of H₂ and D₂	51
5.1	Single-photon Ionization of H ₂ and D ₂	54
5.2	Photodissociation of H ₂ and D ₂	60
5.2.1	Photo-dissociation of H ₂ and D ₂ with an Attosecond Pulse Train . .	61
5.2.2	Direct Dissociation	63
5.2.3	Indirect Dissociation	65
5.2.4	The Role of IR Probe	70
5.3	Vibrationally-resolved dissociation of H ₂ and D ₂ using XUV+IR	73
5.4	RABBIT in H ₂ and D ₂	78
5.4.1	Ground State Dissociation vs Bond Softening	80
5.4.2	Phase of the photo-electron wave-packet in the vicinity of Autoion- izing states	82
6	Electron Localization	89
6.1	Molecular-Frame Asymmetry	90
6.1.1	The Physical Origin of Asymmetry	93
6.2	Semi-Classical Simulation of Electron Localization	98
6.3	Probe Beam Intensity Dependence	101
6.4	Attosecond time-resolved electron Asymmetry	102
6.5	Previous Measurements and Discussion	105
7	Summary and Outlook	107
	Appendices	109
A	Atomic Units	111
B	H₂⁺ and D₂⁺ spectroscopic values	113
C	Raw data	117
D	Fit procedure and Error bars	121
E	Toroidal mirror	123
F	Bandwidth of Doubly-excited states	125
	Bibliography	129

Chapter 1

Introduction

There has been an exponential jump in our knowledge in molecular dynamics with the advent of femto- and attosecond science [1]. This field was initiated with the pioneering work of Ahmed Zewail, who observed the molecular motion in real time for the first time [2][3]. The focus of femtochemistry science is to understand the dynamics of chemical reactions, and ultimately to manipulate the break-up or formation of molecular systems [4]. However, molecular dynamics are governed by electrons which move much faster than nuclei due to their mass difference (three orders of magnitude) [5]. For instance, the period of the orbiting electron in the lowest orbital of the hydrogen atom is approximately 150 attoseconds (1 attosecond = 10^{-18}). With the observation of a train of attosecond pulses in 2001, using high harmonic generation [6], scientists could break time resolution barriers in femtochemistry. Shortly after, electron motion in real time was observed [7][8]. The process of high-harmonic generation (HHG) is a useful tool to study soft-X-ray interaction with matter. The low conversion efficiency of HHG demands higher-repetition laser systems in order to perform coincidence measurements with reasonable signal-to-noise ratio [9]. Up until now, Ti-Sapphire laser systems (mostly based on mode locking [37]) were the workhorse of femtosecond pulse generation with the repetition rate in a few kilohertz regime and mJ pulse energy [10]. There has been effort recently to overcome the repetition rate and pulse energy limitations using disk [11], and fiber lasers [12].

The investigation of light-matter interaction benefits significantly from imaging of the momenta of fragments. Had it not been for sophisticated spectroscopy techniques [13], the field of femto-, and attosecond science would not be where it is today. The commonly used reaction microscope (ReMi) or cold-target recoil-ion momentum spectroscopy technique (COLTRIMS) provides very rich information regarding ultrafast dynamics by providing the detection of the 3D momentum distributions of particles in coincidence [14]. By the virtue of a supersonic gas expansion, a cold and well-collimated beam of molecules or atoms interacts with a laser beam at the center of the ReMi. The produced charged fragments are steered in the presence of an electrostatic field towards position-sensitive

detectors for both negative and positive charged particles on two sides where they can be detected in coincidence. A better spatial confinement for electrons is achieved with the use of a weak magnetic field produced by Helmholtz coils around the spectrometer.

The hydrogen molecule (H_2) is the simplest neutral and the most abundant molecule in the universe. Since it is the only molecule which can be fully investigated in theory, it has become a benchmark molecular system [15]. H_2 has also the strongest isotope effect: no other molecule can double its mass by adding an additional neutron to it. Therefore, investigating H_2 and D_2 (2H_2) side by side provides a deeper understanding into these molecular systems. Additionally, H_2 has the fastest vibrational dynamics which makes it a perfect candidate for the investigation of electron-nuclear correlation. Dissociative photo-ionization of H_2 has been the subject of extensive studies [16]. Not only is it of great theoretical interest, it is also important in interstellar and planetary atmospheres [17]. Generally photo-dissociation can be explained in three stages. A photon is absorbed during the first stage, and the molecule is promoted to an excited state (either electronic or vibrationally-highly-excited state in the ground electronic state). During the second stage, the system evolves through series of transition states, and finally, the molecule dissociates into fragments [18].

Another important aspect in photodissociation is the presence of the doubly-excited states in H_2 , which have repulsive potential curves. They can dissociate into neutral ($H + H$) or ionic ($H^+ + H^-$) fragments or autoionize either non-dissociatively ($H_2^{**} \rightarrow H_2^+ + e^-$) or dissociatively ($H_2^{**} \rightarrow H + H_2^+ + e^-$). The dynamics of doubly-excited states is very challenging as far as the theory is concerned. This is due to the fact that a full quantum mechanical treatment of a four-body system is needed [19]. In addition, the lifetime of autoionizing states is of the same order of magnitude as the vibrational period of the nuclei, which makes it even more complicated. Yet, exploring the dissociative photo-ionization helps scientists uncover light-matter interaction on a deeper level since the detected ion and electrons in coincidence as products of dissociation makes it possible to determine the orientation of the molecule at the time of ionization. The photo-dissociation cross section, however, is very small, increasing drastically the acquisition time of the measurement.

Time-resolved pump-probe measurements should be done to gain more insight into molecular dynamics. The goal of the probe pulse is to project the real-time state of the system in question into observables which are accessible by the detection system. The time resolution improves with the pulse length of the pump and probe. On the other hand, the shorter the pulses become, the broader is the energy spectrum of those pulses which can cause ambiguities in states under investigation [20]. There are, however relatively few time-resolved measurements in molecules compared to atoms because of the complexities added by the nuclear motion.

This work has combined time-resolved measurements in its most sophisticated form, so far, so as to study dissociative dynamics in H_2 and D_2 . To this end, an attosecond

beamline, known as Attolab, has been designed and constructed in a combination with a high-repetition fiber laser and a ReMi. In the first part of this thesis, the interaction between an APT and H_2 and D_2 shows how the energy of the photon is distributed among the fragments of the dissociation, and how this energy distribution differs when a long (50 fs) and weak IR dressing field (with the intensity in the order of $10^{11} W/cm^2$) is added. The strongest feature is the presence of bond softening, which occurs when a photon couples the ground state of the molecular ion to the first excited state of that molecular ion [21][22][23]. As a result of bond softening one can resolve the vibrational levels of the cation (H_2^+) by detecting H^+ fragments after dissociation. Moreover, dissociative ionization of H_2 and D_2 shows strong coupled electron-nuclear dynamics on an attosecond timescale which can be uncovered using a conventional technique for electron interferometry, known as RABBIT (Reconstruction of Attosecond Beating By Interference of Two-photon transitions) [24][25][6]. This technique was initially used to characterize an APT by measuring the chirp (photon group delay derivative). Shortly after, observation of electron delays during photoionization became feasible using RABBIT [26][27]. In addition, one can investigate the behaviour of a photoelectron wavepacket near resonant states using this technique [28][29]. Although there are numerous examples in atomic system, there are very few measurements done on molecules [30][31][32][33][34]. In this work, the RABBIT technique is used to investigate the phase of photoelectrons near the autoionizing resonances in a side-by-side manner in both H_2 and D_2 for the first time and striking isotope effects are presented.

In the second part of this work, an interesting symmetry breaking in the electron localization in the most simple molecular systems (H_2 and D_2) is shown for the first time. These effects have a promising potential in controlling reaction dynamics, and thus the outcome of a reaction. Up until now, all experiments was achieved by means of steering electronic motion in a dissociating molecule in order to manipulate the outcome of the reaction [7][8]. This was achieved by introducing an asymmetric laser field to probe a symmetric molecule and, as a result, electron localization could be manipulated in the laboratory frame of reference in an attempt to reach the quantum control of the chemical reactions [35][36][16]. This work shows how the localization of the electron in H_2 and D_2 can be controlled by means of the number of absorbed photons and the delay between the pump and the probe pulses. The demonstrated experimental results are supported by a semi-classical simulation (carried out by Patrick Froß).

This thesis is structured as follows: in chapter 2, the interaction of atoms with laser field is described. Firstly, the response of atoms in a strong laser field is treated as a basis for high harmonic generation (HHG). Then, a semi-classical model explains HHG on a microscopic scale followed by its macroscopic properties. Moreover, RABBIT technique is introduced. In chapter 3, molecular hydrogen (H_2) is introduced with a short introduction to molecular symmetries and selection rules. Subsequently, the WKB approximation is presented, as well as the Floquet picture. finally, the electron localization is discussed. Chapter 4 gives an introduction into the experimental setup: the high-repetition-rate laser system. The interferometer and HHG setup. Eventually, the ReMi is introduced. Chapter 5

presents the experimental results of the interaction between the XUV-pump and IR-probe measurements. Firstly, dissociation of H_2 and D_2 with an APT is presented. Then, the vibrationally-resolved dissociation in the presence of an IR-probe pulse is examined. Finally, the application of RABBIT in the photodissociation of H_2 and D_2 is discussed. In chapter 6, the electron localization in the dissociation of H_2 and D_2 is introduced. Moreover, the results of a semi-classical simulation are compared with the observed experimental effects which show a very good agreement. This chapter concludes by presenting the electron localization as a function of the time delay between the XUV-pump and IR-probe pulses. Finally, chapter 7 summarizes the whole thesis and gives an outlook on future investigations.

Chapter 2

Interaction of Atoms with Light

As an atom or a molecule interacts with light, depending on the energy and the intensity of light, the bound electrons can be removed. This removal of electrons is called ionization. By studying this phenomena one can access the inner dynamics of the system in question. The experiments presented in this thesis are the result of a wide range of mechanisms leading to ionization. This chapter deals with the theoretical background in order to explain them. The first section covers the atomic response in a high-intensity light field. This is an important case in order to produce higher-energetic photons (up to 40 eV) using high harmonic generation (HHG) which is a highly non-linear interaction of an intense laser light with atoms allowing generation of coherent light in the extreme ultraviolet (XUV). Secondly, the interaction of these high energetic photons with atoms are explained. Finally, an interferometric method is presented which helps to investigate the response of the system on an attosecond time scale.

2.1 Atoms in Strong Light Fields and High Harmonic Generation

Nowadays, many table-top laser systems can produce pulses with intensity (10^{14} – $10^{15} W/cm^2$) of the order of the Coulomb potential of atoms ¹. These intensities can not be regarded as a perturbation anymore. As atoms are placed in such strong laser fields, numerous non-linear processes can lead to photoionization, as illustrated in Fig. 2.1, such as, above-Threshold Ionization (ATI), multiple ionization, over the barrier ionization, and tunnel ionization. In the following section, tunneling ionization is discussed because of its importance in high harmonic generation.

¹The magnitude of the Coulomb field binding the 1s electron in hydrogen atom is $5.1 \times 10^9 V.m^{-1}$ [44]

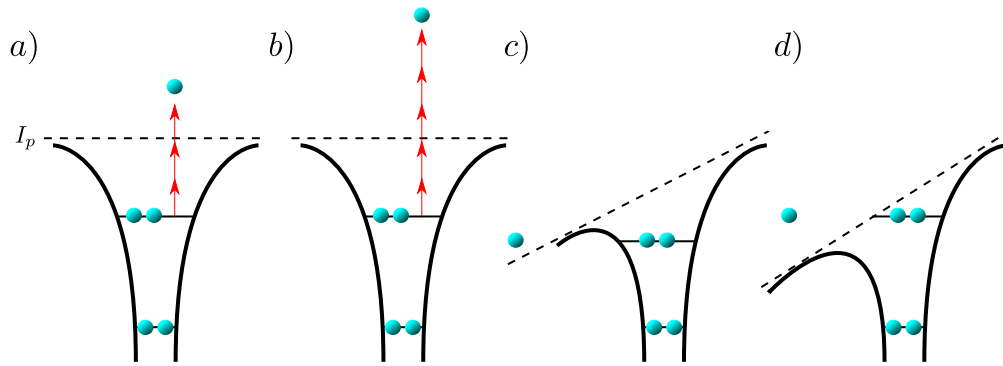


Figure 2.1: Atomic response in the presence of intense laser fields at the moment of ionization. The laser intensity increases from left to right. Multi-photon ionization happens when the electron absorbs multiple photons so as to reach enough energy to overcome the ionization potential (a). An electron can absorb more photons than required to escape the atom in a process known as over-threshold ionization (ATI) (b). The intense electric field of the laser disturbs the Coulombic potential of the atom so that an electron could tunnel out (c). As the laser intensity is further increased, a photo-electron can leave the atom without tunneling through the Coulomb potential (d). This process is known as over-the-barrier ionization.

2.1.1 High Harmonic Generation (HHG)

In 1987, it was observed for the first time, if a laser pulse with intensities in the order of $10^{14} \text{W}/\text{cm}^2$ is focused onto a gas target, a highly non-linear process can result in the production of the higher harmonics of the laser field [45] [46]. Although in order to completely describe this process a fully quantum mechanical approach is needed [47], a semi-classical treatment (the Three-Step Model [48] [49]) provides an intuitive explanation of HHG. This model can explain some characteristics of HHG, e.g., different trajectories for electrons, the cut-off energy, and the attochirp. In the following, the Three-Step model is discussed.

According to the three-step model, shown in Figure 2.2, in the first step, the Coulomb barrier of an atom placed in a strong laser field is distorted, and, as a result, an electron can tunnel through the barrier. After tunneling, in the second step, the electron is accelerated in the laser field. The kinetic energy gained by the electron depends on the release time according to Eq. 2.2. In the third step, as the laser field changes sign, the probability of the electron recombining with the parent ion increases. Upon recombination, the energy gained in the laser field by the electron is emitted in the form of a photon.

The electron trajectory $x(t)$, after the tunneling², in the laser field can be calculated

²The atomic potential is neglected after the ionization and the electron is assumed to have zero kinetic energy

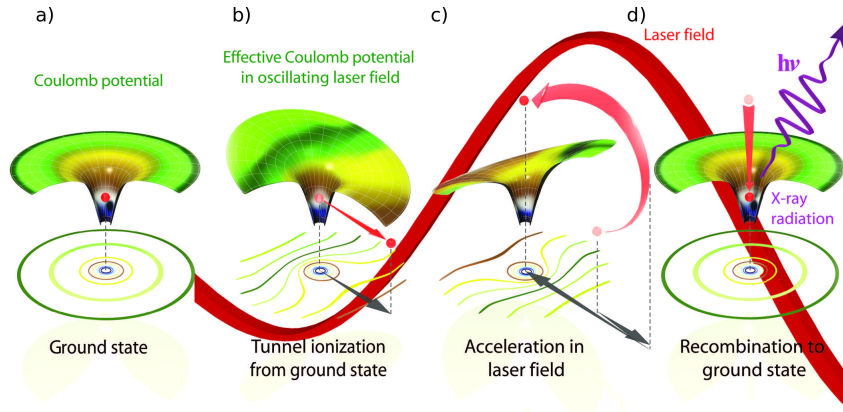


Figure 2.2: Simple-Man Model. a) The Coulomb potential of an atom in the ground state b) The Coulomb potential is bent in the presence of a strong laser field making it possible for the electron to tunnel through the Coulomb barrier. c) The electron is accelerating in the laser field, first, away from the parent ion, then as the electric field of the laser field changes sign, the electron gets accelerated in the opposite direction. d) An XUV photon is released upon recombination of the electron and the parent ion. Figure taken from [50].

using Newton's equation of motion. Assuming a linearly-polarized sinusoidal laser field in the x -direction: $\mathbf{E}(t) = \mathbf{E}_0 \cos(\omega t)$, with angular frequency ω and amplitude E_0 , the electron trajectory is then given by

$$x(t) = \frac{e\mathbf{E}_0}{m_e\omega^2} [\sin(\omega t) - \sin(\omega t_i) - \omega(t - t_i) \cos(\omega t_i)], \quad (2.1)$$

where t_i is the time of ionization, e and m_e are the electron charge and mass, respectively. Depending on the tunneling time, the recombination occurs at different instances, as illustrated in Fig.2.3. Electrons tunneling between 0 and $0.25 T$ (black trajectory), T being the laser period, do not recombine with the ion. Only those leaving between $0.25 T$ and $0.5 T$ could possibly recombine. The kinetic energy gained by the electron then becomes:

$$E_e = \frac{m_e |v(t)|^2}{2} = 2U_p [\cos(\omega t) - \cos(\omega t_i)]^2, \quad (2.2)$$

where U_p is the ponderomotive energy which is the kinetic energy gained by the electron owing to its oscillation in the laser field given by the expression

$$U_p = \frac{e^2 E_0^2}{4m_e\omega^2} = \frac{e^2 I}{2m\epsilon_0 c\omega^2} \propto I\lambda^2, \quad (2.3)$$

where e is the electron charge, m_e electron mass, ϵ_0 vacuum permittivity, c is the speed of light. The ponderomotive energy depends on the intensity I and wavelength λ of the laser field [51][52]. The energy of the emitted XUV photon is then given by

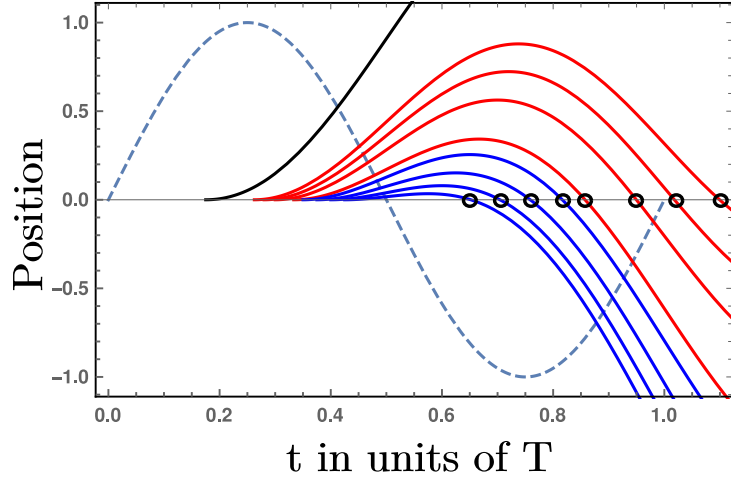


Figure 2.3: Solving Eq. 2.1 gives the electron trajectories for different tunneling times. The blue dashed line is the laser electric field. The red and blue curves are the long and short trajectories respectively. The black circles show the recombination position. The black curve is a trajectory with an emission time between 0 and $T/4$ which does not recombine with the parent ion.

$$E_{\gamma} = E_e + I_p, \quad (2.4)$$

where I_p is the ionization potential of the atom. The maximum XUV photon energy is $3.17U_p + I_p$ known as the cut-off energy.

2.1.2 Phase of HHG

As discussed above, each harmonic emerges from a different electron trajectory and a different return time. In other words, different energies in a HHG spectrum are the result of different recombination times, and therefore, different emission times. As a consequence, XUV radiation is chirped by its nature. This chirp is positive for short and negative for long trajectories. The chirp is approximately linear over a range of energies, as shown in Fig 2.8 [53].

2.1.3 Macroscopic Properties of High Harmonic Generation

To describe the HHG process in real-life one should consider an ensemble of atoms placed in the laser focus. To maximize the HHG yield, there should be a constructive interference in single-atom emissions (see figure 2.4). All the conditions contributing to this constructive adding of single emissions is called **phase matching**. By defining the mismatch vector

$\Delta K = qK_f - K_q$, where K_f is the fundamental laser field wavevector and K_q is the one for the q th harmonic, one can characterize the phase matching condition. The ideal phase matching happens when $\Delta K = 0$. There are four main contributions to the mismatch vector [54][55][56]:

- Gouy phase mismatch (Δk_g) caused by the spatial Gouy phase along the focus of a Gaussian beam ranging from $-\pi/2$ at $z = -\infty$ to $\pi/2$ at $z = \infty$. the Gouy phase mismatch is the cause of not reaching a perfect phase matching [57].
- Δk_n and Δk_p are the neutral and plasma dispersion respectively. Free electrons produced as a result of the ionization of the driving laser produce plasma with a refractive index n_q for q th harmonic

$$n_q = \sqrt{1 - \left(\frac{\omega_p}{q\omega}\right)^2}, \quad (2.5)$$

where $\omega_p = \sqrt{4\pi e^2 N_e / m_e}$ is the *plasma frequency*, q is the harmonic order, and ω is the fundamental frequency.

- Atomic dipole phase mismatch (Δk_d) is the accumulated phase during the movement of the electron in the laser field. Δk_d is generally negative for atoms located before the focus and positive for behind the focus.

The resulting vector mismatch is then given by

$$\Delta K = \Delta k_d + \Delta k_n + \Delta k_g + \Delta k_p \quad (2.6)$$

During an experiment three parameters can be adjusted: Laser intensity, gas pressure, and focus position. Intensity influences mainly, Δk_p , Δk_n , and Δk_d . As the intensity increases, more free electrons are produced which results in high plasma dispersion. On the other hand, higher intensities are needed to increase the cut-off energy. Gas density also has an effect on Δk_n and Δk_p .

2.1.4 Attosecond pulse trains (APT)

The three-step model happens every half cycle of the driving laser field. During each half-cycle a burst of attosecond pulses is emitted. For long pulses with many cycles, this leads to production of attosecond pulse trains with $T/2$ spacing between spikes, where T is the period of the driving laser field. This process manifests itself, in the frequency domain, as a frequency comb with a spacing of 2ω . Different photon energies are produced within one half cycle of the driving laser field, as illustrated in Fig. 2.5

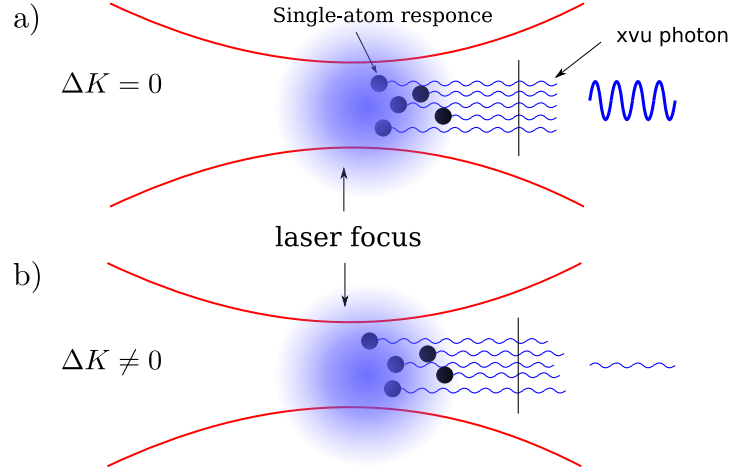


Figure 2.4: Illustration of the phase matching of one harmonic (one wavelength). Each atom emits an XUV-photon. a) In a perfect phase-matching condition ($\Delta K = 0$), single-atom responses are in phase resulting in a constructive interference. b) Destructive interference if the phases of different emissions do not match ($\Delta K \neq 0$).

2.2 Single-Photon ionization using XUV light

Ionization is a tool to study dynamics of atoms and molecules. It is most favorable to ionize while the system under study is least disturbed. XUV light is a powerful tool because the photon energy can ionize most atoms and molecules with only one photon absorption. If an atom absorbs a photon with an energy larger than the ionization potential (I_p) of the atom. One or many electrons can be ionized. Single-photon single-ionization is given by the equation



The surplus energy ($\epsilon = E_\gamma - I_p$) will be carried by the ejected electron. The probability amplitude α_ϵ of this transition once the interaction is over, according to the first-order perturbation theory, is given by

$$\alpha_{\epsilon,l} = \frac{e}{i\hbar} \langle f_l | \hat{r} | g \rangle \cdot E_{XUV}(\Omega), \quad (2.8)$$

where e is the electron charge, $\langle f_l |$ is the final unbound state with angular momentum l , \hat{r} is the electric dipole operator, and $|g\rangle$ is the ground state. The electric dipole operator expresses the interaction between dipole (charge separation) of the atom and the electric field component of the light field. Since a photon carries one unit of angular momentum, only transitions changing the angular momentum by ± 1 are allowed owing to the conservation of angular momentum.

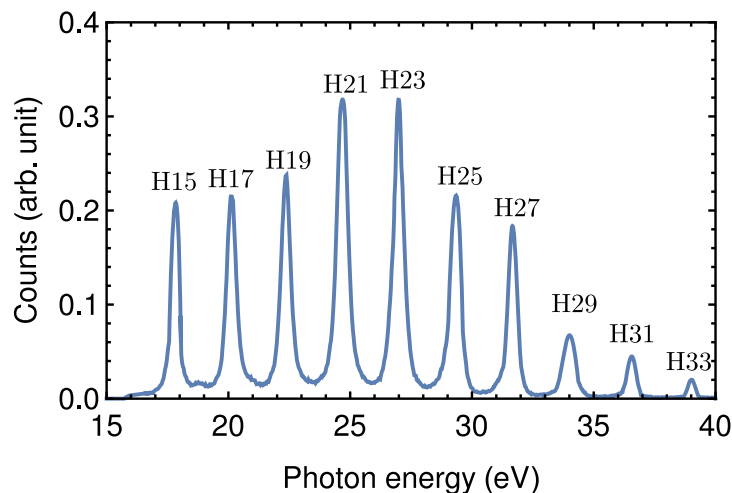


Figure 2.5: The XUV spectrum reconstructed from photoelectrons as a consequence of ionization of argon with an APT in the Reaction Microscope. The photoionization cross section of argon and the aluminum transmission for XUV light were used to retrieve the photon spectrum.

Laser-assisted Photoionization

The interaction of an atom with an XUV photon and an IR photon could lead to the absorption of an XUV photon and an IR photon exchange according to

$$A + \Omega_{XUV} \pm \omega_{IR} \rightarrow A^+ + e^-. \quad (2.9)$$

At IR intensities in the order of 10^{11} W/cm^2 , only one IR photon can be absorb or emit-

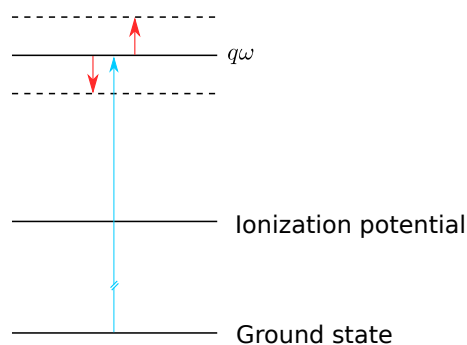


Figure 2.6: An atom is ionized with an XUV photon in the presence of an IR field resulting in appearance of sideband (dashed lines) by absorbing or emitting an IR photon (red arrows).

ted resulting in three peaks in photoelectron spectrum. The central one is the direct result of the XUV ionization while the two neighboring peaks correspond to the emission and absorption of an IR photon. In order to formulate this process, one can imagine a transition triggered by an XUV photon from ground state $|g\rangle$ to an intermediate continuum state $|\alpha\rangle$ which can further absorb or emit an IR photon resulting in a final state $|f\rangle$. On the assumption that, there is only one accessible state in the continuum, the two-photon transition matrix (using second-order perturbation theory), in the case of a linearly polarized light in \hat{z} direction, is given by

$$M_{fg}^{\pm} = \lim_{\epsilon \rightarrow 0} \sum_{\alpha} \frac{\langle f | \hat{z} | \alpha \rangle \langle \alpha | \hat{z} | g \rangle}{\hbar\Omega - E_{\alpha} + E_g + i\epsilon}, \quad (2.10)$$

where energies of the ground and intermediate states are denoted as E_{α} E_g , respectively. The Ω is the XUV angular frequency, and ϵ is the infinitesimal quantity ensuring correct boundary conditions during ionization process. The sum is performed over all continuum and bound intermediate states α . A two-photon transition can be thought of as a sum of two steps, namely, the transition from ground to intermediate state, and a continuum-continuum (CC) transition from the intermediate to final state [61] [27] [62].

2.2.1 Attosecond photoelectron interferometry

RABBIT (Reconstruction of Attosecond Beating By Interference of Two-photon transitions) is a widely used technique for phase characterization of high harmonic generation [58] [59] was first used to measure the duration of an XUV pulse [6]. More recently it has been also used to acquire information on ionization time delays by measuring the relative phases of emitted photo-electrons [27][26][60].

According to this cross-correlation technique, XUV pulses are probed with a small portion of the driving laser field where two fields are locked in phase. As shown in Fig. 2.6, an atom is ionized with an APT which results in the emergence of photon-electrons with energy spacing of $\hbar\omega_q - I_p$ where q is the harmonic order and I_p is the ionization potential of the atom. The presence of the driving laser field with a photon energy of $\hbar\omega$ results in absorption or emission of an extra photon by the photo-electrons. As a result, additional peaks called side-bands appear in the photo-electron spectrum. The intensity of the probe field is kept low so as to avoid multiphoton processes. Since two quantum paths lead to the same final energy, the side-bands oscillate as a result of an interference explained in more detail in the following section.

The total transition probability from ground to final state is given by

$$\mathcal{A}_{fg}^{\pm}(\tau) = -\frac{ie^2}{\hbar} E_{XUV}(\Omega) E_{IR}(\omega) e^{\pm i\omega\tau} M_{fg}^{\pm}, \quad (2.11)$$

where τ is the delay between XUV and IR pulse.

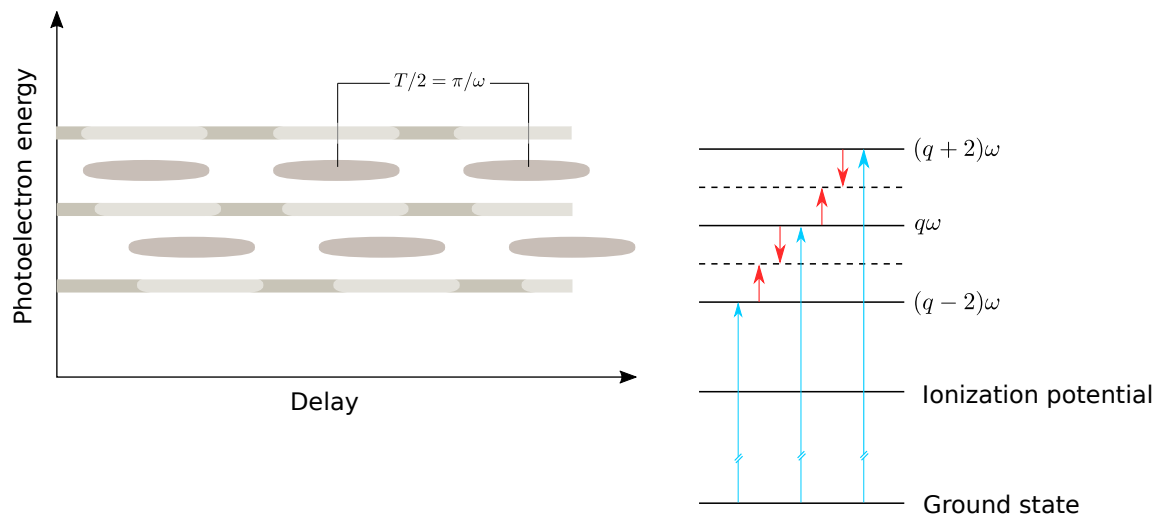


Figure 2.7: Schematic illustration of a RABBIT measurement. Right panel illustrates the emergence of sidebands in the presence of the IR field where photoelectrons absorb or emit and IR resulting in a peak in between. Each sideband can be reached from two neighboring harmonics. Left panel illustrates the oscillation of side-bands with the delay between two fields with a frequency of 2ω where ω is the driving laser frequency. The oscillations are the consequence of interferences between the amplitudes corresponding to the different quantum paths giving rise to a sideband. The intensity of harmonic lines oscillates as well due to the conservation of electron numbers. Adapted and modified from [63].

As for the frequency comb of XUV, the sidebands are accessible from both neighboring XUV peaks as shown in Fig. 2.7 The intensity of q^{th} sideband is given by

$$\begin{aligned} S_q &= |\mathcal{A}_{q-1}^- + \mathcal{A}_{q+1}^-|^2 \\ &= |\mathcal{A}_{q-1}^-|^2 + |\mathcal{A}_{q+1}^+|^2 + 2|\mathcal{A}_{q-1}^-||\mathcal{A}_{q+1}^+|^2 \cos(2\omega\tau - \Delta\phi), \end{aligned} \quad (2.12)$$

where $\mathcal{A}_{q\pm 1}^\pm$ is the amplitude of the two-photon transition including and XUV photon q and absorption (+) and emission (-) of an IR photon. The delay-dependent intensity of the sidebands oscillates at the frequency 2ω as a consequence of the interference of two quantum paths. Referring to Eq. 2.11, The phase of the oscillation $\Delta\phi$ consists of different terms

$$\Delta\phi = \Delta\phi_{XUV} + \Delta\phi_{aux}, \quad (2.13)$$

where $\Delta\phi_{XUV} = \phi_{q+1} - \phi_{q-1}$ is the group delay of the attosecond pulse owing to the difference in the emission times of consecutive harmonics. $\Delta\phi_{aux}$ is the phase of the two-photon dipole transition matrix element originating from each pathway. This phase term is the result of the interaction of the electron wavepacket with the ionic core and the probe field [61].

By fitting a function of the form $A \cos(\omega\tau - \Delta\phi) + B$, one can extract the phase of each sideband, as shown in Fig. 2.8. Regarding a transition to a flat continuum without any resonant states, the phase variations of the sideband is mostly dominated by the XUV group delay also known as attochirp.

Phase term ϕ_{aux}

ϕ_{aux} phase factor³ is composed of two terms: ϕ_w and ϕ_{cc} . The former one is the result of the phase of the EWP after the photo-ionization influenced by the atomic or molecular potential. The ϕ_{cc} contribution can be assigned to transition driven by the laser field connecting two continuum states in the presence of the long range Coulomb potential [26]. A detailed derivation regarding ϕ_{cc} can be found in [61]. In the presence of a resonance state one path could reach the final state while the other one has a smooth transition to the final continuum state. In such cases the measured phase could be associated to the dwell time in the resonant states of atoms [65] [66][67] or molecules molecules [68] [69]. In section 5.4.2 the behavior of ϕ_{aux} is studied experimentally in the presence of autoionization states in H₂ and D₂.

³Values for ϕ_{aux} are calculated by Mauritsson *et al.* [64] for helium, neon, and argon by solving numerically the TDSE.

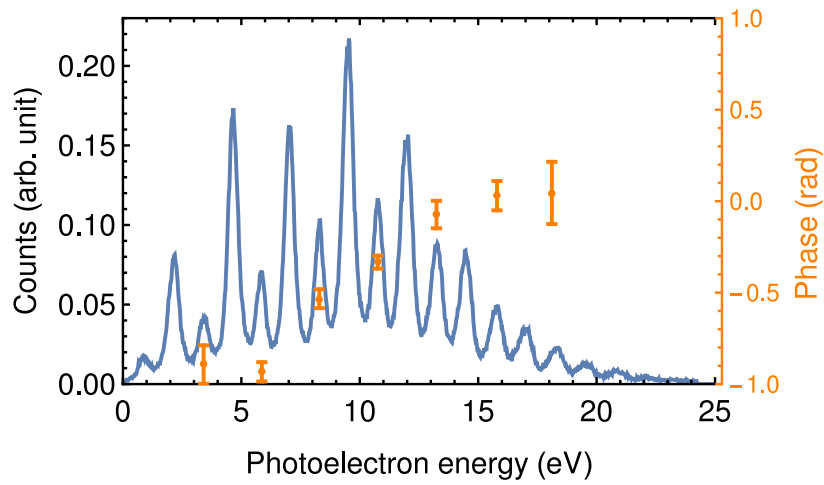


Figure 2.8: Photo-electron spectrum as a result of the interaction of XUV+IR with argon. Relative phases of each harmonic is shown with orange dots showing almost a linear trend dominated mostly by the attochirp of XUV pulse because in argon ϕ_{aux} is small, and thus negligible compared to the attochirp [6].

Chapter 3

Hydrogen Molecule

This chapter is dedicated to the simplest electrically neutral molecule. H_2 which consists of two electrons and two hydrogen atoms. The simplest existing molecule is hydrogen ion (H_2^+). It consists of an electron and two nuclei. Despite the simplicity of these systems, an analytical solution to the Schrodinger equation for H_2^+ only exists with utilising some approximations.

3.1 The Born-Oppenheimer Approximation

This approximation, which was suggested by Max Born and Robert Oppenheimer [73], is based on the fact that the nuclei are much heavier than electrons, and as a result, the motion of the electrons in a molecular system can be described independently of the dynamics of the nuclei. In other words, electrons can adjust their positions instantaneously to new configurations of the nuclei [74] [75]. The potential curves are then calculated from the total energy of the system by fixing the internuclear distance. The stationary Schrodinger equation for a molecule is given by

$$\hat{H}\psi(\mathbf{r}_i, \mathbf{R}_k) = E\psi(\mathbf{r}_i, \mathbf{R}_k), \quad (3.1)$$

where \mathbf{r}_i and \mathbf{R}_k are the electron and nuclear coordinates, respectively. The hamiltornian is expressed by

$$\hat{H}(\mathbf{r}, \mathbf{R}) = \hat{T}_n(\mathbf{R}) + \hat{T}_e(\mathbf{r}) + V_n(\mathbf{R}) + V_e(\mathbf{r}) + V_{ne}(\mathbf{r}, \mathbf{R}), \quad (3.2)$$

where the first two terms are the kinetic energy of nuclei and electrons, respectively. The next two terms are the repulsive potential energy of the nuclei and electrons, and the last term is the attraction between the nuclei and electrons.

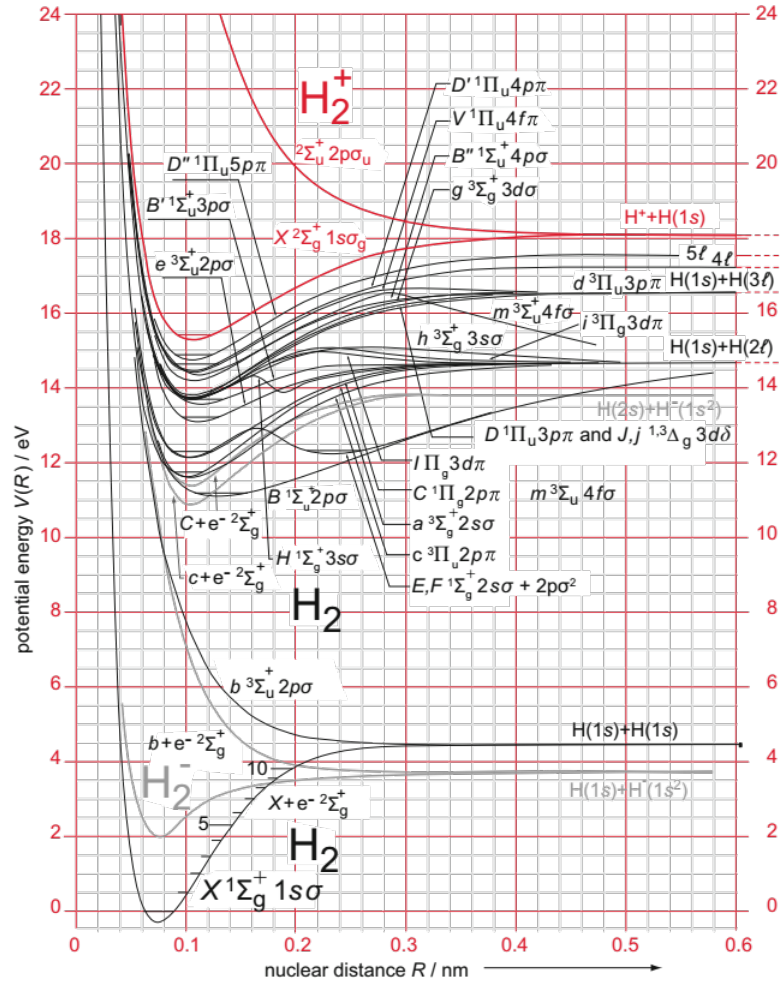


Figure 3.1: Potential energy curves for H_2 molecule. Figure taken from [76].

Using the Born-Oppenheimer approximation, one can separate the molecular, $\chi(\mathbf{R}_k)$, and electronic wave function, $\Phi(\mathbf{r}_i, \mathbf{R}_k)$:

$$\psi(\mathbf{r}_i, \mathbf{R}_k) = \chi(\mathbf{R}_k) \cdot \Phi(\mathbf{r}_i, \mathbf{R}_k), \quad (3.3)$$

for the electronic wave function, the molecule is regarded as a rigid rotor, at a fixed nuclear position \mathbf{R}_k , with electron coordinates \mathbf{r}_i . The coupling between electron and nuclei dynamics is neglected in the above equation. The total energy E is the sum of the kinetic energy of the nuclei ($E_{vib} + E_{rot}$) and $E_n^{el}(R)$ in the n th electronic state according to the potential curves 3.1. However, in the last chapter it is shown, based on experimental data, that the electronic dynamics can be strongly modified by the nuclei movement.

3.2 Molecular Time Scale

There are different types of motions on different time scales in molecules. The energy spacing between the ground and final level determines the timescale of the system dynamics 3.1. Electronic transitions are in visible to ultra-violet range, vibrational ones are in mid-infrared, and rotational ones in microwave range as summarised in table 3.1.

Table 3.1: Timescale of molecular transition.

Transition	Period	Energy difference
Rotational	0.1 – 10 <i>ps</i>	$10^{-4} - 10^{-2} eV$
Vibrational	10 – 100 <i>fs</i>	$3 \cdot 10^{-2} - 3 \cdot 10^{-1} eV$
Electronic	0.1 – 1 <i>fs</i>	$> 0.6 eV$

3.3 Molecular Orbital and Electronic States Nomenclature

Unlike atomic electrons which move in a spherically symmetric potential, in case of linear molecules cylindrical coordinate should be adapted. The angular momentum operator \mathbf{L} and the Hamiltonian do not commute any more, and the orbital angular momentum is no longer a good quantum number. However, The projection of \mathbf{L} , onto the molecular axis is a conserved quantity ($[\hat{H}, \hat{L}_z] = 0$). As a consequence, eigenvalues of \hat{L}_z are $\lambda\hbar$ where $\lambda = m_l$ similar to atoms. λ is used to identify molecular orbitals (MOs) for diatomic molecules, the same as l for atoms. Lower-case Greek letters are used to label MOs. e.g. σ_g^+ , σ_u , π_g , π_u , ... for homo-nuclear, as shown in

Angular Momentum	0	1	2	...
λ	σ	π	δ	

Similarly, to characterize the total molecular state containing several electrons capital Greek letters are used according to

Angular Momentum	0	1	2	3	...
Λ	Σ	Π	Δ	Φ	

Inversion at the center of the mass is another symmetry operator concerning homo-nuclear molecules ($r \rightarrow -r$). This is known as the parity of the molecular state having odd (ungerade) or even (gerade) parity. Even parity corresponds to $\Phi_g(r) = \Phi_g(-r)$ whereas odd parity corresponds to $\Phi_u(r) = -\Phi_u(-r)$. The total spin of a molecule is the sum of the

individual electron spins

$$\hat{S} = \sum_i \hat{S}_i \quad (3.4)$$

where $|\hat{S}| = \sqrt{S(S+1)}$. The overall electron states have a multiplicity of $2S+1$.

Molecular states are denoted (equivalent to *term symbol* in case of atoms)

$${}^{2S+1}\Lambda_{g/u}^{+/-} \quad (3.5)$$

where $+/-$ represents the reflection symmetry with respect to the plain containing the nuclear axis.

Additionally, capital letters are served to identify the state (ground, first, second excited state, ...)(X, A, B, C, \dots), and Q_n for doubly-excited states. For instance, in the case of H_2 , the ground state is $X^1\Sigma_g^+$. As for H_2^+ the lowest two states are $X^2\Sigma_g^+$, and $A^2\Sigma_u^+$ respectively [77] [78] [79] [80] [81].

3.4 Symmetry, Group Theory, and Selection Rules

By definition, a transformation leaving an object indistinguishable from its original configuration is called a symmetry operation. For each symmetry operation there is a corresponding symmetry element. These are point, line, and plane. A symmetry operation is done with respect to a symmetry element, for instance, a rotation around an axis, reflection relative to a plane and inversion with respect to a point. Objects, molecules for example, that contain the same set of symmetry elements can be classified in a group. regarding molecules, this classification is very important because it enables one to draw general conclusions regarding molecules properties in a particular class, e.g., if a molecule has a dipole moment, what are the selection rules for electronic rovibronic transitions, and degeneracy of molecular state. A point group is defined as a group of symmetry elements with respect to which symmetry operations leave at least a common point unchanged. These symmetry operations are identity (E), n-fold proper rotation C_n by an angle of $2\pi/n$, reflection through the plane σ , inversion i , and n-fold improper rotation S_n . The symmetry properties of a particular point group are given in character tables. For example H_2 and D_2 (homonuclear diatomic molecules) belong to $D_{\infty h}$ point group with the corresponding character table given in table 3.2.

Table 3.2: Character Table for $D_{\infty h}$, point group. The fully symmetric irreducible representation is shown in red.

$D_{\infty h}$	E	$2C_{\infty}^{\phi}$	$\infty\sigma_v$	i	$2S_{\infty}^{\phi}$	$\infty C_2 \dots$		
Σ_g^+	1	1	1	1	1	1	R_z	$\alpha_{x^2+y^2}, \alpha_{z^2}$
Σ_g^-	1	1	-1	1	1	-1		
Π_g	2	$2 \cos \phi$	0	2	$-2 \cos \phi$	0		
Δ_g	2	$2 \cos 2\phi$	0	2	$2 \cos 2\phi$	0	T_z	$\alpha_{x^2-y^2}, \alpha_{xy}$
\vdots	\vdots	\vdots	\vdots	\vdots	\vdots	\vdots		
Σ_u^+	1	1	1	-1	-1	-1		
Σ_u^-	1	1	-1	-1	-1	1		
Π_u	2	$2 \cos \phi$	0	-2	$2 \cos \phi$	0	$T_{x,y}$	
Δ_u	2	$2 \cos 2\phi$	0	-2	$-2 \cos 2\phi$	0		

There are many important aspects to a character table which are out of the scope of this work. The relevant feature in this work, however, is the derivation of selection rules. Table 3.4, Eq. 3.6 and Eq. 3.7 show general rules for the product of two irreducible representations.

$$g \otimes g = g, \quad u \otimes u = g, \quad g \otimes u = u, \quad (3.6)$$

$$+ \otimes + = +, \quad - \otimes - = +, \quad + \otimes - = -, \quad (3.7)$$

Table 3.3: Direct product table of the point group $D_{\infty h}$.

$D_{\infty h}$	Σ^+	Σ^-	Π	Δ	Φ	Γ	...
Σ^+	Σ^+	Σ^-	Π	Δ	Φ	Γ	
Σ^-		Σ^+	Π	Δ	Φ	Γ	
Π			$\Sigma^+ + \Sigma^- + \Delta$	$\Pi + \Phi$	$\Delta + \Gamma$	$\Phi + H$	
Δ				$\Sigma^+ + \Sigma^- + \Gamma$	$\Pi + H$	$\Delta + I$	
Φ					$\Sigma^+ + \Sigma^- + I$	$\Pi + \Theta$	
Γ						$\Sigma^+ + \Sigma^- + K$	
\vdots							

Selection Rules

The electric and magnetic components of the light can interact with the molecular system¹. The electric component of the radiation interacts with the electric dipole moment (or weakly with the quadrupole moment) of the molecule. Possibility of these transitions via these interaction are determined by *Selection rules*. Although selection rules are described completely with quantum numbers in atoms, in diatomic molecules, quantum numbers are insufficient and the symmetry of the electronic wave function has to be taken into

¹The electric interactions are 10^5 times stronger than the magnetic ones

account². E.g., in the case of homonuclear diatomic molecules such as H₂, electronic transitions between states which are both symmetric or antisymmetric are not allowed. [82] [83].

For each electronic state in a molecule there are corresponding vibrational and rotational levels of modifications. Usually these modifications happen simultaneously during an electronic transition, and as a result complicated spectra are produced. For simplicity (please refer to 3.2) one can leave out rotational transitions in the molecular wave function, and by applying the Born-Oppenheimer approximation, the molecular wave function can be written

$$\psi = \psi_e \psi_v \quad (3.8)$$

where ψ_e is the electronic wave function (containing the spin wave function), and ψ_v the vibrational (nuclear) wave function. An electronic transition can be described by transition between the initial state ψ_i and the final state ψ_f via a dipole transition with the transition moment integral

$$M = \int \psi_f^* \mathbf{D} \psi_i d\tau \quad (3.9)$$

where \mathbf{D} is the dipole moment operator containing a nuclear (\mathbf{D}_n) and electronic part (\mathbf{D}_e). Using 3.8

$$\begin{aligned} M &= \int \psi_e^* \psi_v^* (\mathbf{D}_n + \mathbf{D}_e) \psi_e \psi_v d\tau \\ &= \int \psi_e^* \psi_v^* \mathbf{D}_n \psi_e \psi_v d\tau + \int \psi_e^* \psi_v^* \mathbf{D}_e \psi_e \psi_v d\tau \\ &= \underbrace{\int \psi_e^* \psi_e d\tau_e}_{=0} \int \psi_v^* \mathbf{D}_n \psi_v d\tau_n + \underbrace{\int \psi_v^* \psi_v d\tau_n}_{\text{Franck-Condon integral}} \int \psi_e^* \mathbf{D}_e \psi_e d\tau_e \end{aligned} \quad (3.10)$$

the first integral in the last line is zero because of orthogonality of electronic wave functions, and the labeled Franck-Condon factor integral belongs to two electronic states with different potential functions, and thus is not necessarily zero. By introducing the spin of the electron in equ. 3.8 the above equation can be rewritten as

$$M = \underbrace{\int \psi_v^* \psi_v d\tau_n}_{\text{Franck-Condon factor}} \underbrace{\int \psi_e^* \mathbf{D}_e \psi_e d\tau_e}_{\substack{\text{orbital} \\ \text{selection} \\ \text{rules}}} \underbrace{\int \psi_e^* \psi_e d\tau_e}_{\substack{\text{spin} \\ \text{selection} \\ \text{rules}}} \quad (3.11)$$

²One can in general express selection rules in atoms also with symmetry description but this is more complex than the quantum number treatment.

in which the transition is not allowed if any of the integrals is zero. From the above equation, the spin selection rules referring to the transitions between two states of equal multiplicities due to the orthogonality of spin wave functions can be derived

$$\Delta S = 0. \quad (3.12)$$

To define orbital selection rules (an electronic transition), one can use the symmetry properties introduced earlier.

Orbital Selection Rules

A transition is only allowed if its total symmetry includes the fully symmetric irreducible representation of the point group. In other words

$$\Gamma_i \otimes \Gamma_{T(x,y,z)} \otimes \Gamma_f \supset \Gamma_{Sym} \quad (3.13)$$

where Γ_i and Γ_f are the irreducible representation of the initial and final states, respectively, and $\Gamma_{T(x,y,z)}$ is that of the dipole operator. The character table for homo-nuclear diatomic molecules is shown in 3.2 with Σ_g^+ being the full symmetry irreducible representation.

In order to see if a dipole transition from the ground state of H_2 molecule (Σ_g^+) to the lowest doubly-excited state ($Q_1\Sigma_u^+$) is possible, using Eq. 3.13

$$\Sigma_g^+ \otimes \Gamma_{T(x,y,z)} \otimes Q_1\Sigma_u^+ \supset \Sigma_g^+ \quad (3.14)$$

one has to only determine the remaining term $\Gamma_{T(x,y,z)}$. It turns out that the $\Gamma_{T(x,y,z)}$ has an irreducible representation of Σ_u^+ , which corresponds (according to the character table 3.2) to the dipole operator linear in z direction. Generally, the selection rules are given for parallel transitions by

$$\Delta\Lambda = 0 \quad (3.15)$$

$$u \leftrightarrow g \quad (3.16)$$

and for perpendicular ones by

$$\Delta\Lambda = \pm 1 \quad (3.17)$$

$$u \leftrightarrow g \quad (3.18)$$

A summary is given in table 3.4.

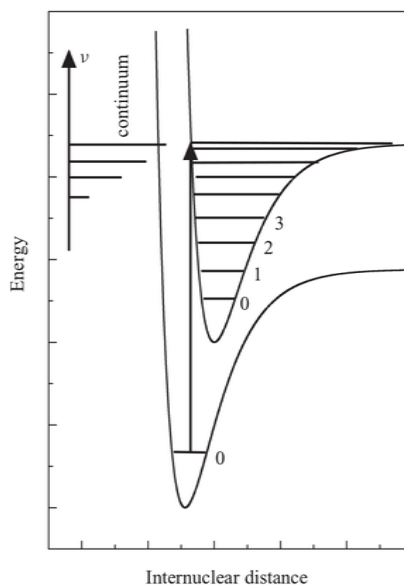


Figure 3.2: Franck-Condon Principle. Those transitions, during which the nuclei coordinates change the least, are the most favoured ones. In the upper left, a spectrum of the resulted transitions is shown. Figure taken from [84].

Table 3.4: Dipole transitions in homonuclear diatomic molecules. \parallel and \perp show allowed parallel and perpendicular transitions, respectively. \times indicates forbidden transitions.

	Σ_g^+	Σ_g^-	Σ_u^+	Σ_u^-	Π_g	Π_u	Δ_g	Δ_u
Σ_g^+	\times	\times	\parallel	\times	\times	\perp	\times	\times
Σ_g^-		\times	\times	\parallel	\times	\perp	\times	\times
Σ_u^+			\times	\times	\perp	\times	\times	\times
Σ_u^-				\times	\perp	\times	\times	\times
Π_g					\times	\parallel	\times	\perp
Π_u						\times	\perp	\times
Δ_g							\times	\parallel
Δ_u								\times

3.5 The Franck-Condon principle

According to Franck-Condon Principle, since the vibrational transition are much slower than the electronic ones, the nuclei are stationary during an electronic transition. In other words, a transition can be shown by a vertical arrow at one fixed nuclear distance in the

potential curves, as illustrated in Fig. 3.2. For instance, in the case of the single ionization of H_2 , a vertical transition happens between the ground state of H_2 to that of H_2^+ i.e. the projection of the wave function of H_2 onto the wave function of H_2^+ using the dipole matrix elements (the first term in Eq. 3.11). The probability of this transition is not dependent on the nuclei distance. These probabilities of occupation for different vibrational levels of the ground state of the molecular hydrogen ion and deuterium ion are given in appendix B.

3.6 WKB Approximation

Unlike assuming simple potentials with small variation as in the case of the perturbation theory, WKB uses a slow varying potential.

Starting with the Schrödinger equation in one dimension with an arbitrary potential $V(x)$

$$-\frac{\hbar^2}{2m} \frac{d^2}{dx^2} \psi(x) + V(x)\psi(x) = E\psi(x), \quad (3.19)$$

where E is an energy eigenvalue. In case of a constant potential, solutions in the form of plane wave exists

$$\psi = A \exp\left(\pm \frac{i}{\hbar} p_0 x\right) \quad (3.20)$$

with

$$p_0 = \sqrt{2m(E - V_0)} \quad (3.21)$$

being constant. On the other hand, if the potential is not constant ($V(x)$ hence $p(x) = \sqrt{2m(E - V(x))}$) one can look for solutions in the form of

$$\psi = A \exp\left(\pm \frac{i}{\hbar} S_0(x)\right). \quad (3.22)$$

Putting the above equation into Eq. 3.6 results in

$$-\frac{i\hbar}{2m} \frac{d^2 S(x)}{dx^2} + \frac{1}{2m} \left[\frac{dS(x)}{dx} \right]^2 + V(x) - E = 0 \quad (3.23)$$

According to WKB approximation $S(x)$ is expanded in power series of \hbar

$$S(x) = S_0(x) + \hbar S_1(x) + \frac{\hbar^2}{2} S_2(x) + \dots \quad (3.24)$$

By inserting the above equation into Eq. 3.23 one obtains

$$-\frac{i\hbar}{2m} \frac{d^2}{dx^2} (S_0(x) + \hbar S_1(x) + \dots) + \frac{1}{2m} \left[\frac{d}{dx} (S_0(x) + \hbar S_1(x) + \dots) \right]^2 + V(x) - E = 0 \quad (3.25)$$

Taking the classical limit ($\hbar \rightarrow 0$) results in

$$\frac{1}{2m} \left[\frac{dS_0(x)}{dx} \right]^2 + V(x) - E = 0, \quad (3.26)$$

and therefore the solution is given by

$$S_0(x) = \pm \int_{x_0}^x \sqrt{2m(E - V(x'))} dx'. \quad (3.27)$$

Putting the above equation into 3.22 yields

$$\psi = B \exp\left(\pm \frac{i}{\hbar} \int \sqrt{2m(E - V(x'))} dx' - iEt/\hbar\right), \quad (3.28)$$

where B is a normalization factor. According to the above equation, the phase of the wave-packet which is propagating along the potential $V(x)$ can be approximately given by the exponential term.

3.7 The Floquet Picture (Laser-Dressed Molecular Potentials)

In order to acquire an understanding of photo-induced processes in molecules, such as photo-dissociation, the Floquet picture (FP), thoroughly described in [85, 86], is a powerful tool. This picture is most suited for intensities below 10^{13}W/cm^2 , and wavelengths in visible to UV regions. Under these conditions, few-photo resonances are dominant processes. In the presence of the laser field new light-induced potential curves³ (LIPs) are formed, as illustrated in Fig. 3.3. These are parallel potential energy curves which are separated by $n\hbar\omega$, where $n = 1, 2, 3, \dots$, resulting in light-induced conical intersections or avoided crossings [87][88]. LIPs are obtained by diagonalizing the diabatic potential matrix

$$V(R) = \begin{bmatrix} V_g(R) + \hbar\omega & V_{gu}(R) \\ V_{gu}(R) & V_u(R) \end{bmatrix}, \quad (3.29)$$

giving rise to light induced potentials (LIPs)

³they are the consequence of applying Born-Oppenheimer approximation to the dressed molecular Hamiltonian.

$$V_{\pm}^{adiabatic} = \frac{V_g(R) + \hbar\omega + V_u(R)}{2} \pm \sqrt{(V_g(R) + \hbar\omega - V_u(R))^2 + 4V_{gu}(R)^2}. \quad (3.30)$$

where V_g and V_u are field free $1s\sigma_g$ and $2p\sigma_u$, respectively. The term $V_{gu}(R) = -\frac{1}{2}\epsilon(t)D(R)\cos\theta(t)$ where $D(t)$ is the transition dipole between two curves and $\theta(t)$ is the angle of laser polarization with respect to the molecular axis, and $\epsilon(t) = A(t)\cos(\omega(t)t)$, where $A(t)$ is the temporal field envelope, and $\omega(t)$ is the instantaneous frequency. The characteristics of avoided crossings are then controlled by the intensity and frequency of the field, as well as, alignment of the molecule. If R_c is the position of the avoided crossing, the transition between these LIPs at R_c can be calculated using *Landau-Zener* equation [89][90]. The presence of LIPs results in a new series of different phenomena, such as bond softening, bond hardening and above-threshold dissociation.

3.7.1 Bond Softening, Hardening and above-threshold dissociation

The opening of the crossing increases with the intensity. The vibrational levels above the opening level, which were once bound in the field-free diabatic potential curves, are no longer bound and dissociate. Levels lying below the crossing have a chance to tunnel out through the potential barrier. This process is known as **bond softening** [94][95].

If the laser intensity is further increased ($\approx 10^{14}W/cm^2$), vibrational levels at around the three-level crossing can lead to dissociate. A molecule can then follow the adiabatic potential $|u, u-3\rangle$ until it reaches X_3 avoided crossing where one photon is emitted and the molecule ends up in $|g, n-2\rangle$ resulting in a net two-photon transition. In analogy to atoms where they can absorb more photons necessary needed to be ionized, this process is called in molecules **above-threshold dissociation** [96][94][95][97].

Vibrational levels above the one-photon crossing can be trapped in the adiabatic potential well in a process known as bond hardening or vibrational trapping predicted first theoretically [98][99] and proven subsequently experimentally in H_2 [100] and D_2 [101]. If the laser field intensity is decreased at this point, these trapped states can either go back to the bound state of the molecular ion $1s\sigma_g$ in a process known as molecular stabilization in strong laser field [102] or stay on the repulsive $2p\sigma_u - \omega$ dissociating at the one-photon limit.

If the field intensity is further increased during trapping, the lower point of the adiabatic potential well the trapped vibrational levels is lifted, and as a result, the molecule dissociates to the field-free dissociation limit with almost zero kinetic energy [103].

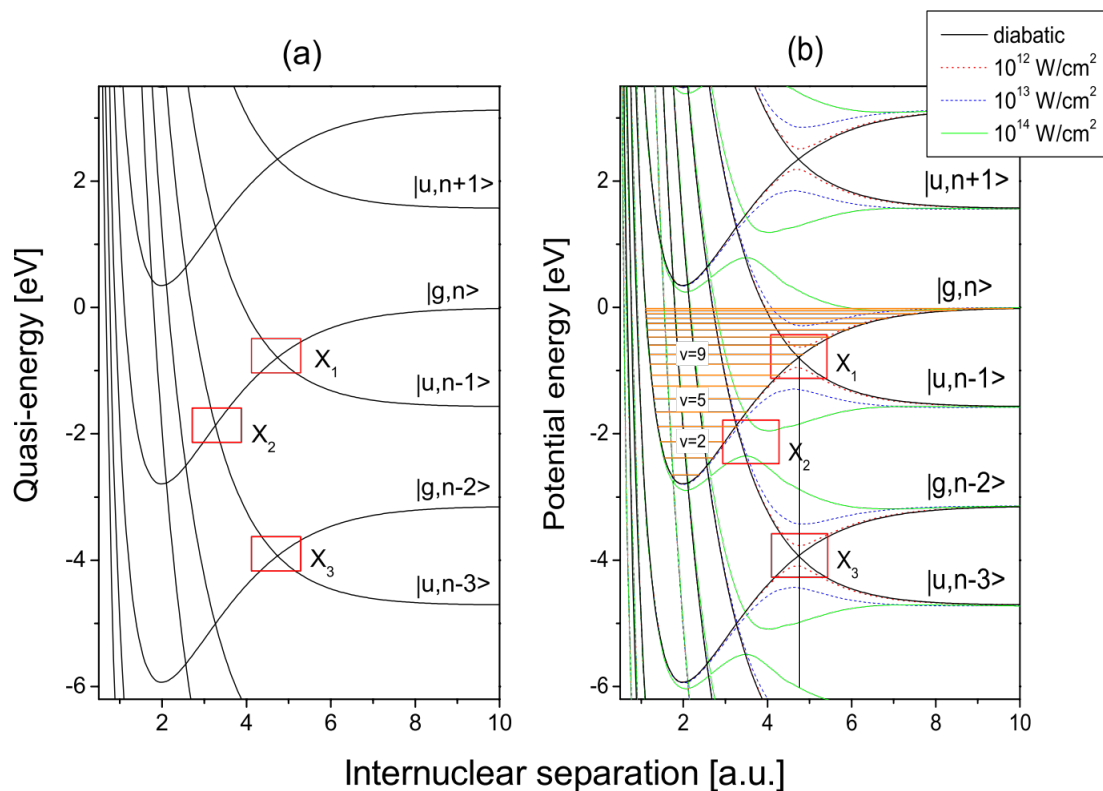


Figure 3.3: Illustration of the Floquet picture. a) At vanishing laser intensities, the molecular system can be described by diabatic potential curves, corresponding to $1s\sigma_g$ and $2p\sigma_u$. These potential curves are shifted by the number of absorbed photons $n=1,2,3,\dots$ creating crossing points marked with red boxes. b) At non-vanishing laser intensities, avoided crossings occur as a result of the coupling of gerade and ungerade states. As a consequence, adiabatic potential curves are formed. These potential curves for three different intensities are shown. Figure taken from [92]

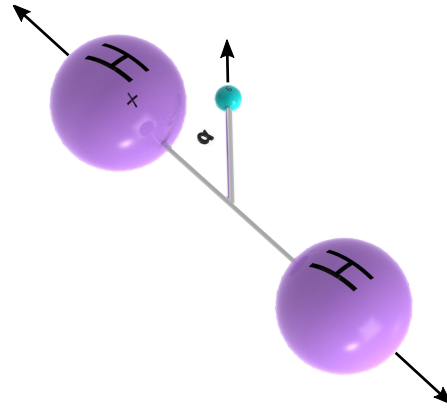


Figure 3.4: Schematic of dissociation of molecular hydrogen. The two nuclei dissociate in a nearly back-to-back fashion because of the relative light electron mass. α is the angle between the emitted electron and the molecular axis.

3.8 Electron Localization

In dissociation of H_2



the emitted electron can be either on proton side or H side, as shown in figure 3.4. This can be determined with the relative angle α between the emitted electron and the molecular axis. A localization parameter (asymmetry) can be defined as

$$A = \frac{N_{\alpha < 90} - N_{\alpha > 90}}{N_{\alpha < 90} + N_{\alpha > 90}} \tag{3.32}$$

where $N_{\alpha < 90}$ and $N_{\alpha > 90}$ are the number of cases where proton and electron are emitted in the same hemisphere ($\alpha < 90$) and the opposite one respectively ($\alpha > 90$). A asymmetry occurs when there are two pathways leading to the same final state as a result of a coherent superposition of two different electronic wave functions which have acquired unequal phases along those two pathways. The final state must be the same, photon energy sharing must be identical so that the fragments are not distinguishable, and the symmetry of emitted electron partial waves must be different. i.e. a *gerade* and *ungerade* electronic state couple as one can see from Eq. (3.33) and Eq. (3.34).

$$\tag{3.33}$$

$$(3.34)$$

According to above two equations, a coherent superposition leads to the fact that the electron is localized either on the left or right sided of the nucleus. To translate localization into quantum mechanics language, one can start by defining the wave function of the final state as

$$|\Psi_f\rangle = c_1 |\phi_1\rangle + c_2 |\phi_2\rangle \quad (3.35)$$

which is the superposition of two different states. Each state corresponds to the product of the total orbital angular momentum of the bound electron labeled with capital Greek letters $\Sigma \Pi \Delta, \dots$ and partial wave of the emitted electron (photo-electron) labeled with small Greek letters $\sigma \pi \delta, \dots$.

By defining a set of basis as follows

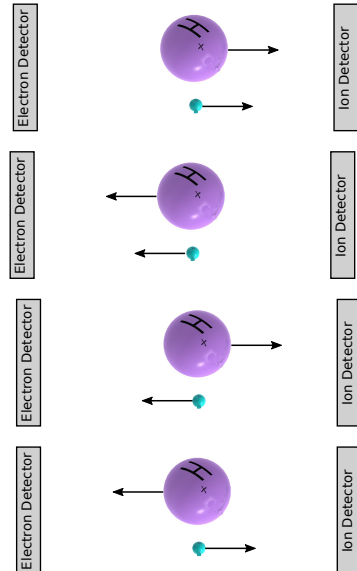
$$\begin{aligned} |H_{right}^+\rangle &= |\Lambda_1\rangle + |\Lambda_2\rangle & |H_{left}^+\rangle &= |\Lambda_1\rangle - |\Lambda_2\rangle \\ |e_{right}^-\rangle &= |\lambda_1\rangle + |\lambda_2\rangle & |e_{left}^-\rangle &= |\lambda_1\rangle - |\lambda_2\rangle \end{aligned} \quad (3.36)$$

$$|\psi_{pro}^1\rangle = |H_{right}^+\rangle \otimes |e_{right}^-\rangle$$

$$|\psi_{pro}^2\rangle = |H_{left}^+\rangle \otimes |e_{left}^-\rangle$$

$$|\psi_{anti}^1\rangle = |H_{right}^+\rangle \otimes |e_{left}^-\rangle$$

$$|\psi_{anti}^2\rangle = |H_{left}^+\rangle \otimes |e_{right}^-\rangle$$



(3.37)

the transition coefficients can be calculated by projecting the different cases in above equation onto the final state

$$\begin{aligned}
 |\langle \psi_{pro}^1 | \psi_f \rangle|^2 &= (c_1 + c_2)(c_1^* + c_2^*) \\
 |\langle \psi_{pro}^2 | \psi_f \rangle|^2 &= (-c_1 - c_2)(-c_1^* - c_2^*) \\
 |\langle \psi_{anti}^1 | \psi_f \rangle|^2 &= (-c_1 + c_2)(-c_1^* + c_2^*) \\
 |\langle \psi_{anti}^2 | \psi_f \rangle|^2 &= (c_1 - c_2)(c_1^* - c_2^*)
 \end{aligned} \tag{3.38}$$

By definition

$$\begin{aligned}
 N_{pro} &= |\langle \psi_{pro}^1 | \psi_f \rangle|^2 + |\langle \psi_{pro}^2 | \psi_f \rangle|^2 \\
 N_{anti} &= |\langle \psi_{anti}^1 | \psi_f \rangle|^2 + |\langle \psi_{anti}^2 | \psi_f \rangle|^2
 \end{aligned} \tag{3.39}$$

by putting them in Eq. 3.32 and after some lengthy calculations one obtains (for the full derivation see [104])

$$A = \frac{2Re[c_1 c_2^*]}{|c_1|^2 + |c_2|^2}. \tag{3.40}$$

This equation will be used in chapter 7 to simulate the observed experimental effects.

Chapter 4

Experimental Setup

The Attolab at MPIK was designed and constructed in the framework of this thesis. In the first part, the commercial laser system is presented. Secondly, the Mach-Zender interferometer is explained. Eventually, the principle of the Reaction Microscope is discussed.

4.1 Laser System

The laser is a commercially-available high-power fiber laser made by Active Fiber Systems GmbH [105] [106]. Figure 4.1 shows schematics of the laser CPA (chirped pulse amplification) amplifier system operation at three different repetition rates, namely 50, 70, and 150 KHz with a pulse duration of 250 fs and a pulse energy of 2 mJ. In the following step the 250-fs pulses are further compressed using two hollow-core fibers in series, as shown in Figure 4.2. After the first compression stage, pulses are compressed down to 40fs with 1.2 mJ pulse energy. The second compression stage reduces the pulse duration to sub 8 fs with 0.8 mJ pulse energy. In the following table, different outputs with the corresponding pulse energies are given

Pulse Duration (fs)	250	40	<8
Pulse Energy (mJ)	2	1.2	0.8

4.2 Interferometer

An interferometer with a nanometer resolution is needed to do time-resolved experiments on an attosecond time scale. Since most experiments are performed for more than couple

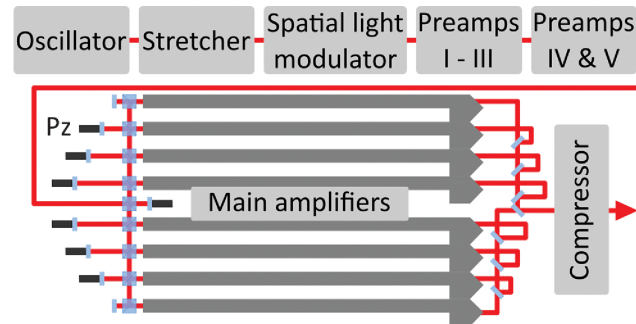


Figure 4.1: Schematic of the main amplifier of the laser (CPA) producing pulses with a duration of 250 fs. Figure take from [105]

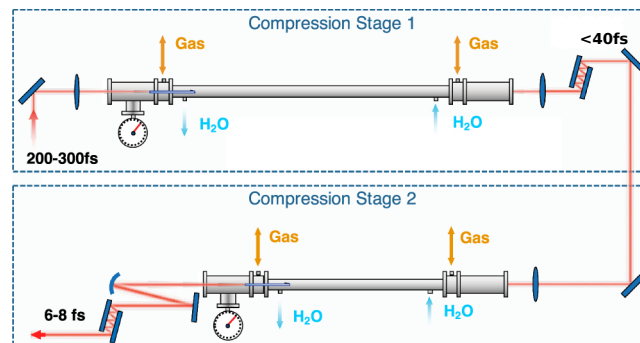


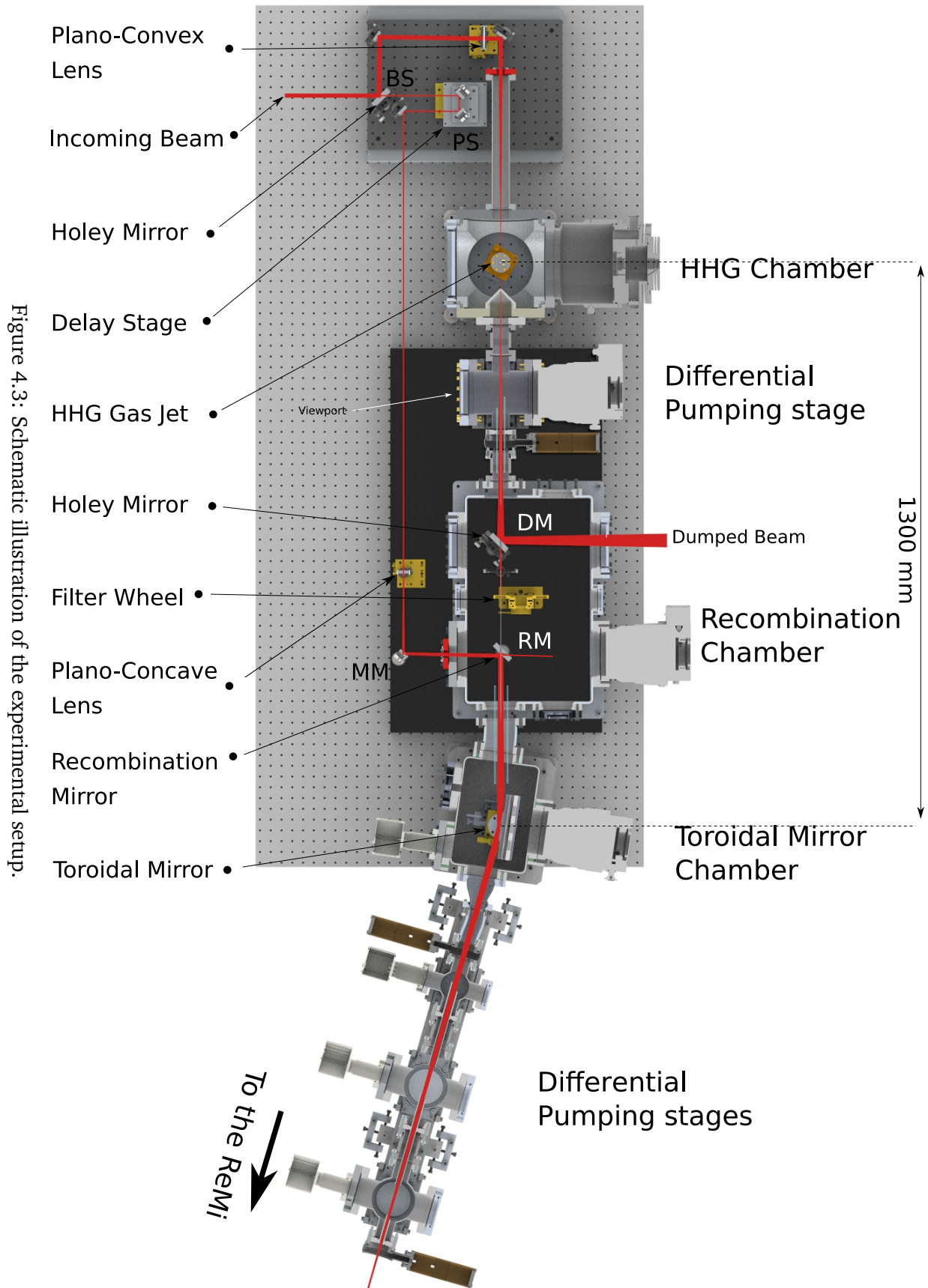
Figure 4.2: Schematic of the laser system nonlinear compression unit. Lang pulses after the CPA amplifier are fed into the first hollow-core fiber filled with argon with a pressure of 1.8 bars. Compressing the pulse length down to 40 fs using a series of chirped mirrors. Pulses are even further compressed in the second hollow core fiber filled with argon at a pressure of 2 bars. After chirp compensation, pulses of a duration of less than 8 fs are produced. Figure take from [105]

of hours to even couple of days, both short- and long-term stability of the interferometer is essential. For this purpose, during the design of the new Attolab, many efforts were targeted to create an ideal environment for high-precision experiments. The laser and the optical setup is located in a separate room, fulfilling clean room ISO 4 class, where, for example, the temperature is regulated with 0.1 degree precision. The interferometer with a Mach-Zehnder configuration, as shown in Fig. 4.3, is built with the minimum number of reflections, and as short as possible. A measurement of the stability of the interferometer is given in Fig. 5.9. In the following the individual components of the interferometer are explained.

The incoming laser beam with a diameter of 8 mm ($1/e^2$) is split into two arms, using a holey mirror with a hole diameter of 3 mm. The reflected holey beam (the pump arm with 85 % of the incoming intensity) is used to produce XUV light using HHG. The remaining 15 % (probe arm) is delayed with a translation stage. The pump arm is focused with the help of a plano-convex lens with a focal length of 500 mm. Afterwards, the beam goes then through a 1-mm thick glass and enters the vacuum chamber. A gas nozzle is placed at the focus of the pump beam. The nozzle is fixed on four different motorized stages, as shown in Fig. 4.4. In section 4.2.1, high harmonic generation is explained in more detail.

After the production of XUV, at a distance of 50 mm from the HHG gas target, a skimmer with a opening diameter of 2 mm separates the HHG chamber from the first differential pumping stage where the pressure is reduced from $4 \cdot 10^{-2}$ mbar, in the HHG chamber, to $2 \cdot 10^{-4}$ mbar. This differential stage is placed on an adjustable base allowing to move the whole chamber in order to align the beam through the small tube which separates this section from the recombination chamber. This tube has a diameter of 20 mm and a length of 250 mm. The entrance side of the tube is cut under 45° allowing the alignment of the chamber by looking through the view port from outside. In the recombination chamber the pressure is reduced to $1 \cdot 10^{-6}$ mbar. A mirror (labeled as DM) with a diameter of 4 mm is placed at the entrance of the recombination chamber which reflects most part of the incoming IR beam while letting through the XUV beam, which at this point is much smaller in diameter than the IR beam due to its divergence. The reflected IR beam goes through a viewport and is dumped outside the chamber. An iris after DM blocks further the co-propagating IR beam until the aluminum filter with a thickness of 200 nm, placed on a adjustable filter wheel, blocks completely the IR beam. The remaining XUV beam goes through the recombination mirror (labeled as RM) where the two arms of the interferometer are recombined.

In the probe arm, the small beam, going through mirror BS, hits a retro-reflector placed on a nano positioning piezo stage made by Physical Instrument (P-629.1CL) which is used to introduce a path length difference between the two arms of the interferometer. The piezo stage is driven with an external signal generator with a triangle waveform which is also sent to the data acquisition system as a reference for the time delay. In order to reach the same beam divergence to match the one in the pump arm, the probe beam is focused using a plano-concave lens with a focal length of -25 mm so that the virtual focus



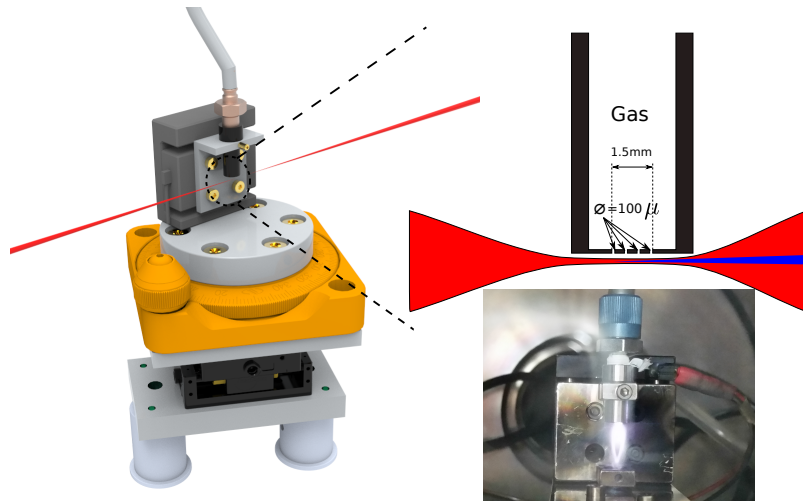


Figure 4.4: Schematic illustration of the HHG nozzle mount. The nozzle is fixed of a vertical piezoelectric stage. A rotational stage is placed underneath on top of two horizontal piezo stages used to move the target along and perpendicular to the laser beam direction. A HHG target is shown with four holes each with a diameter of 100 micrometer. A picture of the produced plasma in argon is shown at the focus of the laser beam.

is at the same distance from the recombination mirror as is the focus of the probe arm at the HHG target. The probe beam is then reflected through the recombination chamber using the motorized mirror MM, and recombines eventually with the XUV beam. The RM mirror has two co-centric holes letting through a small part of the probe beam used later for diagnostic purposes.

After recombination, two beams go through a small tube which separates the recombination chamber from the toroidal mirror chamber so that the pressure can be even further reduced by another order of magnitude. The recombined beam then hits the toroidal mirror at a grazing incidence of 8 degrees. The toroidal mirror has a $2f-2f$ configuration and has a B_4C coating (the specifications are given in Appendix E). The mirror is mounted on a combination of four different motorized stages, as shown in Fig. 4.5. With the help of these stages one can optimize the focus of the beam inside the ReMi. So as to reduce the pressure at this stage ($1 \cdot 10^{-7}$ mbar) to reach pressures comparable to ones in the ReMi, a series of differential pumping stages are implemented to reach a pressure in 10^{-11} mbar regime at the entrance of the ReMi. All differential stages are each mounted on an adjustable base allowing the adjustment of the beam through the small tubes between them.

In order to ensure the temporal and spatial overlap, a removable mirror is mounted on the back side of the ReMi reflects the beam to a camera. This serves as a rough initial alignment. A more precise alignment is done with the ReMi. Due to the high flux of the XUV light in the ReMi a tube with a length of 1.5 meters and a diameter of 40 mms is attached at the end of ReMi to dump the XUV photons.

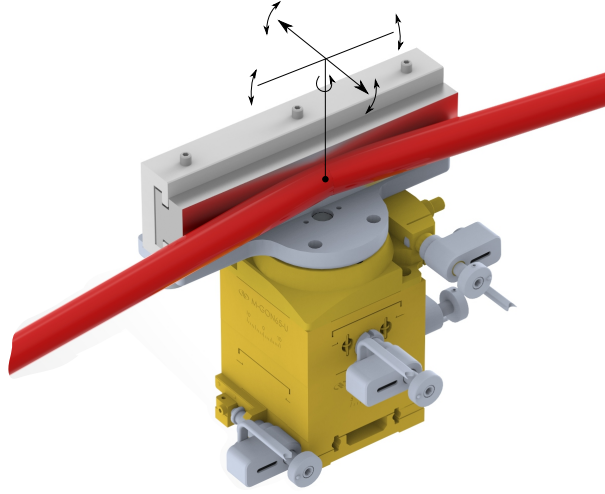


Figure 4.5: Schematic illustration of the toroidal mirror mount. The mirror is placed on four different stages. The lowest stage is a translation stage moving the whole mirror on the sagittal plane. Two goniometers are used to move the mirror around the center of the mirror, illustrated with a black circle. The upper-most stage rotates the mirror around the central point.

4.2.1 High-Harmonic Generation (HHG)

In the pump arm of the interferometer, the incoming beam before the focusing lens has a diameter of 8 mm ($1/e^2$). After focusing with a plano-convex lens with a focal length of 50 cm, the focal spot size is almost $80 \mu\text{m}$. There is a gas nozzle mounted on four different motorized stages. For all experiments in this thesis argon is used as the HHG target gas. The backing-pressure of the nozzle is almost 1 bar. With the help of a vacuum turbo pump (Leybold Turbovac 350i) and a Pfeiffer Ontool booster 150 the pressure in the HHG chamber is kept at around 4.10^{-2} mbar. To have an estimate of the number of the photons and conversion efficiency, one can use the photoionization rate in the ReMi to calculate the number of XUV photons. The number of photons per second per unit area is given by:

$$\phi = \frac{R}{Ln\sigma\eta}, \quad (4.1)$$

where R is the photoionization rate, L is the interaction length, n is the density of the target, σ is the cross section of the target, and η is the detection efficiency. As a reference argon was used as HHG target gas, and helium as the ionization target in the ReMi. The XUV was produced with the holey beam. The power before the HHG target was measured to be 38 W corresponding to 0.8 mJ pulse energy. No aluminum filter was used, and the XUV beam was focused with the toroidal mirror into a gas jet of helium in the ReMi. A count rate of 18 kHz was measured at 47 kHz laser repetition rate. By taking into account

the photoionization cross-section of helium [107]¹, the interaction length (2 mm), gas jet density (10^{11} atoms/cm³), and 40% detection efficiency², 10^{11} photons/s corresponding to 10^7 photon/pulse have been reached which is comparable to values in literature [106]. A spectrum of the XUV pulse is given in Fig. 2.5.

¹4 Megabarn (10^{-18} cm²) was used as an average over the energy range available in the XUV spectrum.

²The MCPs used in the ReMi has a maximum detectable area of 60 %, meaning if each particle is detected the detection efficiency will be 60 %. The factor of age (MCPs used during this measurement were 12 years old) and particle type and velocity results in an final detection efficiency estimation of 40 % which is still an overestimation.

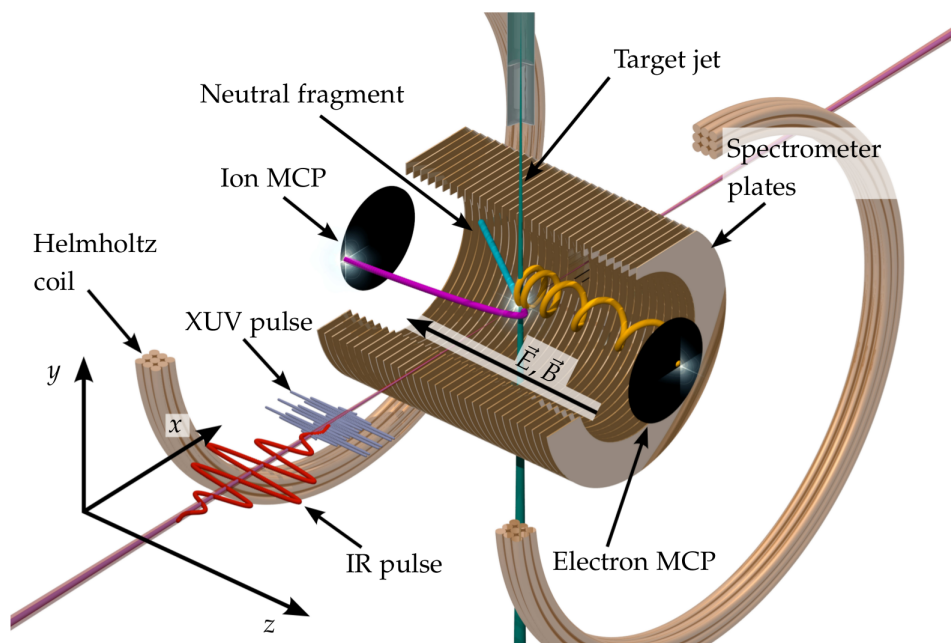


Figure 4.6: Schematic illustration of a reaction microscope (ReMi). Figure taken from [110]

4.3 Reaction Microscope

A multi-particle coincidence spectrometer which is known as the Reaction Microscope (ReMi) [108] [109] is a powerful tool in atomic and molecular physics. The spectrometer detects charged reaction fragments with a solid-angle acceptance of 4π . By using the time of flight and hit position on its detectors, one can reconstruct the initial momentum vectors in 3 dimensions. The coincident measurement nature of the ReMi can be exploited to determine the reaction channels. A ReMi is shown schematically in Fig 4.6. A laser beam is focused onto a supersonic gas jet passing through the center of the spectrometer. Electrons and ions are collected and guided towards the detectors with a help of a magnetic and an electric field. In the following sections different parts of the ReMi is introduced and the working mechanism, and momentum reconstruction are explained.

4.3.1 Supersonic Gas Target

Most experiments with ReMi are done on targets in the gas phase. At the room temperature the mean kinetic energy of gas particles is 25 meV ($k_B T$). Because of this, it is necessary to cool down the target to improve the momentum resolution. One needs also

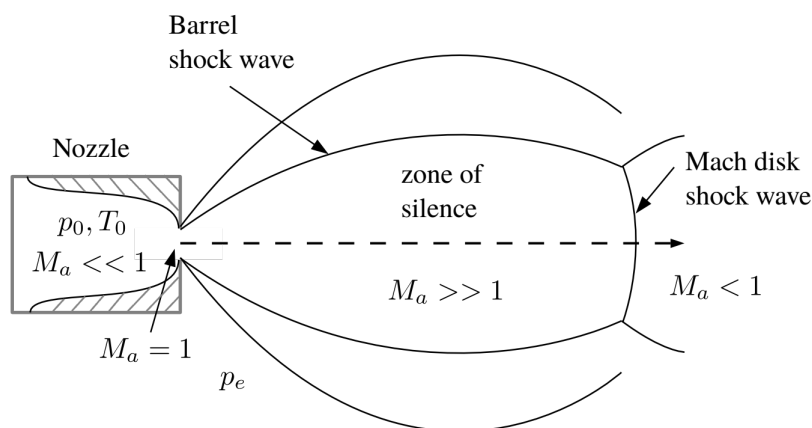


Figure 4.7: The gas initially is flowing slowly in a region with pressure p_0 and temperature T_0 resulting in a very small Mach number ($M_a \ll 1$). The gas expands into a region with pressure p_e where $p_e \ll p_0$, and, as a consequence, the particles are accelerated along the pressure gradient shown with the dashed arrow. Under the assumption that the heat conduction and friction can be neglected, an isentropic process takes place where the entropy is constant. Gas particles travel at the speed of sound if $M_a = 1$ corresponding to $\frac{p_0}{p_e} = 2.1$. For higher backing pressures, the gas expands in the form of shock waves to reach pressure balancing giving rise to the creation of a zone of silence. In this region the gas velocity exceeds that of sound. Spatial density reduction is therefore compensated through the increase in density in momentum space eventually leading to temperature reduction. Figure taken from [111].

a small fixed interaction region so as to be able to reconstruct the momenta, as explained in section 4.3.3. In order to fulfill these requirements, a supersonic gas jet is used to reach a temperature of few Kelvins. The mechanism of a supersonic gas jet is as follows: A gas is expanding into a reservoir through a very small nozzle of $30 \mu\text{m}$ from a high pressure region with pressures of the order of few bars into a low pressure region of a few millibars resulting in a supersonic expansion, as shown in Fig. 4.7. The gas jet setup is shown in Fig. 4.8. The gas at the room temperature is expanded through a small hole with a diameter of $30 \mu\text{m}$ into the first jet stage. A skimmer with an opening of $150 \mu\text{m}$ separates the jet stage 1 from jet stage 2. The second skimmer with an opening of $200 \mu\text{m}$ lets the gas beam into the main chamber of the ReMi.

4.3.2 Spectrometer and Detectors

The function of the spectrometer is to produce a homogeneous electric field to guide the charged particle towards the detectors. The homogeneity of the field is an important factor

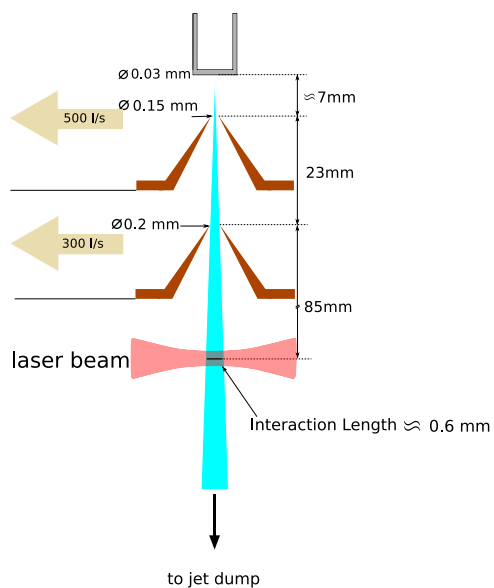


Figure 4.8: Schematic illustration of the gas jet in the reaction microscope.

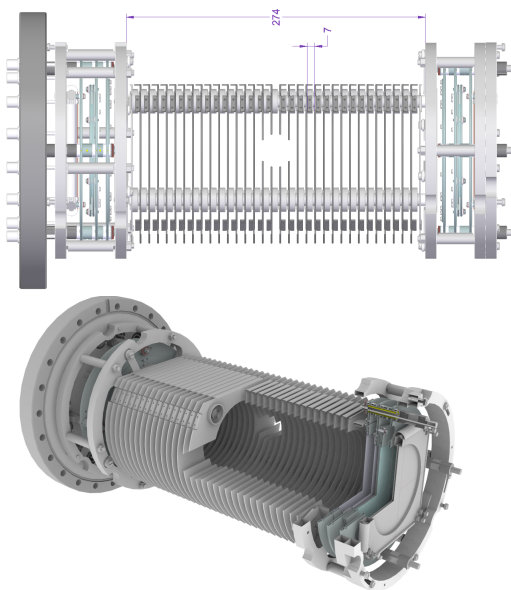


Figure 4.9: Drawing of the reaction microscope spectrometer with a total length of 274 mm . The distance between spectrometer electrodes is 7 mm .

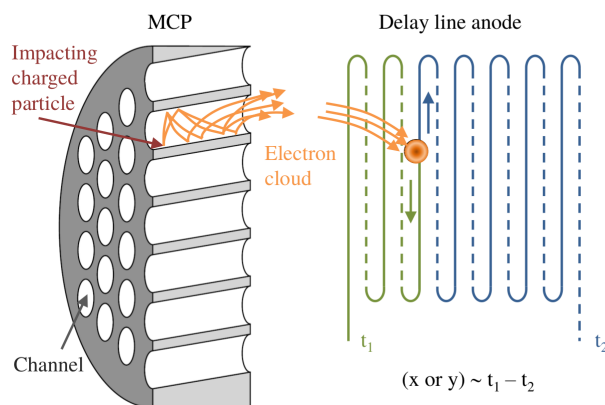


Figure 4.10: Schematic illustration of an MCP and delay-line anode. Figure taken from [113].

in order to achieve a proper momentum resolution. The whole length of the spectrometer is composed of 32 plates with a spacing of 7 mm, as shown in Fig. 4.9. For more details about the spectrometer see [112].

The hit position and the time of flight are determined using MPCs (multichannel plates) [114] with a combination of a delay line anode [115]. As for MCPs, they consist of arrays of very small channels with a diameter of couple micrometers, as shown in Fig. 4.10. The inner surface is coated with, for instance, GaP or GaAsP allowing the production of secondary electrons, upon bombardment with particles, due to their low work function. By applying a voltage on both sides of an MCP, electrons can be accelerated and hit the inner surface again resulting in an electron avalanche similar to photo-multipliers. As a consequence, a voltage drop takes place between two sides of the MCP is used to determine the hit instance (t_{MCP}) or the detection time of a particle resulting from an interaction with the laser pulse. The interaction instance (t_{laser}) or the interaction time is also known. Eventually, the TOF can be determined using

$$TOF = t_{MCP} - t_{laser}. \quad (4.2)$$

The channels of an MCP are slightly tilted to increase the detection efficiency. Normally, two or three MCPs are stacked upon each other which improves also the detection efficiency.

The hit position is determined using a delay-line anode, consisting of meshes of copper wire, placed behind the MCP [116]. The electron cloud leaving the back side of the MCP hits its wires. Delay-line anode is positively biased with respect to the back side of the MCP to guide the electrons. Once an electron cloud hits the delay-line anode, a signal is produced which travels with constant velocity v towards both ends of the wire, as shown in Fig. 4.11. The position can be determined by the arrival time of these signals

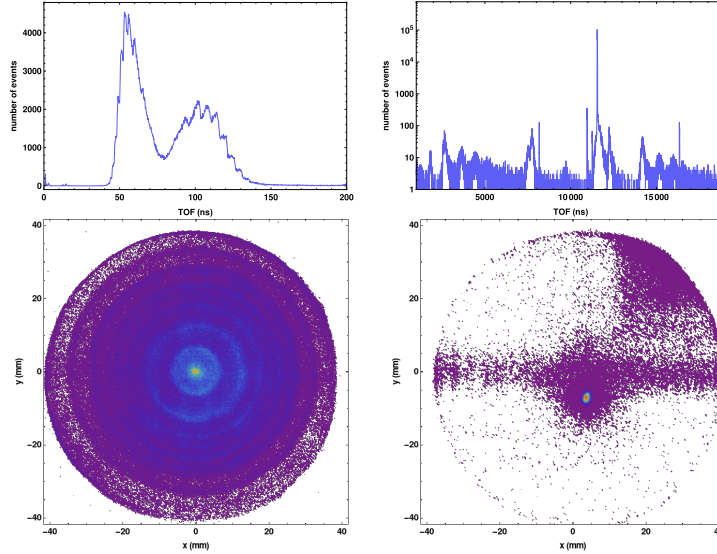


Figure 4.11: Upper left panel shows the TOF spectrum for electrons. Lower left hit positions on the electron detector. Upper right the TOF spectrum for ion and lower right hit positions for ions. From hit and TOF one can reconstruct all momenta vectors.

$$x = \frac{v}{2}(t_1 - t_2). \quad (4.3)$$

by adding another set of wire perpendicular to the existing one, (x, y) coordinates of an hit can be determined.

4.3.3 Momentum Reconstruction

In the following, reconstruction of the three initial momentum vectors is explained using the TOF and impact position on the detectors. Time of flight of charged particles depend on the charge and mass of particles as well as the initial velocity, acceleration region, and extraction voltage. One can use the cylindrical coordinates in order to facilitate the momentum calculations. As it is shown in Fig. 4.6, the longitudinal direction is along the z axis which is the time of flight axis as well. Using the Lorentz force and Newton's second law of motion, one can describe the motion of a charged particle in a magnetic and electric field.

$$m \cdot \vec{a} = q \cdot (\vec{E} + \vec{v} \times \vec{B}), \quad (4.4)$$

where m and q are mass and charge, and E and B are the electric and magnetic field respectively. One can neglect the effect of the magnetic field on ions. The above equation can be simplified to

$$a = \frac{qE}{m} = \frac{qU}{mL}, \quad (4.5)$$

where U is the voltage applied over the length L which is given by

$$\begin{aligned} L &= \frac{1}{2}at^2 + v_z t, \\ &= \frac{1}{2} \frac{qU}{mL} t^2 + v_z t, \end{aligned} \quad (4.6)$$

where t is the time it takes for ions to reach the detector from the interaction point, known as *time of flight*. One can rewrite the above equation in terms of the longitudinal momentum (of an ion or an electron) ($p_z = mv_z$)

$$p_z = \frac{Lm}{t} - \frac{qUt}{2L}, \quad (4.7)$$

and in atomic units (*a.u.*)

$$p_z = 8.043 \times 10^{-3} \frac{qU}{L} \Delta t. \quad (4.8)$$

Solving for t in the above equation

$$t = \frac{2Lm}{\sqrt{p_z^2 + 2mqU} \pm p_z}. \quad (4.9)$$

Transversal Momentum

In case of ions, the transversal momentum (p_1) is calculated from the hit position on the detector and the time of flight. One can neglect the effect of the magnetic field resulting in

$$p_1 = \frac{rm}{t}, \quad (4.10)$$

where the hit position r is given by

$$r = \sqrt{(x - x_0)^2 + (y - y_0)^2}, \quad (4.11)$$

where x_0 and y_0 are the position of an ion with zero transversal momentum. As it can be seen in Fig. 4.11, ions manifest a shift in y-direction relative to the center of the detector caused by the initial gas velocity in the jet. This can be accounted for by choosing the

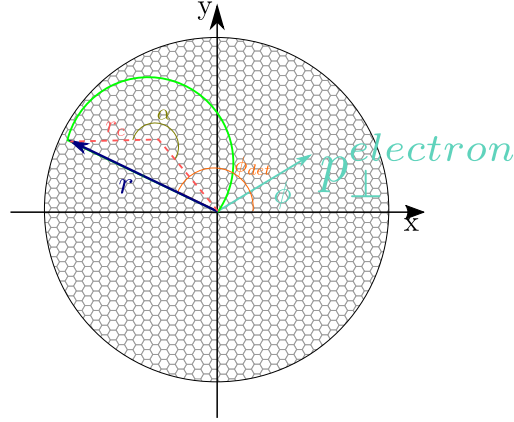


Figure 4.12: Schematic of the electron trajectory in a plane perpendicular with respect to the spectrometer axis.

center of the distribution as (x_0, y_0) instead of the center of the detector. The emission angle in xy -plane is given by

$$\phi_{\perp} = \arctan \frac{(y - y_0)}{(x - x_0)}, \quad (4.12)$$

and transversal momentum components are

$$p_x = \frac{(x - x_0)m}{t}, \quad \text{and} \quad p_y = \frac{(y - y_0)m}{t}. \quad (4.13)$$

In case of electrons, momentum reconstruction is more complicated, for the presence of the magnetic field causes electrons to undergo cyclotron motion. Using equation 4.4 and the centrifugal force ($F = m \frac{v_{\perp}^2}{r_c}$)

$$\frac{mv_{\perp}^2}{r_c} = ev_{\perp}B \implies p_{\perp} = er_cB, \quad (4.14)$$

where r_c is the radius of cyclotron motion, e is the electron charge, and B is the magnetic field. One can not detect r_c . However using Fig. 4.12, a relationship between r and r_c is given by

$$r_c = \frac{r}{2 \sin(\alpha/2)}, \quad (4.15)$$

where $\alpha = \omega_c t$ with ω_c being the cyclotron frequency. By combining Eq. 4.14 and Eq. 4.15, electron transversal momentum is given

$$p_{\perp} = \frac{erB}{2|\sin(\alpha/2)|}. \quad (4.16)$$

The azimuthal angle of emission can be calculated using the detection angle ($\phi_{det} = \arctan(y/x)$)

$$\phi = \phi_{det} - \frac{w_c t}{2}. \quad (4.17)$$

4.3.4 Spectrometer Acceptance

The acceptance of the spectrometer is the maximum detectable kinetic energy of a fragment emitted in a particular direction. The limitation is due to the geometry and applied voltages of the spectrometer because a charged particle moving away from the corresponding detector has to be driven back to the detector. If the deceleration length is not enough, the particle trajectory exceeds the spectrometer length, and therefore, can not be detected. The maximum detectable longitudinal momentum for a particle with the mass of m and charge of q is given by

$$p_{max}^{\parallel} = \sqrt{2mqU}, \quad (4.18)$$

where U is the applied voltage. As for photo-ionization of atoms with photon energies accessible in the scope of this work, the momenta of ions hardly exceed 2 a.u. However, molecular fragmentation can result in higher energetic particles. For example, fragments resulting from dissociation of molecules can have a momentum up to 45 a.u..

In the case of the transversal acceptance, unlike the longitudinal one, ions and electrons have to be considered separately as they are affected differently by the magnetic field. Regarding ions, the transversal acceptance on a detector with a radius of R_{det} at a distance of L from the interaction point is given by

$$p_{max}^{\perp} = R_{det} \frac{\sqrt{2mqU}}{2L}. \quad (4.19)$$

Concerning electrons, maximum transversal momentum is given by

$$p_{max}^{\perp} = BR_{det}. \quad (4.20)$$

where B is the magnetic field.

4.3.5 Momentum Resolution

Momentum resolution of the detected particles is influenced by a number of factors. Firstly, inhomogeneities in both magnetic and electric field. Furthermore, there is an intrinsic uncertainty in the detection of the position and time of flight. Furthermore, gas

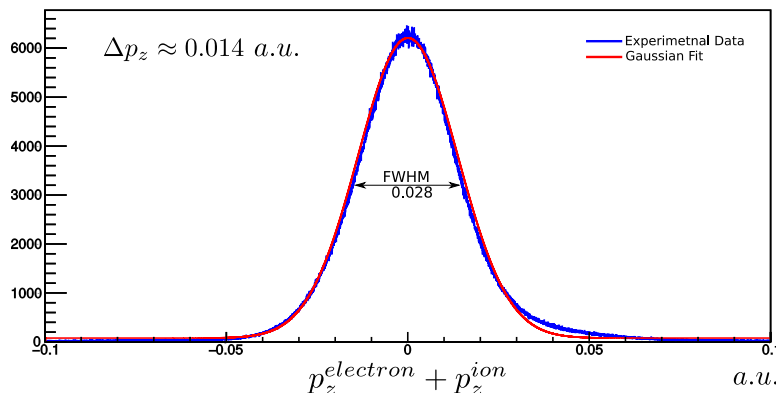


Figure 4.13: Sum of longitudinal momentum of electrons and ions in atomic units in the single ionization of H_2 . Momentum resolution is given by $FWHM/2 = 2\sqrt{2 \ln 2} \sigma$ where σ is the standard deviation. The extraction voltage is 50 V.

jet temperature related momentum uncertainty, and the extent of the interaction region are other contributing factors. Generally the momentum sum of detected particles from single-ionization is used as a measure of the momentum resolution. For instance, the sum of $p_x^{electron} + p_x^{ion}$ is shown in Fig. 4.13. A Gaussian fit is used to determine the width of the distribution ($\Delta p_z \approx 0.014$). The same procedure for the other two momentum components in the case of single-ionization of H_2 results in $\Delta p_x \approx 0.14$ a.u. and $\Delta p_y \approx 0.57$ a.u. at 50 V extraction voltage.

4.3.6 Molecular Frame

Based on the assumption of axial recoil approximation [117] molecular dissociation happens on a much faster time scale compared to molecular rotation (see timescale of H_2 molecule 3.1). Consequently, the detected recoil direction is the same as the dissociation direction at the moment of dissociation. In the first step all detected fragments are in the laboratory frame (LF). In the case of the dissociation of a diatomic molecule AB , molecular frame (ML) can be reconstructed using the momenta of the detected ion A^+ and electron e^-

$$\hat{\mathbf{p}}_{MF}^{A^+} = \hat{\mathbf{p}}_{LF}^{A^+} + \left(\frac{M_B}{M_{AB}} \right) \hat{\mathbf{p}}_{LF}^{e^-}, \quad (4.21)$$

where M_{AB} is the mass of two nuclei. For H_2 , one has to add $\hat{\mathbf{p}}_{MF}^{H^+} = \hat{\mathbf{p}}_{LF}^{H^+} + \left(\frac{1}{2} \right) \hat{\mathbf{p}}_{LF}^{e^-}$, as illustrated in Fig. 4.15.

Chapter 5

Nuclear-Electron related Dynamics of H₂ and D₂

With photon energies available to us during these experiments (up to 40 eV), a number of interesting interactions in molecular hydrogen and its isotope, molecular deuterium can be studied. The corresponding potential curves for hydrogen molecule¹ are given in Fig. 5.1. The complexity of these simplest molecular systems is clear by looking at the potential curves. In this chapter, a time-resolved investigation of dissociative photo-ionization of both H₂ and D₂ is presented. This chapter is structured as follows: firstly, the results of the interaction of an attosecond pulse train (APT) consisting of XUV photons with H₂ and D₂ are presented in a quantitative manner and are compared with the available theory and experiments in the literature. Subsequently, the role of the IR pulse as a dressing field is explained. Furthermore, how the system under examination behaves as the delay between XUV and IR pulses varies, followed by vibrational-resolved investigations. Eventually, using the interferometric RABBIT technique, photo-dissociation processes are studied with attosecond precision leading to phenomena such as the effect of resonances on the phase of the photo-electrons, and how these phases change as a function of the internuclear distance which implies the intertwined electron-nuclear dynamics.

Both photo-ionization and photo-dissociation occur as H₂ and D₂ interact with an APT, as shown in the TOF spectrum, given in Fig. 5.2. The resulted electron spectra are shown in the top left corner of Fig. 5.3 as well as a schematic spectrum of an APT. Single-ionization with an XUV photon is explained in the coming section followed by photo-dissociation.

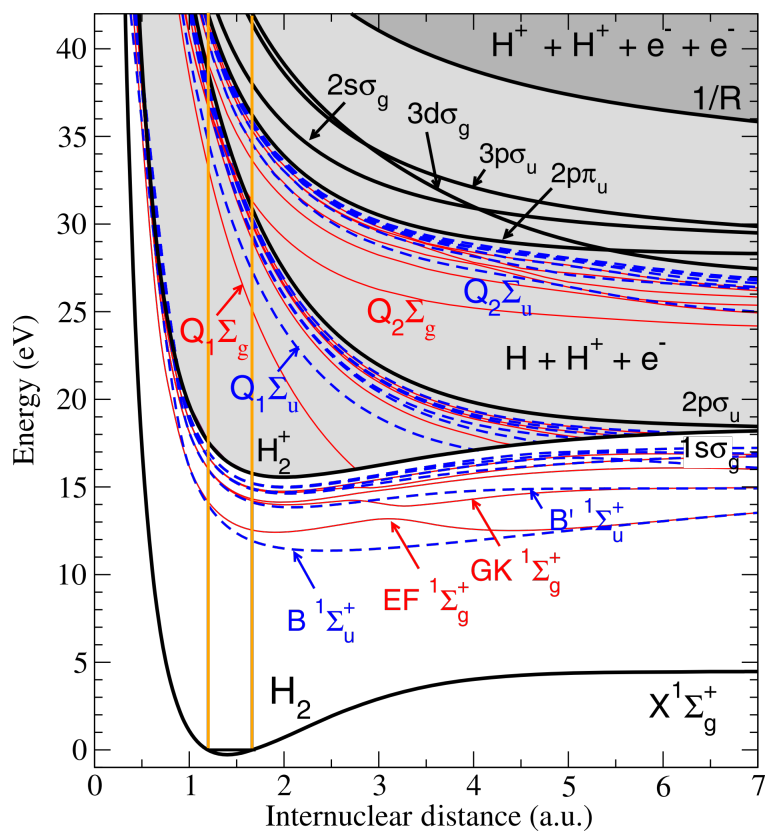


Figure 5.1: Potential energy curves showing neutral and ionic states of H_2 . Franck-Condon region is shown with orange vertical lines. Figure taken from [43].

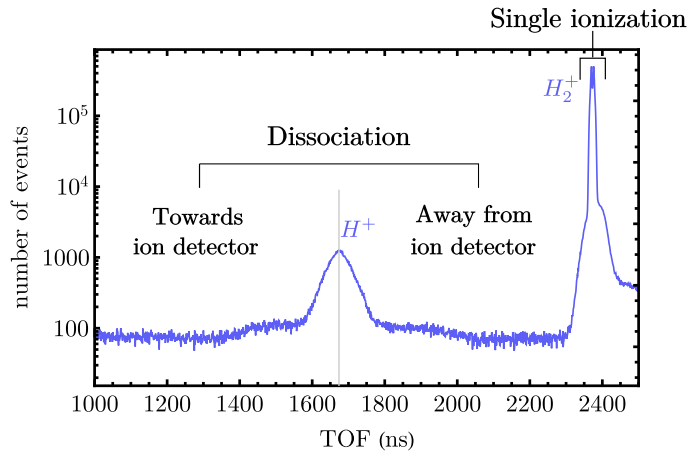


Figure 5.2: The Time of flight spectrum of the detected ions resulting from the interaction of an XUV pulse train with H_2 . The ratio $\frac{H^+}{H_2^+} = 0.02$. The dissociation region is spread over a much larger area compared to single-ionization. The center of the distribution is marked with a gray vertical line showing the zero energy protons.

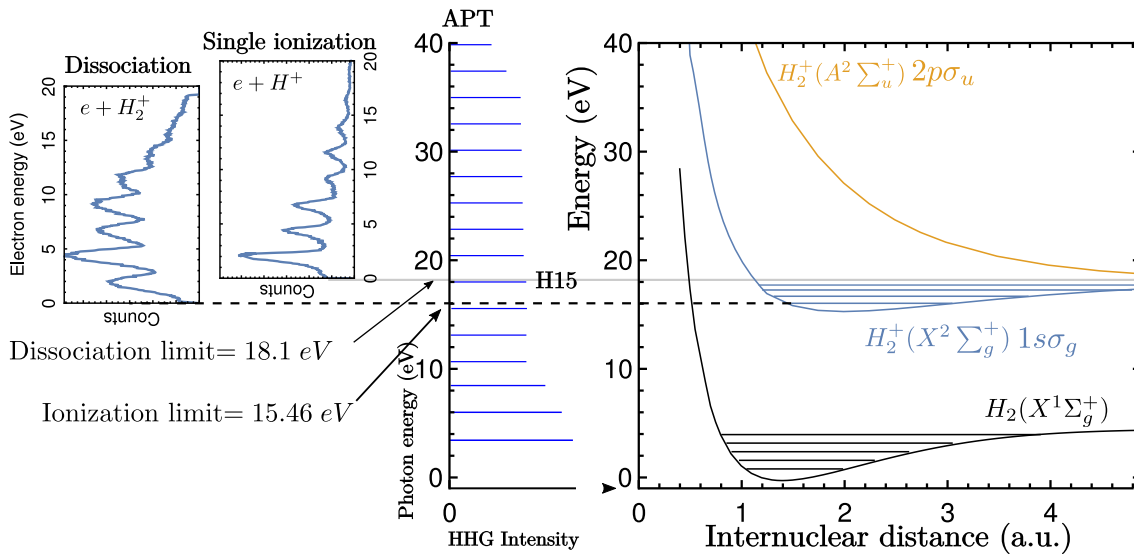


Figure 5.3: The interaction of an attosecond pulse train (APT) with H_2 . The potential energy curves of H_2 are given on the right side. The spectrum of the APT is given in the middle. The corresponding photo-electron spectra are given for both single ionization and dissociation channels in the top left corner. Photoionization (slightly above harmonic 13) and dissociation (slightly above harmonic 15) limits are marked with horizontal dashed and gray lines, respectively.

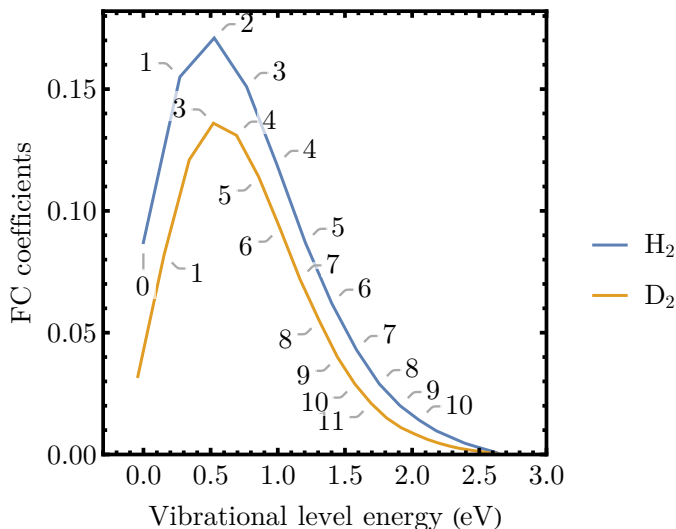


Figure 5.4: Franck-Condon coefficients for H_2 and D_2 . Numbers on the curves denote the vibrational state ν . Values taken from [118].

5.1 Single-photon Ionization of H_2 and D_2

The spectrum of an attosecond pulse train (APT) covers a range of energies from 15 to 40 eV. The peaks are separated by 2.42 eV and an energy width of 0.3 eV (FWHM) for each peak. Upon absorption of an XUV photon with energies higher than ² 15.46 eV [120], a dipole transition from $H_2(X^1\Sigma_g^+)$ ³ to the ground state of the cation ($H_2^+(X^2\Sigma_g^+)(1s\sigma_g)$) is possible resulting in the emission of an electron. Since the ground state potential curve of the cation is slightly displaced relative to the ground state of the neutral molecule, higher vibrational⁴ levels of $1s\sigma_g$ are coherently populated according to Franck-Condon factors, as illustrated in Fig. 5.4. This coherent superposition of vibrational states leads to the formation of a nuclear wave-packet (NWP). After the photo-ionization of the molecule, the energy of the emitted electron is given by

$$E_{e^-} = q\hbar\omega - E(1s\sigma_g, \nu), \quad (5.1)$$

where $E(1s\sigma_g, \nu)$ is the energy of the ν^{th} vibrational state of the cation relative to the ground state of the hydrogen molecule. Fig. 5.5 shows the detected photo-electron spectrum resulting from ionization with XUV light in coincidence with H_2^+ (blue curve) and D_2^+ (brown curve). Furthermore, the harmonic peaks are broader than that of the single-ionization of argon. The reason for this broadening is the last term in the above equation

¹ D_2 has the same potential curves

²Throughout this work all values given for H_2 are also valid for D_2 unless otherwise stated.

³The neutral H_2 and D_2 molecule are in the first vibrational ground state at room temperature ($\frac{1}{40}$ eV. $E_{\nu_0 \rightarrow \nu_1} = 0.5159$ eV for H_2 [76] and 0.371 eV for D_2 [121].

⁴Rotational energy levels can not be resolved with this experiment, and therefore are neglected.

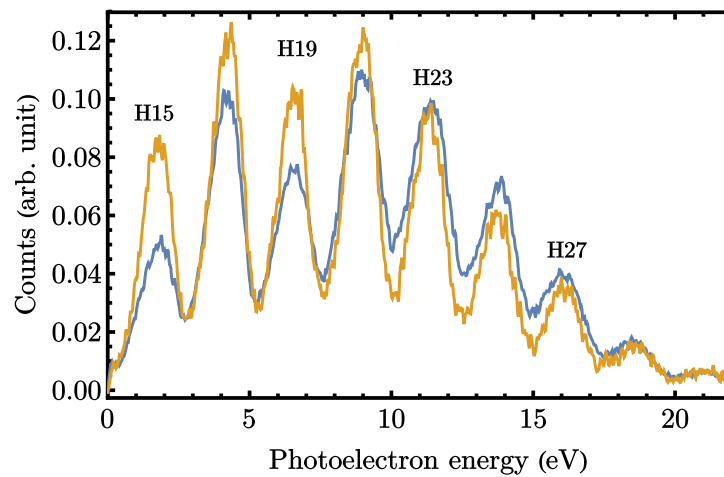


Figure 5.5: Photo-electron spectrum of H_2 , and D_2 as a result of ionization ($I_p=15.46$ eV) with XUV light. The first peak corresponds to harmonic 15. The difference between two spectra is due to the difference in the XUV spectrum, since these two measurements were not carried out at the same time. Additionally, the peak of harmonic 15 is smaller than that of harmonic 17 due to the presence of the aluminum filter in the XUV beam. Harmonic 25 denotes the cut-off frequency and, as a result, the intensity of higher harmonics decreases exponentially. Besides, the height of harmonic 19 is smaller than its two adjacent peaks. This effect is also present in the case of the single ionization of argon (Fig. 2.8), and therefore, is attributed to the spectrum of the XUV beam. The reason for this effect is not clear.

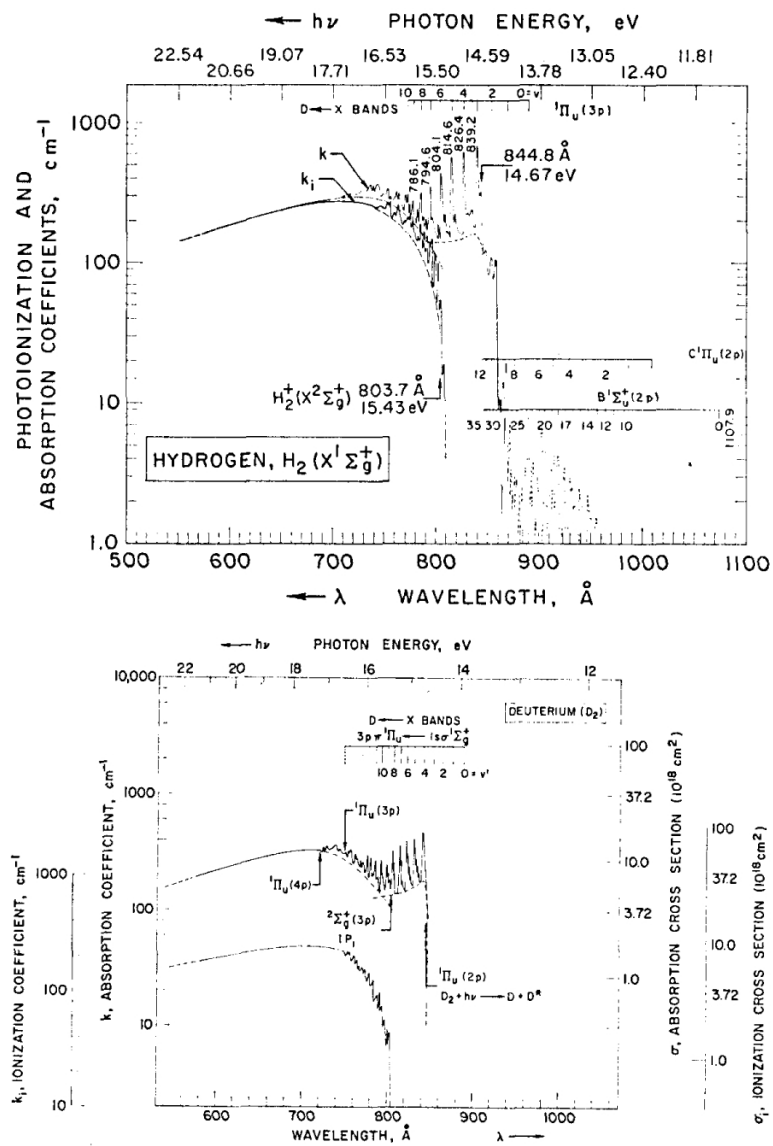


Figure 5.6: Photoionization cross section of H_2 (top), and D_2 (bottom). Figures taken from [119].

which follows the Franck-Condon distribution as opposed to atoms where this term is a constant value (ionization potential) leading to sharp photo-electron energy peaks in atoms. The width of each harmonic peak in the photo-electron spectrum in case of argon is around 300 meV (FWHM)⁵. Therefore, single vibrational level can not be resolved considering the fact that the spacing between vibrational levels are smaller (the largest one is for H₂⁺ where $E_{\nu_0 \rightarrow \nu_1} = 0.271 \text{ eV}$). One can, however, resolve vibrational levels with help of a probe pulse dissociating the molecule, as will be discussed in section 5.3. Moreover, the two spectra are not identical due to the fact that these measurements were not recorded at the same time (the XUV spectrum was not identical). Otherwise, one expects to observe the same photoelectron spectra, since H₂ and D₂ have a very similar photo-ionization cross section, as illustrated in Fig. 5.6. In addition, the intensity of harmonic 15 is smaller than the intensity of harmonic 17, since the aluminum filter was used in the XUV beam. Harmonic 25 marks the cut-off frequency, and, as a consequence, the intensity of higher harmonics decreases exponentially. Furthermore, the intensity of harmonic 19 is smaller than its two neighboring peaks. This feature is also present in the case of single ionization of argon (Fig. 2.8), and thus, is attributed to the spectrum of the XUV beam. The reason for this effect is not clear.

Photo-ionization of H₂ and D₂ with an XUV Pulse in the Presence of an IR Pulse (Photo-assisted ionization)

The ionization of H₂ and D₂ with XUV in the presence of IR is similar to that of atoms presented in 2.2. The photo-electron energy is given by

$$E_{e^-} = q\hbar\omega \pm \hbar\omega - E(1s\sigma_g, \nu), \quad (5.2)$$

where $q = 2n + 1, n = 0, 1, 2, \dots$ resulting in the appearance of sidebands, as depicted in Fig. 5.7. The sidebands are not as well-resolved as in argon (Fig. 2.8) due to the much broader harmonic and sideband peaks. One can, however, see that the valleys between harmonics become shallower as the peaks of harmonics become shorter. If the intensity of the IR beam is increased, at one point, none of the peaks are visible anymore. One also expects to see that the sidebands grow symmetrically in the middle as it is the case for higher sideband (SB 24, 26, 28). The reason for this asymmetric growth in lower sidebands (SB 16, 18, 20) is not clear.

RABBIT in H₂ and D₂

Similar to atomic cases, one can plot the photo-electron energy as a function of the delay between XUV and IR pulses which results in the appearance of sideband oscillations, as shown in Fig. 5.8. The frequency of this oscillatory pattern is 2ω , corresponding to a period of 1.7 fs.

⁵The detected width is the combination of the ReMi resolution and the bandwidth of the harmonic peaks.

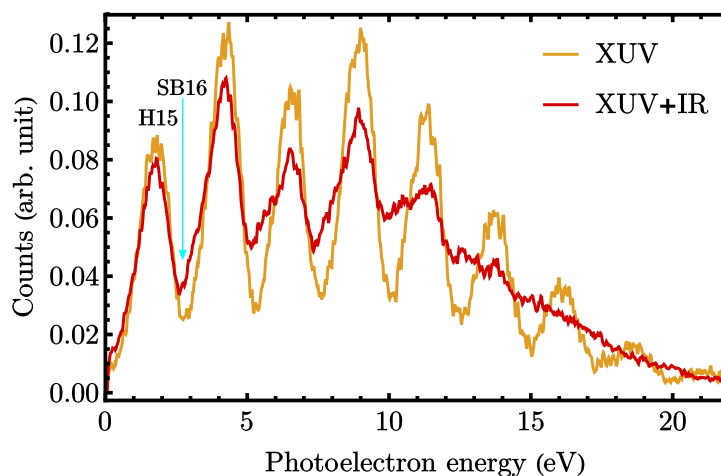


Figure 5.7: Photo-electron spectrum of D_2 with and without IR probe pulse. Sidebands begin to fill the space between harmonic peaks as the height of the harmonic peaks become smaller. The first harmonic and sideband are labeled.

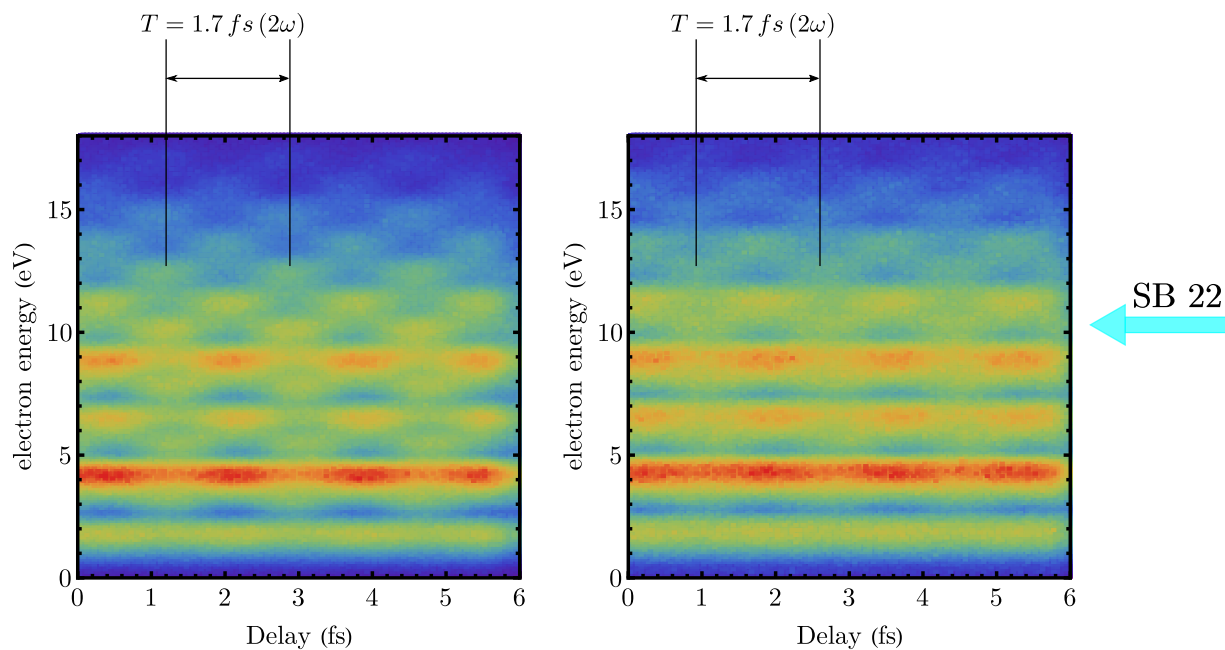


Figure 5.8: Photo-electron energy (coincidence $H_2^+/D_2^+ + e$) vs time delay in the XUV+IR single-ionization of H_2 (right panel) and D_2 (left panel). The sidebands oscillate with a period of $1.7 \text{ fs } (2\omega)$. Sideband 22 is shown as an example.

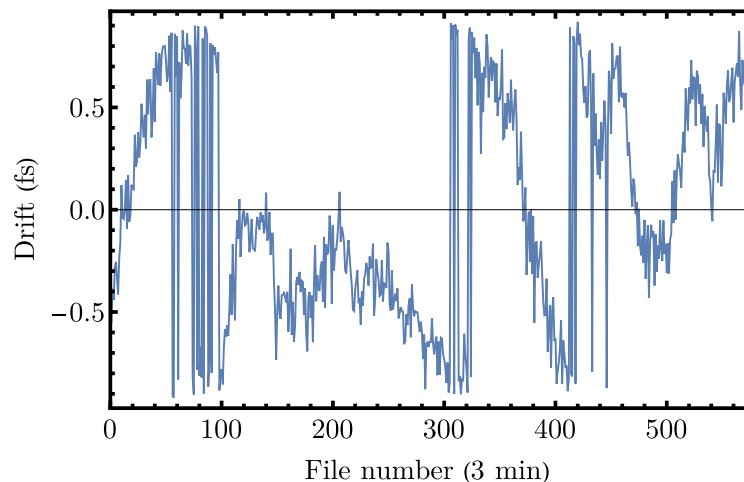


Figure 5.9: The temporal drift (the phase of the sideband 22) of the two arms of the interferometer as a function of the acquisition time. The jumps in the curve are the result of the periodicity of the sidebands ($T = 1.7$ fs).

Drift correction

The interferometer of the Attolab was not actively stabilized during the measurements presented in this work. Therefore, the sideband oscillation in the single-ionization channel shown in Fig. 5.8 is used for long-time drift correction, explained as follows. The data set is divided into smaller sections, e.g., data files of 3 minutes. This is enough to see the sideband oscillations. Then, the phase of a sideband is used as a reference and each following file is shifted so that the phase of that particular sideband stays the same for the rest of the data set. Fig. 5.9 illustrates the phase of sideband 22 (photon energy 22 eV) as a function of acquisition time for a 26-hour measurement corresponding to D_2 . As one can see, after one hour the interferometer has drifted for about 0.5 fs. The jumps in the plots occur when the drift is larger than 1.7 fs (2ω) which is the periodicity of the sideband oscillation.

Atto-chirp

As discussed in section 2.2.1, an XUV pulse is intrinsically chirped. This chirp, known as atto-chirp, is almost linear as a function of photon energy. For each measurement argon is used prior to switching to the other gas targets in order to have a reference for that measurement. Since the atto-chirp of XUV pulse is not of interest in the scope of this work, sideband phases in argon are used to correct for the atto-chirp for the whole measurement. Obviously, this is not an ideal approach, as argon was not measured during the experiment. However, for some measurements a short argon reference was taken before and after a long measurement. By comparing the sideband phases one can observe that these phases

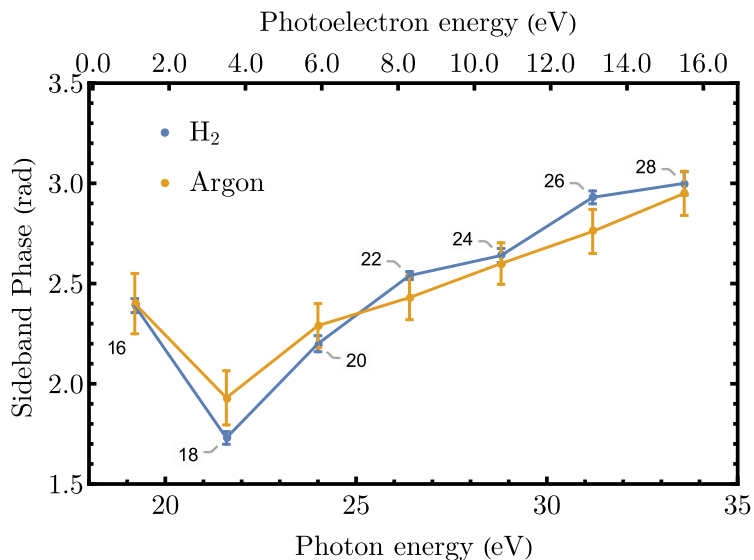


Figure 5.10: Sideband phases in the single-ionization of argon and H_2 with XUV+IR. Number on the curves denote sideband numbers. Argon was measured prior to H_2 , and is used as a reference. The phase of the sidebands show a linear trend except for SB 16.

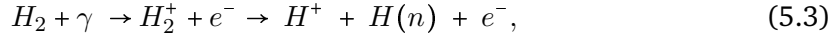
do not change considerably, at least within errorbars. Fig. 5.10 shows the RABBIT phases of different sidebands for argon, performed prior to starting the measurement, and the single-ionization of H_2 for comparison. The argon reference measurement is only couple of minutes resulting in large errorbars.

5.2 Photodissociation of H_2 and D_2

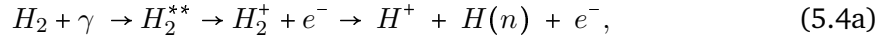
Apart from the dominate photo-ionization which results in bound vibrational levels in the ground state of the molecular ion ($1s\sigma_g$), the interaction with photon energies higher than the dissociation limit of H_2 and D_2 (18.076 [76]) or little less in the presence of and IR field, could result also in $H^+ + H(1s) + e^-$ or $H^+ + H(n=2) + e^-$ with higher photon energies ($h\omega > 28.281$) [122]. The aforementioned phenomena are introduced in this section. Unlike single-ionization, photo-dissociation is possible via different pathways accounting for very rich physical effects.

5.2.1 Photodissociation of H₂ and D₂ with an Attosecond Pulse Train

One XUV photon from the attosecond pulse train with energies higher than the dissociation limit can dissociate the molecule directly



or indirectly



Only the first one (a) is studied in this work. After the dissociation, the surplus energy is shared between fragments

$$E_{H^+} + E_H + E_{e^-} \approx E_\gamma - I_d,^6 \quad (5.5)$$

where I_d is the dissociation limit of H₂. The sum $E_{H^+} + E_H$ is referred to as the kinetic energy release (KER) which is almost $2E_{H^+}$. The time of flight (TOF) spectrum of the interaction between an APT and H₂ is shown in Fig. 5.2. The center of the distribution of H⁺ is marked with a gray vertical line. Two regions on both sides of this line are the protons with energies higher than zero increasing with the distance to the central line flying to the right (away from the ion detector) and vice versa. Subsequently, the KER can be calculated. Fig. 5.11 shows the KER distribution for H₂ and D₂. The width of KER distribution for D₂ is smaller than that of H₂ because of a smaller FC region in the case of D₂⁷. The acquired data is in agreement with experimental data from [124][125]. The D₂ curve is somewhat noisy due to the very short acquisition time.

As one can see from Fig. 5.2, $\frac{H^+}{H_2^+} = 0.02$. This is similar to values reported in previous measurements [126]. This ratio is smaller for D₂ ($\frac{D^+}{D_2^+} = 0.008$). With the help of the ReMi one can detect both H⁺ and e⁻ in coincidence. Once detected, the energy distribution between products of dissociation can be presented in one plot known as the energy sharing plot given in Fig. 5.12. As one can see, most events appear along diagonal lines with a slope of -1. This is the consequence of energy conservation ($E_{e^-} - (E_{XUV} - I_d) = -KER$). Events which are elsewhere do not belong to the coincidence $H^+ + e^-$, and are thus called false coincidences. The diagonal lines are spaced by 2ω , manifesting the odd harmonics of the APT. As an example the 27th harmonic is shown with a diagonal black line. The first diagonal line is the harmonic 17 ($17 \times 1.2 \text{ eV} = 20.4 \text{ eV} > I_d$). At an KER of 0.6 eV, one can see a faint trace (better visible in Fig. 5.17) as a result of an enhanced dissociation due

⁶the exact equality is $E_{H^+} + E_H + E_{e^-} = E_\gamma - I_d - \frac{P_e^2}{2M}$, where P_e is the electron momentum, and M is the mass of nuclei. The last term is very small in energy range used with high harmonic generation in this work, and therefore, this term is always omitted.

⁷Franck-Condon region of D₂ is 16% smaller than that of H₂[123].

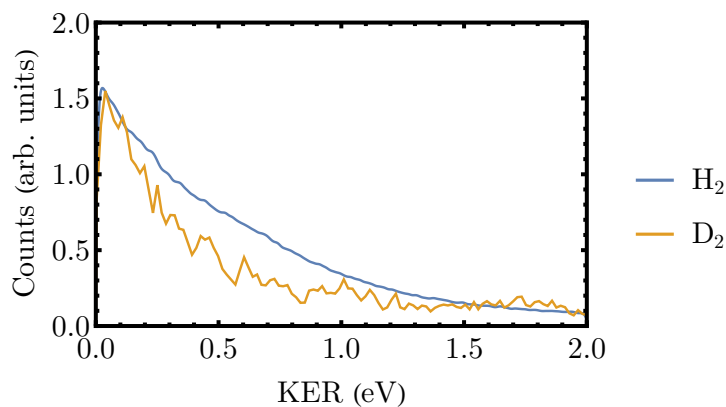


Figure 5.11: Kinetic energy release (KER) for D_2 and H_2 with as a result of the interaction with the APT. D_2 has a narrower KER distribution due to the smaller FC region. Both plots are normalized to emphasize the difference. The D_2 measurement has much fewer data points, and is thus more noisy.

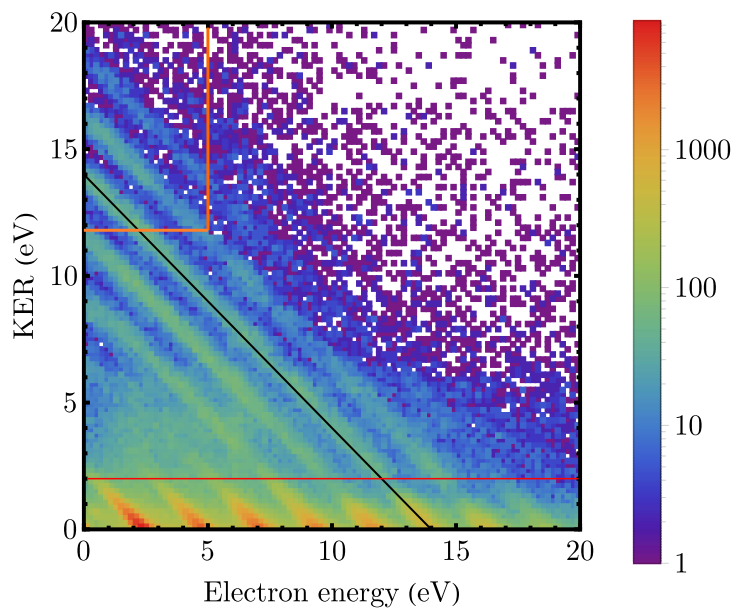


Figure 5.12: Energy sharing between electron and nuclei ((H^+, e) coincidence), integrated over all angles, as a result of the dissociation of H_2 with an attosecond pulse train (APT). Each of the diagonal lines correspond to a harmonic in the APT. For instance, harmonic 27 is marked with a diagonal line with a slope of -1. Events below the red line at $KER=2$ eV are mostly attributed to the GD. The box in the top left corner contains events as a consequence of the direct dissociation via the first excited state of the cation ($2p\sigma_u$).

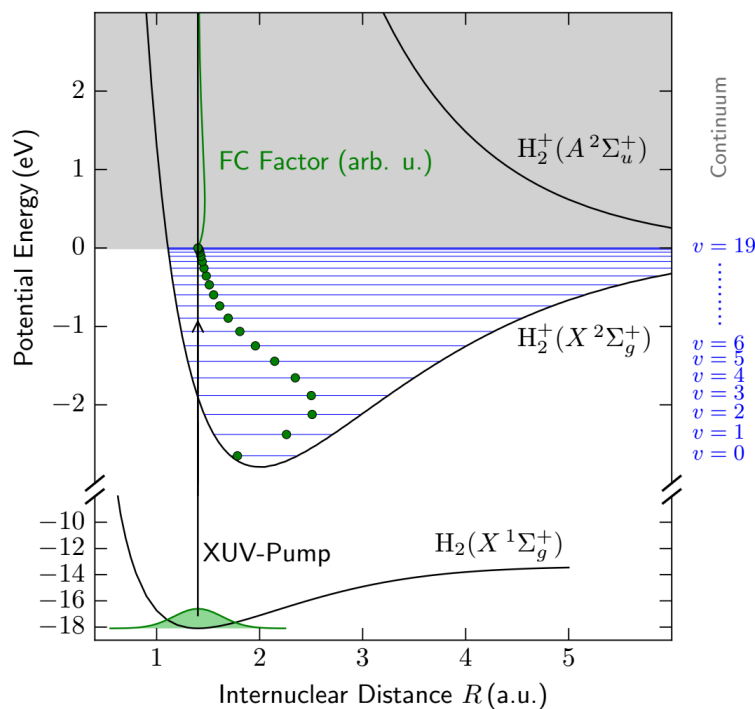


Figure 5.13: Franck-Condon (FC) factors for H₂. The coefficients for the bound ground state of the cation are the same given in Fig. 5.4. The FC distribution in the continuum of the molecular ion (the gray area) is shown with a green curve. Figure taken from [127]

to unwanted IR photons not being completely blocked by the aluminum filter in the XUV arm resulting in bond softening, discussed later in this chapter. The energy sharing plots are very useful means to find out about different dissociative mechanisms contributing to the signal. In the following section, different dissociation mechanisms are explained and attributed to specific regions of this plot in order to gain insight into the rest of the experiments.

5.2.2 Direct Dissociation

The transition from the ground state of the neutral molecule to the ground ($1s\sigma_g$) or the first excited state ($2p\sigma_u$) of the molecular ion, which results in dissociation, is known as *direct dissociation*. The former is also referred to as ground-state dissociation (**GD**).

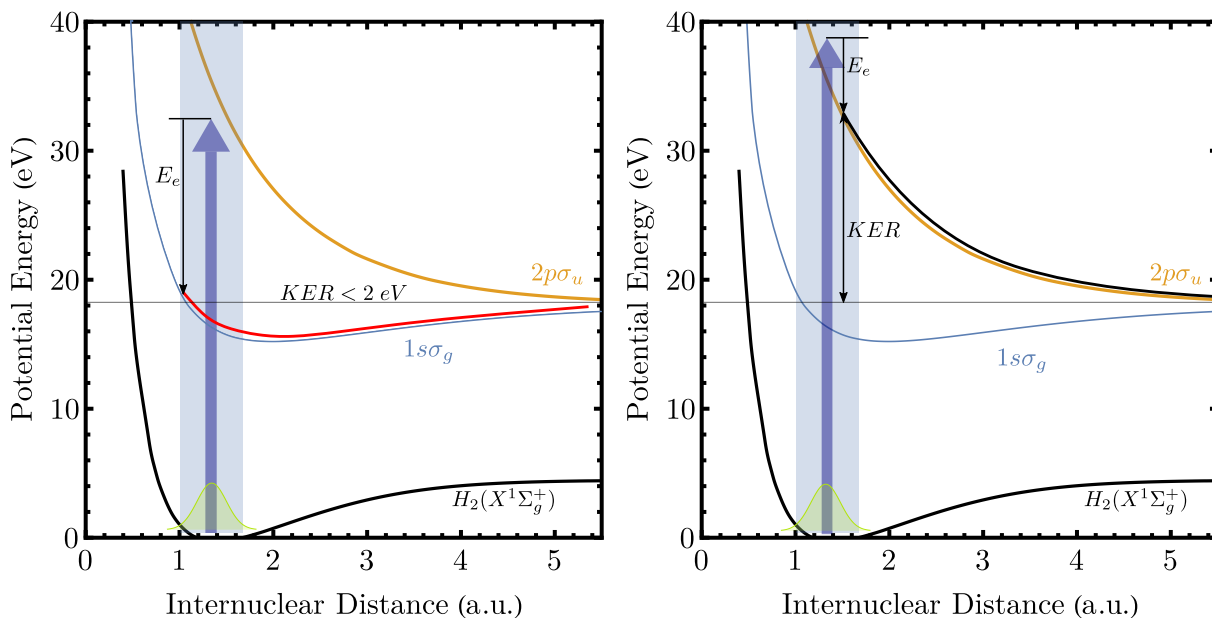
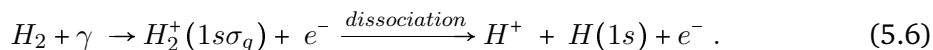


Figure 5.14: Relevant potential energy curves in case of direct dissociation. The FC region is shown with a vertical light blue band. The XUV photon is shown with a vertical blue arrow in the middle of the FC region. Left panel illustrates ground state dissociation using and XUV photon. The nuclear wave-packet follows the red path leaving the dissociating fragments with a KER of less than 2 eV. Right panel shows the direct dissociation using an XUV photon via the first excited state of the cation where the nuclear wave-packet follows the black line resulting in fragments with a high kinetic energy.

Ground-State Dissociation

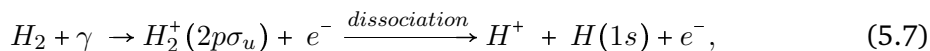
The calculated Franck-Condon factors illustrated in Fig. 5.13 show that a small fraction of states in the continuum [118] of the cation are also populated with photon energies higher than the dissociation limit (18.06 eV) which leads to dissociation of the molecular ion following the $1s\sigma_g$ curve illustrated in the left panel of Fig. 5.14 leaving the fragments with a total KER of < 2 eV according to the following equation



This region contributes to events below the red line in Fig. 5.12. As one can see, GD has the largest contribution to molecular dissociation with a very low kinetic energy. GD decreases exponentially with KER as one can better see in Fig. 5.11.

Dissociation via $2p\sigma_u$

With photon energies higher than 30 eV, as shown in the right panel of Fig. 5.14, the first excited state of the cation ($2p\sigma_u$) can be populated. Being in a dissociative state, the molecule breaks apart into fragments according to



and, as a consequence, relatively large KERs (> 12 eV) and small electron energies ($E_e = \hbar\omega - I_D - KER$) are obtained contributing to events within the orange box in Fig. 5.12. Note that in the case of direct photo-dissociation, symmetry properties do not impose orientation of the molecule with respect to the molecular axis, unlike resonant dissociations.

5.2.3 Indirect Dissociation

Indirect, also known as resonant, dissociation takes place when the molecule is first excited to a 'superexcited' state (doubly-excited state) which can autoionize through electron correlation even if the nuclei are fixed [128]. Once in the doubly-excited states, molecular autoionization competes with dissociation into neutrals (Eq. 5.4b).

Doubly-excited states are classified according to the series limits. Q_1 states correspond to the first excited state of the molecular ion $^2\Sigma_u^+(2p\sigma_u)$ and Q_2 states to the second excited state $^2\Pi_u(2p\pi_u)$. Q_1 states have a $(2p\sigma_u)(nl\lambda)$ configuration resulting in $H(1s) + H(n'l')$, whereas Q_2 states with $(2p\pi_u)(nl\lambda)$ configuration result in $H(2l'') + H(n'l')$ at infinite nuclear distances. All doubly-excited states are dissociative leading to the fragmentation of the molecules into either neutral fragments or ions. The relevant channel to this work is the dissociation into a neutral fragment (H/D) and an ion H^+/D^+ . This takes place only if the autoionization lifetime of the doubly excited state is smaller than the time it takes for the molecule to dissociate otherwise the dissociation ends in two neutral fragments (Eq. 5.4b).

As the ground state of H₂ and D₂ exhibits Σ symmetry, dipole allowed transitions are $\Sigma \rightarrow \Sigma$ for molecules parallel to the polarization axis, and $\Sigma \rightarrow \Pi$ for molecules perpendicular according to table 3.4. In other words, the dipole transition matrix element depends on the direction of the electric field with respect to the molecular axis, and additionally, on the symmetries of the initial and final states as in the case of doubly excited states. Note that molecules are randomly oriented in the gas target at the time of interaction with the linearly polarized laser pulse. After the detection of fragments, one can profit from the full 4π detection capacity of the ReMi, to calculate angles of emitted fragments in all directions. One can put conditions on angles in post analysis, and thus select a particular transition, e.g., perpendicular or parallel. Fig. 5.15 illustrates a perpendicular transition with fragments within the yellow region and a parallel one in the blue region. According to the detection geometry, the polarization axis is along the z direction. Throughout this

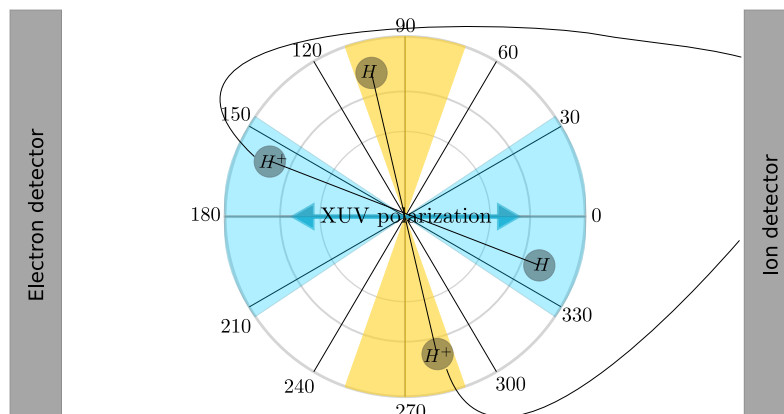
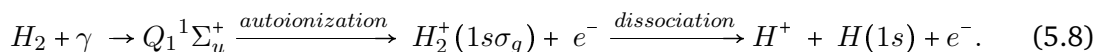


Figure 5.15: Example of a perpendicular (emission within the yellow cone) and parallel (emission within the light blue cone) transition. The z axis is along the polarization. Parallel orientation is a cone with an opening angle of $\pm 35^\circ$ in both directions if not otherwise stated. Perpendicular orientation is a cone with an opening angle of $\pm 20^\circ$ in both directions if not otherwise stated.

work, a parallel transition is defined as the emission of the proton in a cone with an opening angle of $\pm 35^\circ$, and a perpendicular transition is defined as an emission in a cone with an opening angle of $\pm 15^\circ$, if not otherwise stated.

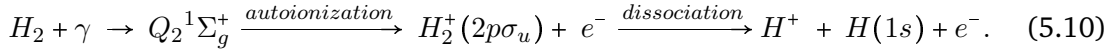
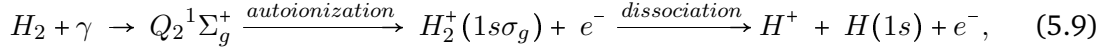
Parallel Transitions

As discussed earlier, only final states of the doubly-excited states (DESS) of H_2 and D_2 with Σ symmetry are populated in parallel transitions, as illustrated in the left panel of Fig. 5.16, which can consequently autoionize into the ground state of the molecular ion according to



For photon energies higher of 25-40 eV mostly the lowest curve of $Q_1^1 \Sigma_u^+$ series contributes to autoionization [129]. Dissociation occurs at intermediate nuclear distances (4-5 a.u.) before the potential crossing point [130] with KERs 0-22 eV [124][42][131][132], and electron energies 0-25 eV which corresponds to the region between the two red lines in the left panel of Fig. 5.17.

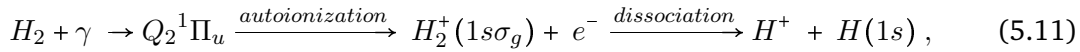
The autoionization lifetime of the lowest curve of $Q_1^1 \Sigma_u^+$ ($Q_1^1 \Sigma_u^+$ is 0.4 to 1 fs [133][134] (see appendix F for the bandwidth of the relevant DESS), similar to that of $Q_1^1 \Sigma_g^+$, and can be populated using two photons (XUV+IR). The autoionization lifetime of higher Q_1 series is much higher and, as a result, only the effects of the lowest ones are considered. With photon energies higher than 31 eV, two of the lowest Q_2 series can also be populated in parallel transition:



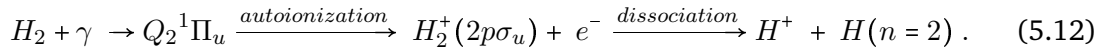
The autoionization time of the above states is, however higher ($> 2fs$) than that of Q_1 and, as a consequence they do not contribute the detected events. The energy sharing between proton and electron is same as other Q_2 series, as explained in the section that follows.

Perpendicular Transitions

For photon energies between 31-37 eV, a transition from the ground state of the neutral molecule ($X^1\Sigma_g^+$) to doubly-excited states $Q_2^1\Pi_u$ becomes possible for molecules perpendicular to the polarization axis of the laser beam. Once populated, this state can autoionize to either the ground state $1s\sigma_g$ and dissociate



or to the first excited state of the cation $2p\sigma_u$



These two pathways are shown in the right panel of Fig. 5.16 with red and violet pathways, respectively. The former case reaches the maximum KER if autoionization takes place at infinitely large nuclear distances, whereas the latter at the smallest possible nuclear distances. Zero KERs can be reached only via $1s\sigma_g$. Q_2 DESs autoionize preferentially to $2p\sigma_u$ at a fixed nuclear distance rather to $1s\sigma_g$ [124].

The right panel in Fig. 5.17 shows the energy sharing which corresponds to molecules dissociating perpendicular to the laser polarization. With the help of the potential curves in the right panel of Fig. 5.16, one can explain different regions in the plot. The checkered area is the region where the acceptance of the ReMi did not detect charged ions with higher kinetic energies due to the low extraction voltage. The diagonal features for KERs higher than 2 eV are assigned to dissociation by means of Q_2 doubly-excited state of the neutral molecule via $1s\sigma_g$ (shown with the red box). The lower part of the plot is related to ground state dissociation because this transition is isotropic, and therefore insensitive to angle selection. The region could have KERs up to 2 eV, as discussed previously.

Another transition is also allowed according to table 3.4 from ground state of the neutral molecule to $Q_1(^1\Pi_u)$. In all previously done measurements, no resonance effects

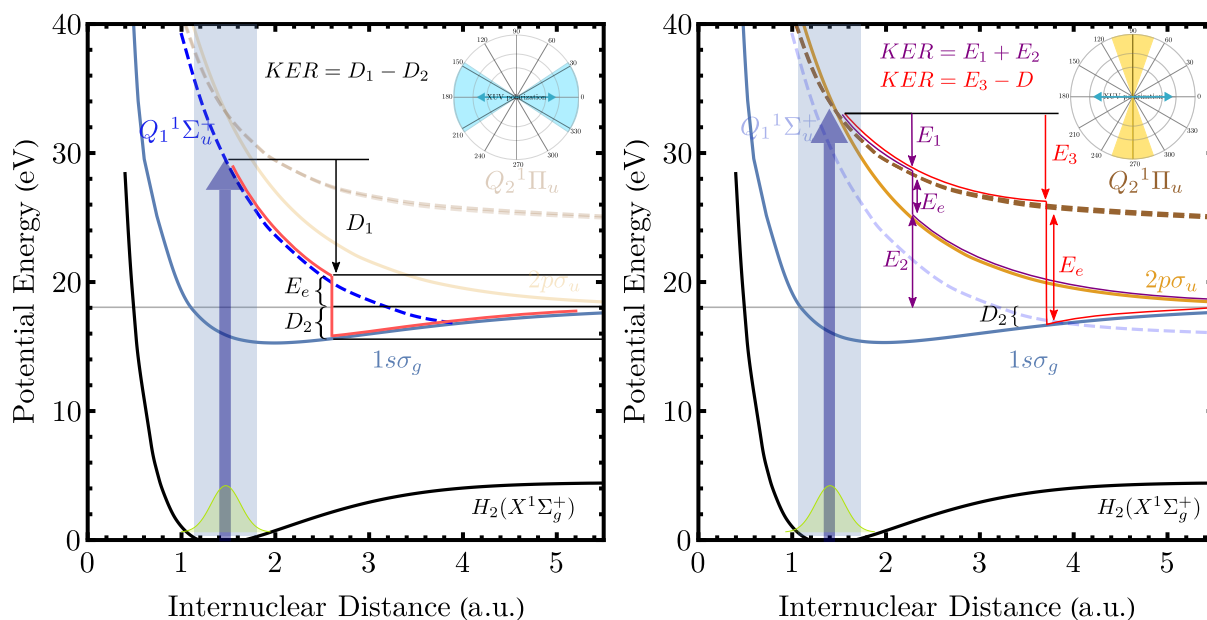


Figure 5.16: Relevant potential energy curves in case of indirect (resonant) dissociation. The FC region is shown with a vertical light blue band. The XVU photon is shown with a vertical blue arrow in the middle of the FC region. Left panel: for photon energies between 25-40 eV the lowest state of the $Q_1^1\Sigma_u^+$ series can be populated for molecules parallel to the polarization axis. This state is dissociative and, as a result, the molecule dissociates following the red path with KERs of 0-22 eV. Right panel: for photon energies between 31-37 eV, the lowest-lying state of the $Q_2^1\Pi_u$ can be populated for molecules perpendicular to the polarization axis. This state has a repulsive potential and can dissociate either via $1s\sigma_g$ (red path) or via $2p\sigma_u$ (violet path).

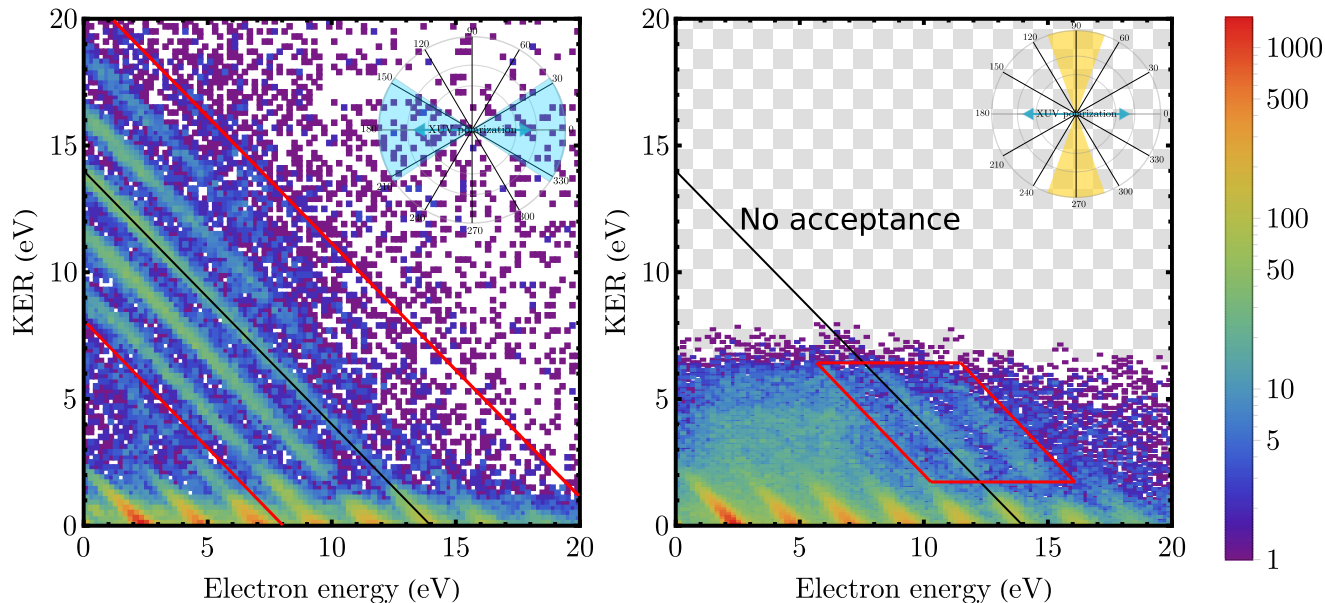


Figure 5.17: Left panel: The energy sharing plot for parallel transitions as a result of photo-dissociation of H₂ with an APT. The lower region, corresponding to a KER from 0 to 2 eV, is mostly related to ground-state dissociation. Harmonic 27 is marked with a diagonal line with a slope of -1. The region between the two red lines contains indirect dissociation from $Q_1^1\Sigma_u^+$. Right panel: the energy sharing plot for perpendicular transitions in photo-dissociation of H₂ using an APT. The lower region, corresponding to a KER from 0 to 2 eV, is mostly related to ground-state dissociation. Due to the acceptance of the ReMi, high energetic protons flying perpendicular to the detector axis can not be captured with the use of the electric field and, as a result, they do not hit the detector. Harmonic 27 is marked with a diagonal line with a slope of -1. The region within the red box corresponds to indirect dissociation according to Eq. 5.2.3.

are to be seen because the autoionization lifetime of this state is larger than dissociation timespan[42] [133].

It is important to bear in mind that, the features in the KER distribution can not necessarily be attributed to pathways mentioned earlier. In fact, resonance interference effects where two channels overlap results in an modified distribution, as shown in Fig. 5.18. In a region where two channels with different symmetries contribute to KER, an asymmetry arises in the photo-electron distribution in the molecular frame [125][130][135][19]. In table 5.1, the summary of the contributing dissociative pathways to events observed in energy sharing plots is given. Note that energy ranges are not exact since they are the intersection of different curves with the FC region, which does not have sharp boundaries. They are also slightly different for D_2 and H_2 . Energy limits is in principle narrower for D_2 . For a more precise comparison between H_2 and D_2 see [123].

Table 5.1: Summary of different dissociation pathways.

Dissociation Ch.	Photon Energy (eV)	KER (eV)	Electron Energy (eV)	Orientation
Ground State Dissociation	>18.076	0-2	>0	Isotropic
Dissociation via $2p\sigma_u$	31-43	12-25	0-13	Isotropic
Indirect via $Q_1^1\Sigma_u^+$	25-40	0-22	0-20	Parallel
Indirect via $Q_2^1\Pi_u$	> 31	2-9(via $1s\sigma_g$) 7-15(via $2\sigma_u$)	8-16(via $1s\sigma_g$) 0-3(via $2p\sigma_u$)	Perpendicular

5.2.4 The Role of IR Probe

The interaction between H_2 and D_2 with an APT (XUV) in the presence of a weak dressing field gives rise to two phenomena: firstly, the appearance of sidebands, as shown in Fig. 5.20. As one can see, sidebands (SBs) as extra lines between harmonic lines have appeared. For example, SB 26 is marked with a dashed red line next to harmonic 25 marked by a solid black line. The region marked by a blue arrow has been caused due to bond softening, as explained in the following. Secondly, an enhancement of photo-dissociation known as bond softening (BS) in the Floquet picture. Once ionized, the NWP in the bound potential of the cation ($1s\sigma_g$) propagates towards higher nuclear distances. The IR beam causes bond-softening after the NWP reaches the outer turning point after around 10 fs in H_2 [136][137]. The BS effect manifests itself as two peaks on two sides of the central dissociation peak, as shown in Fig. 5.19. As the intensity of the probe field increases, these two peaks grow larger relative to the central one (GD).

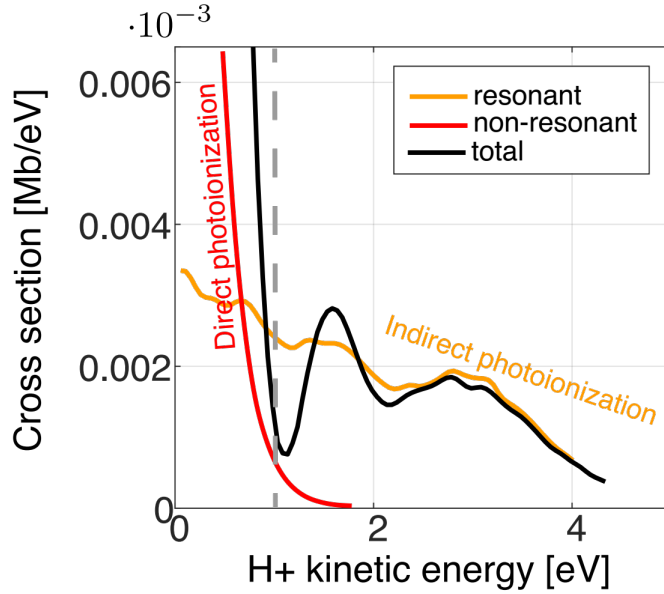


Figure 5.18: Cross section of photo-dissociation in the case of H₂ at a photon energy of 26 eV. Figure taken from [42].

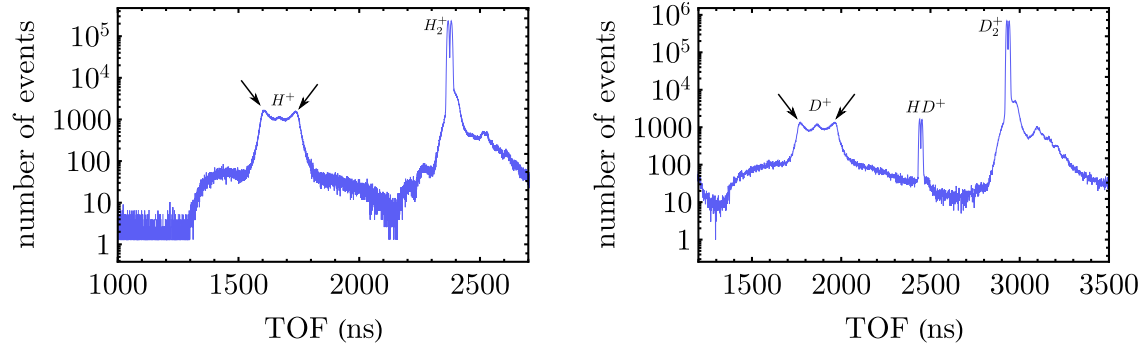


Figure 5.19: Time-of-Flight spectrum of H₂ (left panel) and D₂ (right panel) using XUV+IR. The central peak is the ground state dissociation and two neighboring peaks (shown with arrows) are bond-softening due to the absorption of an IR photon. The shoulders are higher energetic protons. The peak in the middle of the left panel is the single-ionization of HD is due to the contamination of D₂ with HD.

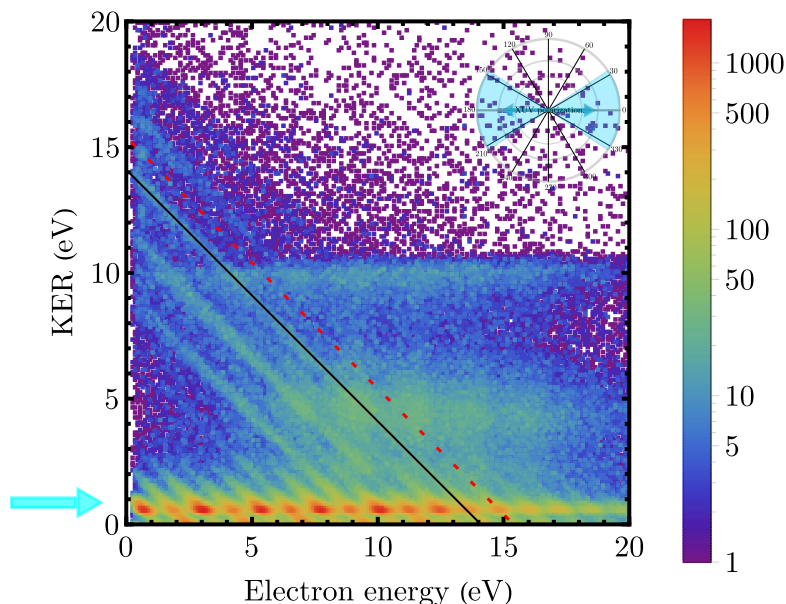


Figure 5.20: Energy sharing plot of the photodissociation of H_2 (coincidence $H^+ + e$) as a result of the interaction with XUV+IR for the parallel orientation. Harmonic 25 and sideband 26 are marked with a solid black and dashed red lines, respectively. The blue arrow marks the position of the bond softening region. The events that are not on diagonal lines are false coincidences.

Intensity Dependence

The dissociation rate through bond softening can be well described by Fermi's golden rule for vanishing intensities. For higher intensities, however dissociation rate is no longer linear as a function of intensity due to the nonlinear nature of the light-induced avoided crossings [21]. Fig. 5.21 illustrates KER distribution for different intensities where the contribution of bond-softening increases with higher intensities. Another feature is the shape of the distribution which also varies. For higher intensities the width of the bond-softening region increases. This increase is, however, not symmetric around the maximum and the distribution becomes larger on the lower side of the bond softening region in the KER distribution, which is attributed to the suppression of the potential at the one-photon avoided crossing as one can see in Fig. 5.23. As a consequence, the contribution of lower laying vibrational levels becomes larger. As for measurements done during this work, a rough estimate of the applied probe light intensity can be achieved by measuring the ponderomotive shift in the photo-electron spectrum ionized by XUV with and without IR dressing field. Considering the fact that the ponderomotive shift at the intensity of $1 \times 10^{12} W/cm^2$ is 100 meV at 1030 nm wavelength and could be well resolved with the resolution of the ReMi, no shift in the photo-electron spectrum suggests that the intensities are on the lower side of $10^{11} - 10^{12} W/cm^2$ intensity range.

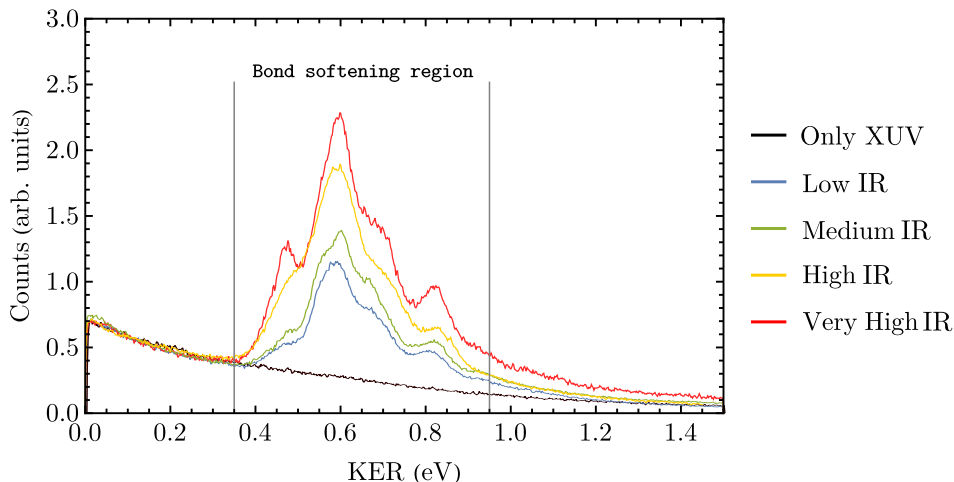


Figure 5.21: KER distribution at different intensities in the photo-dissociation of H₂ using XUV+IR for all dissociation angles and electron energies. The difference between the black curve (only XUV) and other curves in the region between 0.4 and 0.9 eV is due to bond-softening. All curves are normalized with respect to zero energy protons in order to emphasize the differences in the bond softening region.

5.3 Vibrationally-resolved dissociation of H₂ and D₂ using XUV+IR

An anharmonic oscillator model is used to describe the energy of vibrational levels according to

$$E(\nu) = \omega_e \left(\nu + \frac{1}{2} \right) - \omega_e \chi_e \left(\nu + \frac{1}{2} \right)^2, \quad (5.13)$$

with $\nu = 0, 1, 2, 3, \dots$ being the vibrational state number, ω_e being the fundamental, and $\omega_e \chi_e$ the anharmonic constant. The vibrational levels of H₂ and D₂ are shown in Fig. 5.22 (values are given in appendix B). The position of the one- and three-photon avoided crossings are marked with horizontal lines.

Traditionally, vibrationally-resolved dissociation in the laser field was done using an H₂⁺ [138] or D₂⁺ [101] ion beam. During this work, however, the ionic state is reached via ionization with an XUV pulse which prepares a coherent superposition in the bound state of the cation. As discussed previously, the bandwidth of the XUV spectrum is larger than the vibrational spacing in the molecular hydrogen ion and, as a result, one can not resolve the vibrational peaks in the photo-electron spectrum resulting from single-ionization of H₂. However, using a long probe pulse with a duration of 50 fs ($\Delta\nu = 30$ nm), one can dissociate the molecular in the first excite state ($1s\sigma_g$) to the dissociative $2p\sigma_u$ which ultimately dissociates (bond softening). Two important conditions must be fulfilled in order to observe the vibrational states in the KER distribution. Firstly, the molecular ion

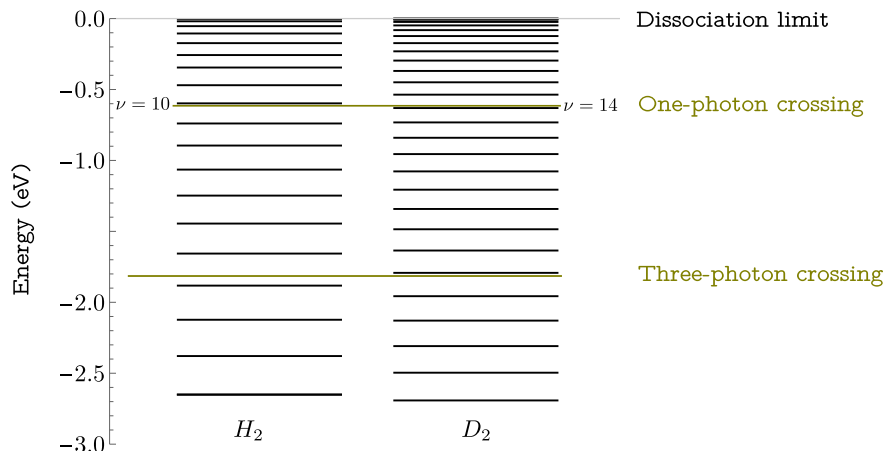


Figure 5.22: Vibrational levels of the ground state of the cation for D_2 and H_2 . The dissociation limit is at zero energy. One- and three-photon crossings are shown with horizontal lines.

nuclear wave-packet needs enough time after creation to propagate in the bound potential before dissociation. The oscillation period of vibrational state ν is given by

$$T(\nu) = \frac{h}{E_{\nu+1/2} - E_{\nu-1/2}}, \quad (5.14)$$

which results in a oscillation period of 30 fs for the 10th vibrational state of H_2 and 41 fs for 14th vibrational state of D_2 . This suggests that, vibrational levels in D_2 are not always visible with pulse durations available. This point is discussed in more depth later. Secondly, the probe pulse duration must be long enough to resolve the energy spacing between vibrational levels. The KER after dissociation is given by

$$KER = \hbar\omega - E_\nu, \quad (5.15)$$

where E_ν is the energy of the vibrational level ν . According to Fig. 5.22, one can correspond the biggest peak in the bond softening region in the KER distribution plot to vibrational state $\nu = 10$ for H_2 and $\nu = 14$ for D_2 as the one-photon crossing hits almost those energy levels. However, as the intensity increases, neighboring states can also contribute to the dissociation. Fig. 5.23 illustrates the case of H_2 . Only the effect of one-photon crossing needs to be considered in the laser intensities used in this work ($I < 10^{12} W/cm^2$). Fig. 5.24 shows KER distributions for both H_2 and D_2 for molecules dissociating parallel with respect to the laser polarization axis. The angle integration is $\pm 15^\circ$ so as to better resolve the peaks in the KER distribution. The vibrational levels are also included and attributed to the corresponding peaks. The width of the peaks is a function of various parameters. The laser spectral width, the lifetime of the vibrational state, and broadening due to the rotational states.

- **Spectral bandwidth of the laser.** The bandwidth of the probe pulse has a contribution to the broadening of the peaks in the KER distribution. Using $\Delta E = \frac{1}{2}hc\frac{\Delta\nu}{\lambda^2}$, one obtains 18 meV for a pulse duration of 50 fs with a central wavelength of 1030 nm.
- **Vibrational state lifetime.** The lifetime of the vibrational state is another contributing factor as these states spend a finite time in the binding potential. The linewidth is then given by the Heisenberg uncertainty relation ($\Delta E \times \tau \geq \hbar/2$). Lifetime of the vibrational states can be estimated using the period of the oscillation⁸ given in Eq. 5.3. The linewidth of the 10th vibrational state of H₂ is 20 meV, whereas D₂ has a linewidth of 16 meV for its 14th vibrational level.
- **Rotational state distribution.** Another source of line broadening is the distribution of the rotational states. The energy of the first three rotational levels of H₂ are 7.4, 14.8, and 44.4 meV and those of D₂ are 3.7, 7.4, and 22.2 meV (for more details see Appx. B. At room temperature ($k_B T = 25$ meV) the first two and three rotational levels of H₂ and D₂ can be populated, respectively. After the photo-ionization from the ground level of the molecule, the rotational levels $J = 0, 1, 2, 3$ of each vibrational level can be populated because of the selection rule $J = 0, \pm 1$. One expects a maximum broadening of 22.2 meV in both H₂ and D₂ as a result of rotational degrees of freedom.

The overall broadening is, therefore, 35 meV for H₂ and 33 meV for D₂. This is still smaller than the spacing between vibrational levels of D₂. As a result, the fact that the vibrational levels can not be resolved in the case of D₂ (Fig. 5.24 left panel), could be attributed to the pulse duration which is not long enough for the NWP to spread, whereas for H₂ due to its faster vibrations, the vibrational levels can be observed.

Other features present in all measurements are the peaks at higher KERs which do not match the vibrational levels. As for D₂, the higher two peaks at 0.83 eV and 0.95 eV, and for H₂ the peak at 1.0 eV. These peaks can not be attributed to level shifting as this effect occurs for vibrational levels below the avoided crossing [138][101]. Another possible effect observed already is the effect of the chirp of the probe field [139][140]. This is, however, very unlikely, because the chirp used in those experiments is much larger ($GDD \approx 1000 \text{ fs}^2$) than that of the probe beam for this experiment. Another possible explanation could be the net two photon transition. This process is very unlikely with these low probe intensities ($I < 10^{12} \text{ W/cm}^2$).

Intensity dependence

As the intensity of the probe field is increased, the opening of the avoided crossing becomes wider and, as a result, more of the lower lying vibrational levels can now dissociate

⁸The Rabi frequency at these low intensities is much higher than the oscillation frequency of the vibrational states, and thus, their contribution is small

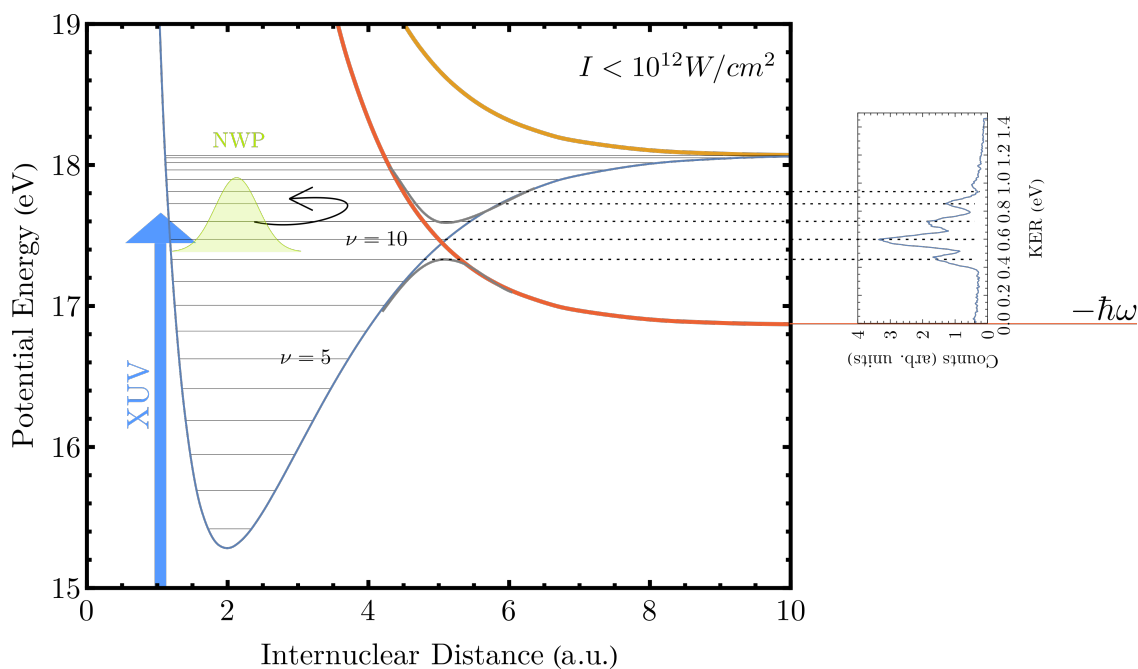


Figure 5.23: Diabatic and adiabatic potential curves in the presence of a dressing field showing the bond softening mechanism. On the right, the KER distribution for molecules parallel ($\pm 15^\circ$) with respect to the polarization axis is given where the peaks corresponding to vibrational levels are marked with dashed lines.

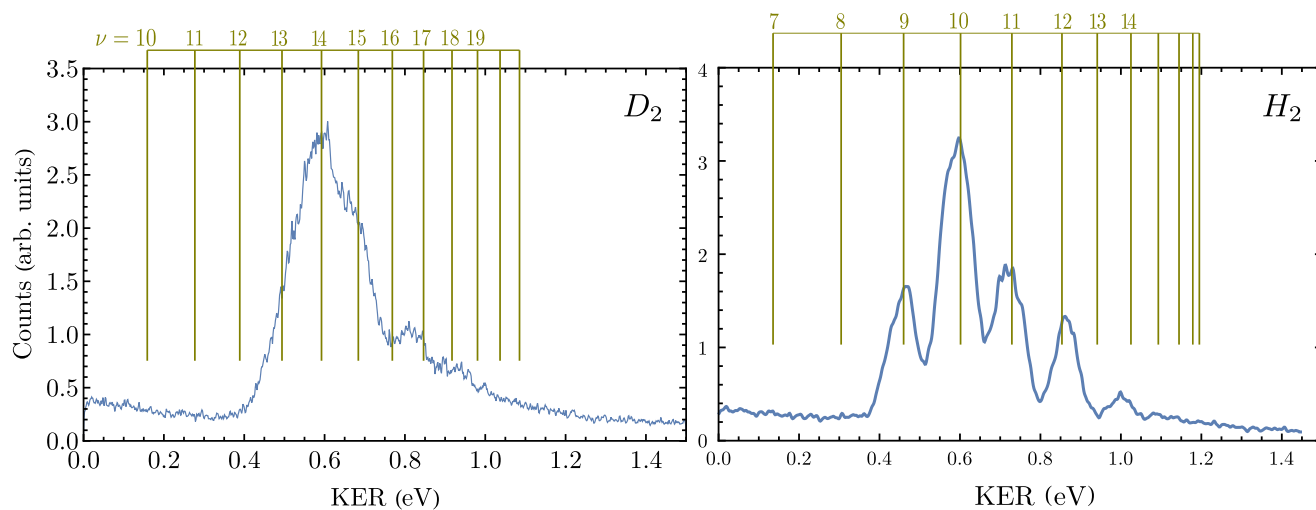


Figure 5.24: KER distribution of D_2 (left panel) and H_2 (right panel) for parallel direction ($\pm 15^\circ$) in an interaction with XUV+IR and their corresponding vibrational levels are shown.

or tunnel through the field distorted barrier, as shown in Fig. 5.23. Vibrational level $\nu = 9$ in case of H₂ grows faster than other peaks by increasing the intensity. The contribution of $\nu = 8$ could not be detected even for the measurement done with the highest intensity. In case of D₂ the same happens to $\nu = 12, 13$. Due to the dipole coupling resulting in BS the effective intensity felt by the molecule is given by projecting the polarization axis onto the molecular one

$$I^{eff}(\theta) = I \cos^2\theta, \quad (5.16)$$

where θ is the angle between molecule and laser polarization suggesting that changing the angle is the same as changing the probe intensity.

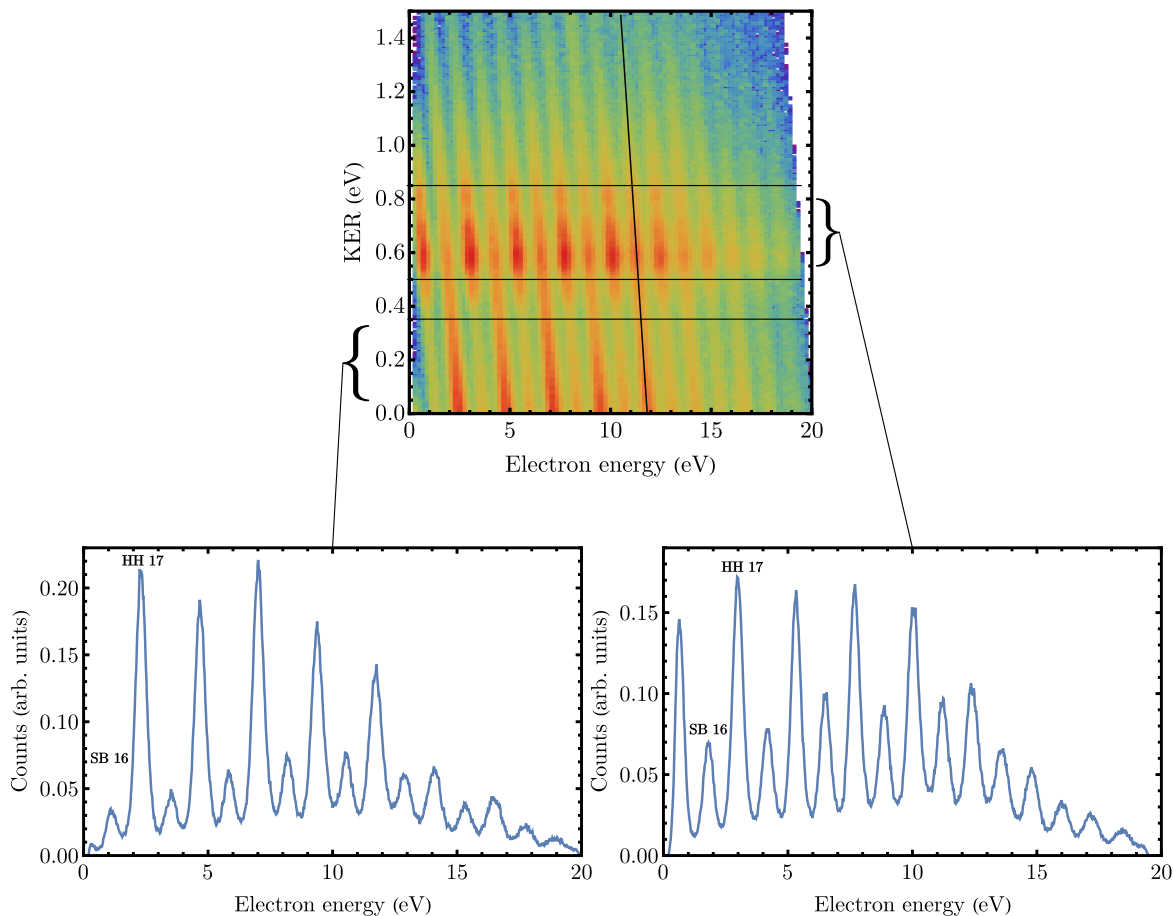
5.4 RABBIT in H_2 and D_2 

Figure 5.25: Upper panel: Energy sharing between electron and nuclei integrated over all molecular orientations and all delay values in H_2 . The diagonal line marks a conservation line corresponding to harmonic 25 with a photon energy of 30 eV. Lower left panel: The projection of the select KER region, corresponding to the ground-state dissociation (KER:0-0.38 eV), onto the electron energy axis. Lower right panel: The projection of the select KER region, corresponding to the bond softening region (KER:0.5-0.85 eV), onto the electron energy axis. Sideband 16 and harmonic 17 are marked in both panels.

The RABBIT technique, introduced in section 2.2.1, can be applied also to molecules to investigate the phase of the outgoing photo-electron wave packet. This technique has proved to be a robust tool to investigate photo-ionization time delays in atomic systems [26][62] see [141] for a review. Due to its complexities in molecules compared to atoms, very few experiments are available using this technique. As an example, the phase of the photo-electron in the presence of continuum resonances in molecular nitrogen was investigated using this technique [68]. As well as that, relative photo-ionization time

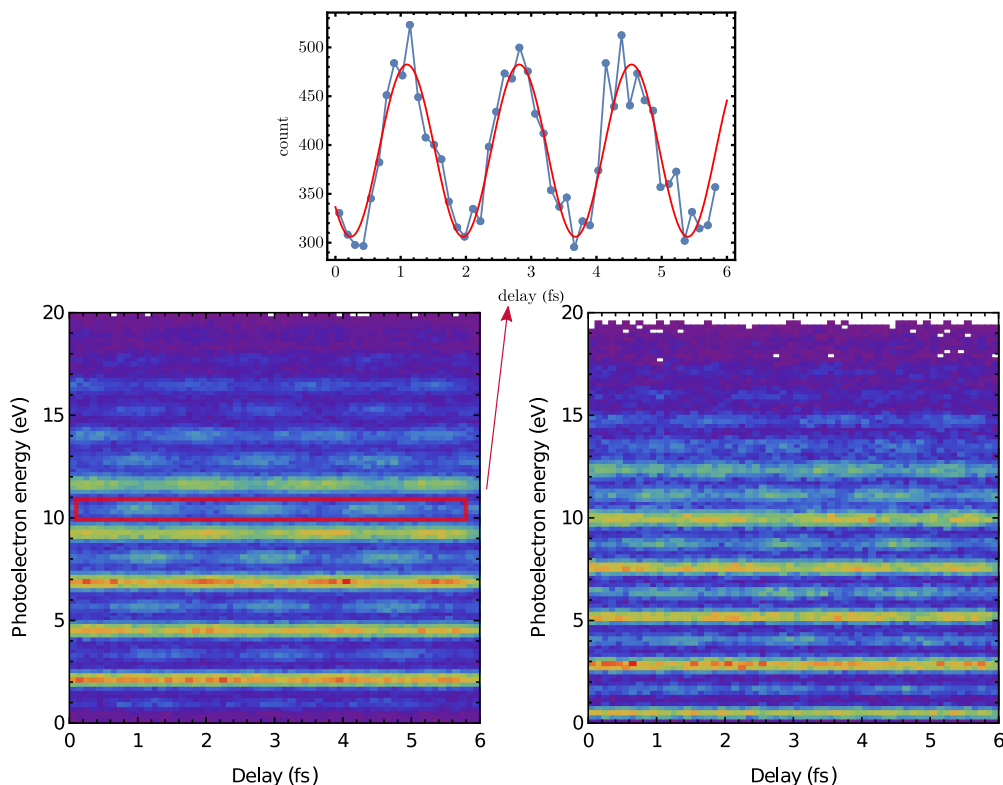


Figure 5.26: Lower left panel: the RABBIT traces for a KER region corresponding to the ground-state dissociation (KER:0-0.38 eV) integrated for all molecule orientations. Lower right panel: the RABBIT traces for the bound-softening region corresponding to the KER interval 0.5-0.85 eV. The projection of the SB 24 onto the delay axis is given in the upper panel. A sinusoidal function is fitted to the experimental data.

delays between two outermost valance shells under the influence of shape resonances in H_2O , N_2O [30], N_2 [31], and CO_2 [32] has been studied. The application of RABBIT to study dissociative photo-ionization is very rare and limited only to CO [33], and H_2 [34] so far. The difficulty arises due to the very low dissociative cross section resulting in a very long acquisition time. This poses a challenge in order to reach attosecond time resolutions. To apply the RABBIT technique to photo-dissociation, one has to detect ions and electrons in coincidence which reduces the yield even further. As regards D_2 , the photo-dissociation cross section is almost three times less than that of H_2 .

As discussed previously, the photon energy is shared between electrons and nuclei due to the fact that the distance between atoms constituting the nuclei is not fixed resulting in diagonal structures in the energy sharing plots. By choosing small regions of KER one can plot same RABBIT traces similar to atoms. By doing so, one can attribute these RABBIT traces to different dissociation mechanisms, introduced in section 5.2.1. However due to the extremely small contribution of mechanisms with a KER higher than 1 eV to the overall

number of events, the discussion is only limited to the region from 0-1 eV in the KER distribution. Even within this small region, there are many different pathways interfering with each other. Within this range there are two main mechanisms contributing to the events: ground state dissociation **GD** and bond softening **BS**, as shown in Fig. 5.25. The projection of these regions onto the electron energy is given in the lower panels. The first peak in the photoelectron spectrum corresponding to GD starts with SB 16, whereas in the right panel the first peak is harmonic 15. The origin of this difference is explained in the section that follows. One obtains the RABBIT traces by plotting the above two spectra as a function of the delay between XUV and IR beam. The resulted plots are shown in Fig. 5.26. The RABBIT traces corresponding to BS is shown in the left panel and that of GD in the right one. Once RABBIT traces are produced, one can retrieve the phase of different sidebands. An example is shown in the upper panel which shows the projection of the marked region onto the delay axis. A function of the form $I = A \cos(\omega t - \phi) + B$ is fitted to the experimental data, and the phase ϕ is extracted. More details about the fit procedure and error bars, can be found in appendix D.

5.4.1 Ground State Dissociation vs Bond Softening

As one can see in Fig. 5.25, the photoelectron spectra of GD and BS are different in that these cases have different electron energies which can be explained using the energy conservation $E_e = \hbar\omega - I_D - KER$, as illustrated in Fig. 5.27. In the case of ground state dissociation, almost no energy is absorbed in the molecule, apart from the small integration window of KER. Harmonic 15 with an energy of 18 eV can not dissociate the molecule, and therefore, the first peak in the GD photoelectron spectrum (Fig. 5.25 right panel) corresponds to sideband 16. This happens when harmonic 15 absorbs and harmonic 17 emits a photon reaching the energy $(16 \times 1.2) - I_D - KER_{window} = 0.65$ eV, where KER_{window} is the selected KER region. As for bond softening, on the other hand, the energy of an IR photon (1.2 eV) is absorbed by the molecule (KER) according to Eq. 5.3, i.e., one can shift the whole potential curve by almost half a photon energy⁹, and, as a consequence, harmonic 15 is the first peak in BS electron spectrum. It should be noted that, in a sideband in BS three photons are absorbed in total, two (XUV+IR) in the first step and the third (IR) photon by the molecule. For example, in the energy sharing plot harmonic 25 at 11.9 eV in GS region turns in to sideband 24 along the diagonal line within BS region.

The sideband phases for GD and BS regions for both H_2 and D_2 are given in Fig. 5.28. The phases are integrated over all orientations of the molecule. The attochirp is removed using the argon reference for each measurement. There are some similarities in phases between GD and BS as well as H_2 and D_2 . For example, sideband 16 shows as shift in phase between GD and BS in D_2 , whereas in H_2 the two cases are almost similar. Phases of sidebands 18 and 20 show similar values for GD and BS in H_2 and D_2 . This could be due to the fact that in this energy range there are not any resonant states according to the

⁹KER gains 0.6 eV ($\hbar\omega/2$).

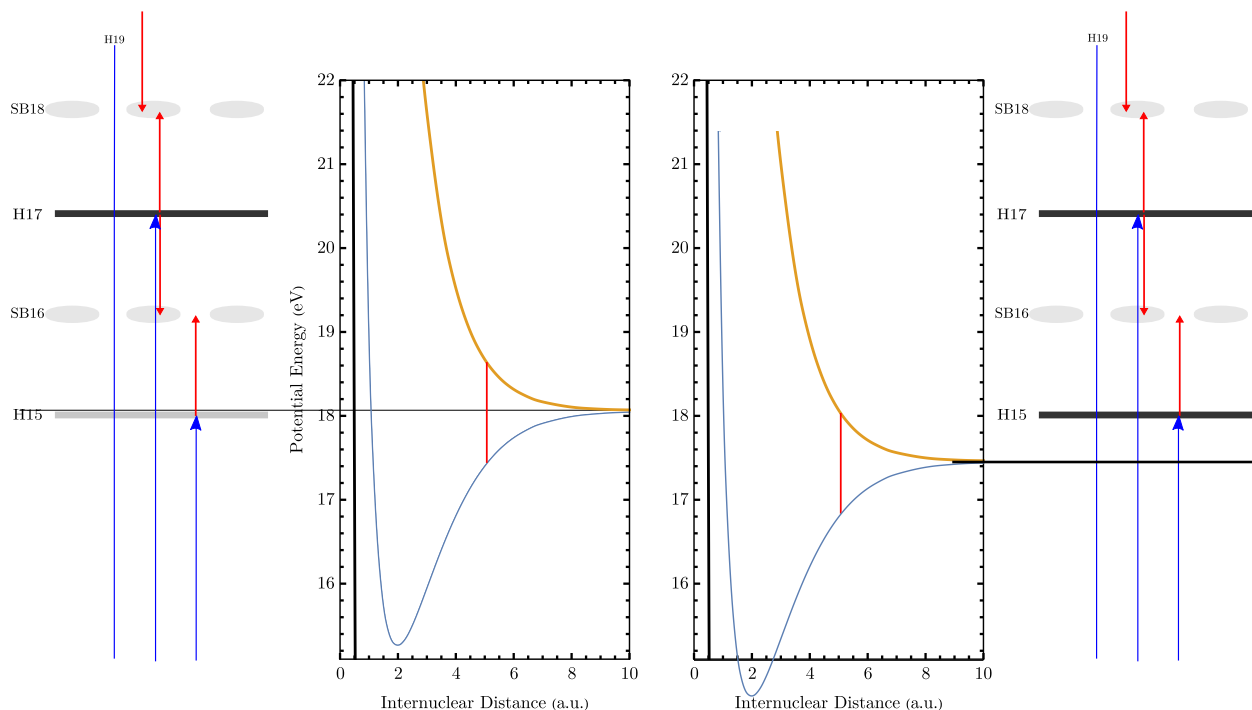


Figure 5.27: Relevant potential curves of H_2 . Left panel: the schematic representation of the RABBIT traces resulting from the ground state dissociation of H_2 . Harmonic 15 can not dissociate the molecule and, as a result, the first peak in the photoelectron spectrum is sideband 16. Right panel: the schematic representation of the RABBIT traces resulting from bond softening. The molecule in this region absorbs a photon and gain almost 0.6 eV in energy. From the photoelectron point of view, this is equal to shifting the potential curves by $\hbar\omega - KER$. As a result, the first peak in the photoelectron spectrum is harmonic 15.

potential curves in Fig. 5.1. On the other hand, higher sidebands show some phase variations, which could be attributed to the presence of the different resonant states at higher energies (26-36 eV), as will be discussed in more depth in the section that follows. These facts are served to support the assumption that phases of the escaping photo-electron are not influenced by the BS at least within the error bars presented here. In other words, one can assume that in the first step the electron is gone and not disturbed by the cation and one further photon merely dissociates the molecular ion by coupling the bound nuclear wave-packet in $1s\sigma_g$ to $2p\sigma_u$ states. This is an important point for the rest of the work. Another point is that, in the BS region there is still the contribution of GD, as shown in Fig. 5.21. This would mean that the contribution of the $q - 1$ harmonic with a phase shift of π to the oscillation of SB q is negligible.

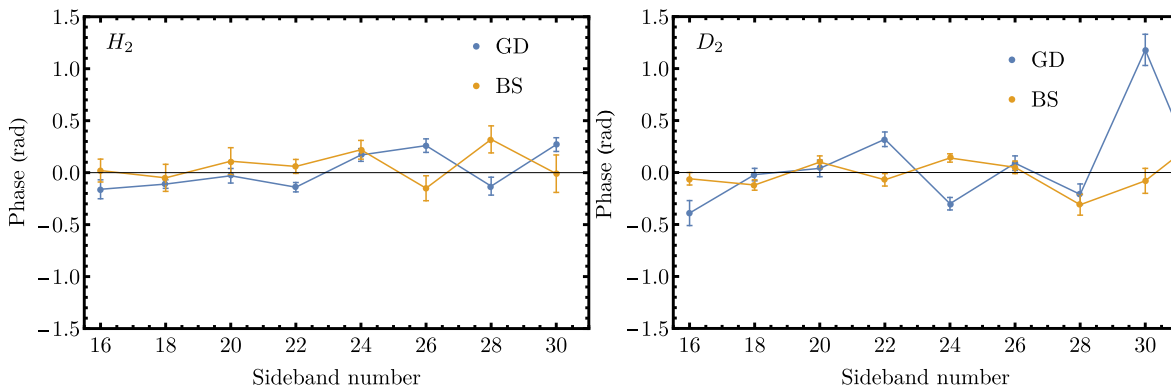


Figure 5.28: Comparison between sideband phases in the ground-state dissociation (GD) and bond softening (BS) of H_2 and D_2 .

5.4.2 Phase of the photo-electron wave-packet in the vicinity of Autoionizing states

Autoionization is present in multi-electron atomic and molecular systems [142]. These are known as Fano resonances in atoms [143]. In molecules, Fano resonances are disappeared due to the coupling between nuclei vibrational motion and electronic degrees of freedom [144][145]. H_2 manifests a strong coupling between decay of the electronic states and the nuclei motion, and the feature in the photo-electron spectrum begin to look more similar to atoms as the mass of the molecular system increases [146].

As discussed before, within the RABBIT scheme if one path experiences a resonance, for instance, in the vicinity of an autoionizing resonance, a phase jump is expected. Without the help of theory it is difficult to find out the exact origin leading to the phase jumps in molecular systems where many resonant states overlap. This is the case in H_2 and D_2 in the energy range of 25-35 eV where many autoionizing states are present. The theoretical calculations are very demanding in molecular systems concerning the auto-ionization due to the fact that a four-body system has to be treated quantum mechanically. Recently, there has been a simulation in the case of H_2 regarding the effect of autoionization [34] but only for parallel transitions (Q_1 series) since the perpendicular case becomes very complicated suggesting that the theory regarding the even the simplest molecular systems is far from being complete.

RABBIT Phases in Photo-dissociation of H_2

In Fig. 5.29, RABBIT phases for the GD case (KER:0-.38 eV) for both perpendicular ($90^\circ \pm 20$) and parallel ($0^\circ \pm 35$) orientations are given. The phases of all sidebands are almost identical in both cases. As for sideband 28, both orientations manifest the same phase

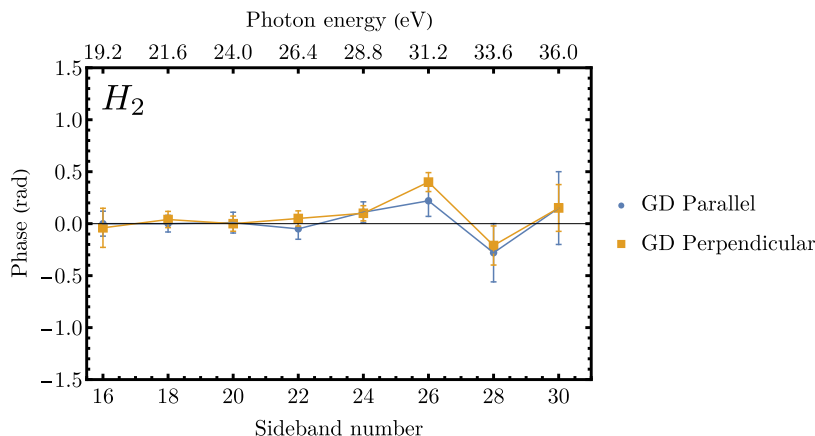


Figure 5.29: Comparison between sideband phases in parallel and perpendicular orientations in ground state dissociation (GD) for a KER region of 0.0-0.38 eV in H_2 .

trend. Otherwise, the overall trend is almost linear. To find out about the origins of these phase differences, a more detailed phase extraction is presented in Fig. 5.30. Phases of each sideband is extracted for much smaller KER regions of 0.1 eV for both parallel and perpendicular orientations. Perpendicular phases can only be extracted for KERs up to 0.4 eV since the number of events in this case for higher KERs is very small. This is due to the fact that bond softening occurs only in parallel orientation and, as a result, one has to reduce considerably the angle integration region so that the effect of the bond softening can be suppressed. The phases in the region 0.4-0.5 eV can not be extracted since this is the overlap region of BS and GS. According to Fig. 5.30, in the KER region 0-0.4 eV, all sidebands manifest no considerable phase variations within error bars for both parallel and perpendicular orientations. Additionally, in each orientation the phases are almost flat over the entire KER region 0-0.4 eV. Regarding higher KERs, on the other hand, one can see phase variations for higher sidebands 22, 24, 26, 28, and 30 corresponding to the photon energy range of 26.4-36 eV. The following conclusions are drawn based on these observations: almost all sidebands do not show considerable phase variations neither for perpendicular, nor for parallel orientations in the GD region (KER 0-0.4 eV) suggesting that there are no considerable contribution of the resonant states in this KER region and, as a result, phase are linear. However, higher sidebands are modified in the presents of resonant states in the BS region (KER 0.5-0.8 eV). These are in contrast to the observed effects in D_2 .

RABBIT Phases in Photo-dissociation of D_2

Fig. 5.31, sideband phases for parallel and perpendicular orientation in D_2 regarding the ground state dissociation (KER 0-0.35 eV). The perpendicular case shows no considerable phase variational for all sidebands except for sideband 30. In the parallel orientation,

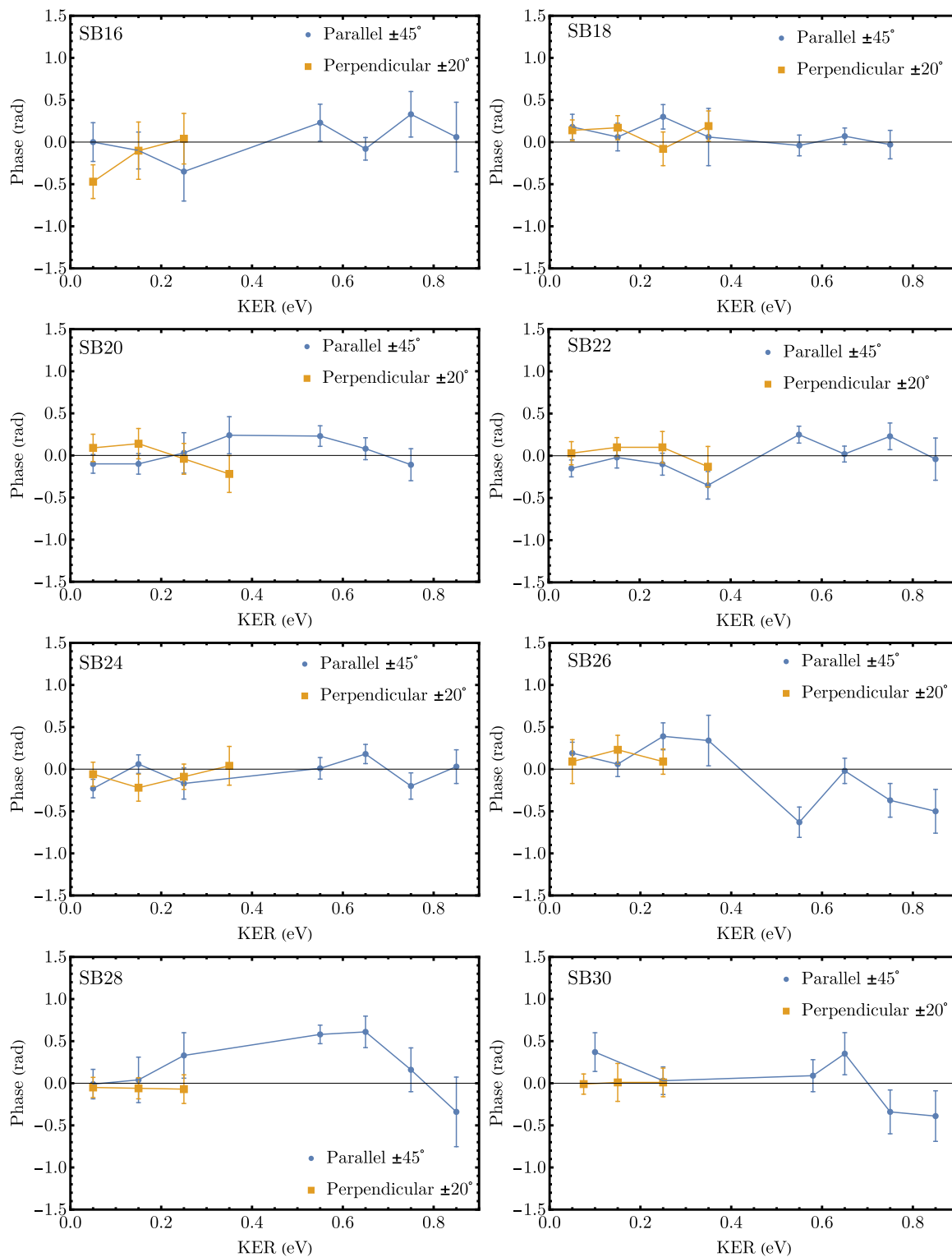


Figure 5.30: Phases of different sidebands for small KER regions for parallel and perpendicular orientations in H_2 . Due to a low number of events in sideband 30 the integration interval is larger.

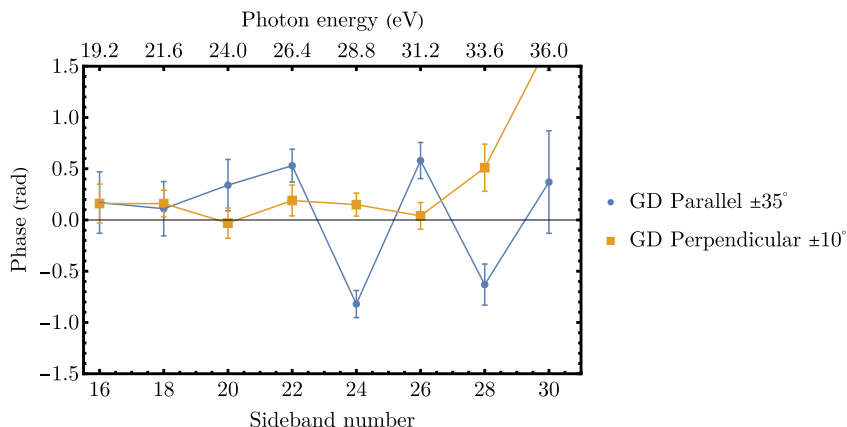


Figure 5.31: Sideband phases for parallel and perpendicular orientations with respect to the field polarization for a KER region of 0.0-0.38 eV in D_2 .

on the other hand, striking phase jumps can be seen for higher sidebands which one can attribute to the DESs. Fig. 5.32, shows phases of each sideband as a function of KER for both parallel and perpendicular orientations similar to H_2 . At the first glance, one can notice that the phases for KERs higher than 0.5 eV are almost flat contrary to H_2 . However, sideband phases in lower KERs (0-0.35 eV) show strong modulations for sidebands higher than 20 in the parallel orientation.

The Origin of the Observed Differences in H_2 and D_2

As opposed to the similar electronic dynamics in H_2 and D_2 , the nuclei move slower in D_2 . The resonant Q_1 and Q_2 states are electronic states and, as a result, they have the same autoionization lifetime in both H_2 and D_2 . This lifetime is determined by the electron-electron correlation. As a consequence, the nuclei move along the same electronic potential curves in both systems. This movement, however is slower in D_2 compared to H_2 due to the mass difference. For instance, imagine a transition to $Q_1^1\Sigma_u^+$ at nuclear distance R . $Q_1^1\Sigma_u^+$ autoionizes after time t . During this time H_2 has moved further down the $Q_1^1\Sigma_u^+$ compared to D_2 resulting in dissociation with higher KERs for H_2 than D_2 . This explains the observed difference. The effects of the resonant states are more prominent in lower KERs in D_2 but in higher KERs in H_2 . The theoretical calculations of the photo-dissociation cross section in H_2 and D_2 , shown in Fig. 5.33, support this argument. In case of D_2 , the dissociation cross section is slightly shifted to the left with respect to H_2 at photon energies around 28 eV where one expects to couple to the lowest Q_1 curve.

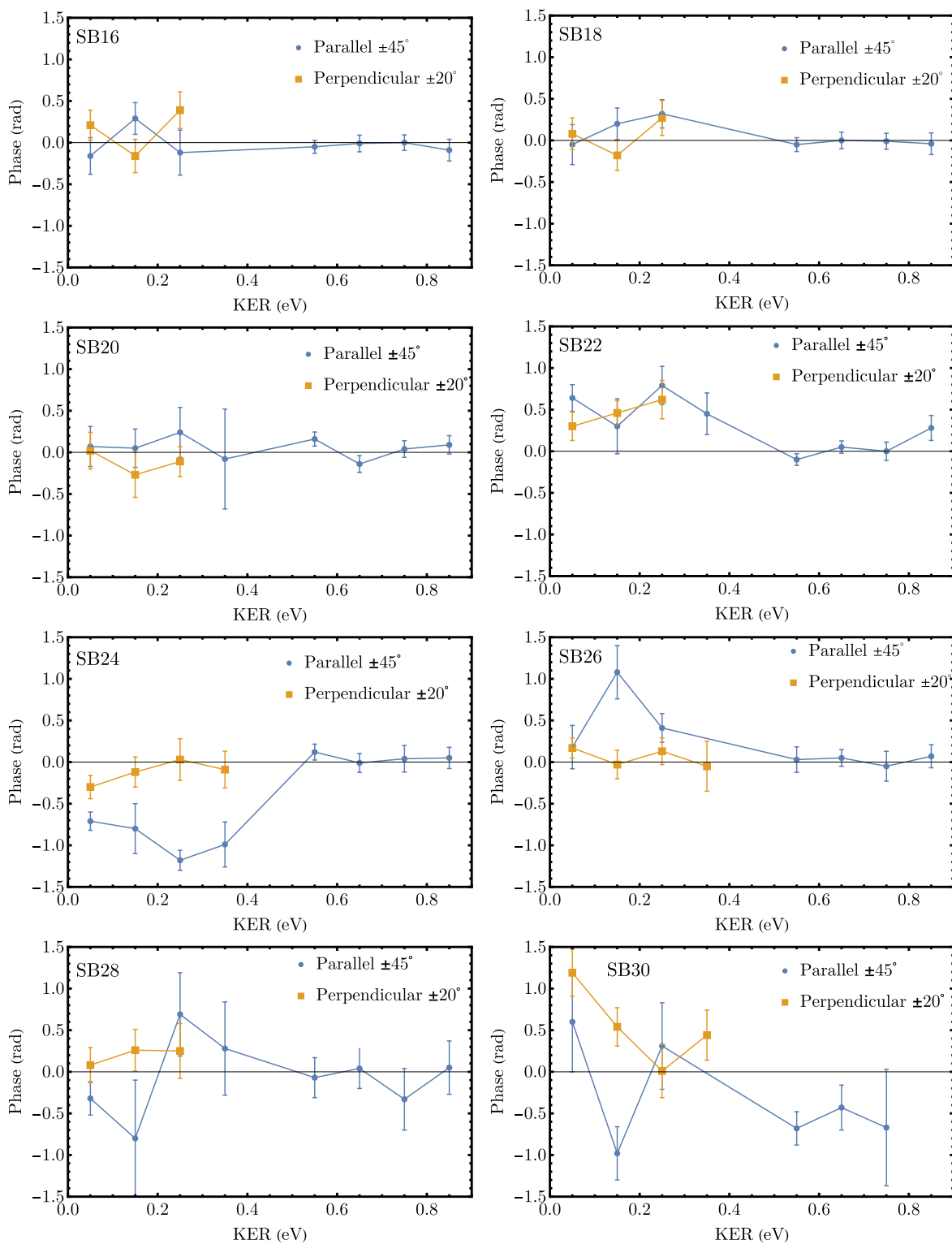


Figure 5.32: Phases of different sidebands for small KER regions for parallel and perpendicular orientations in D_2 .

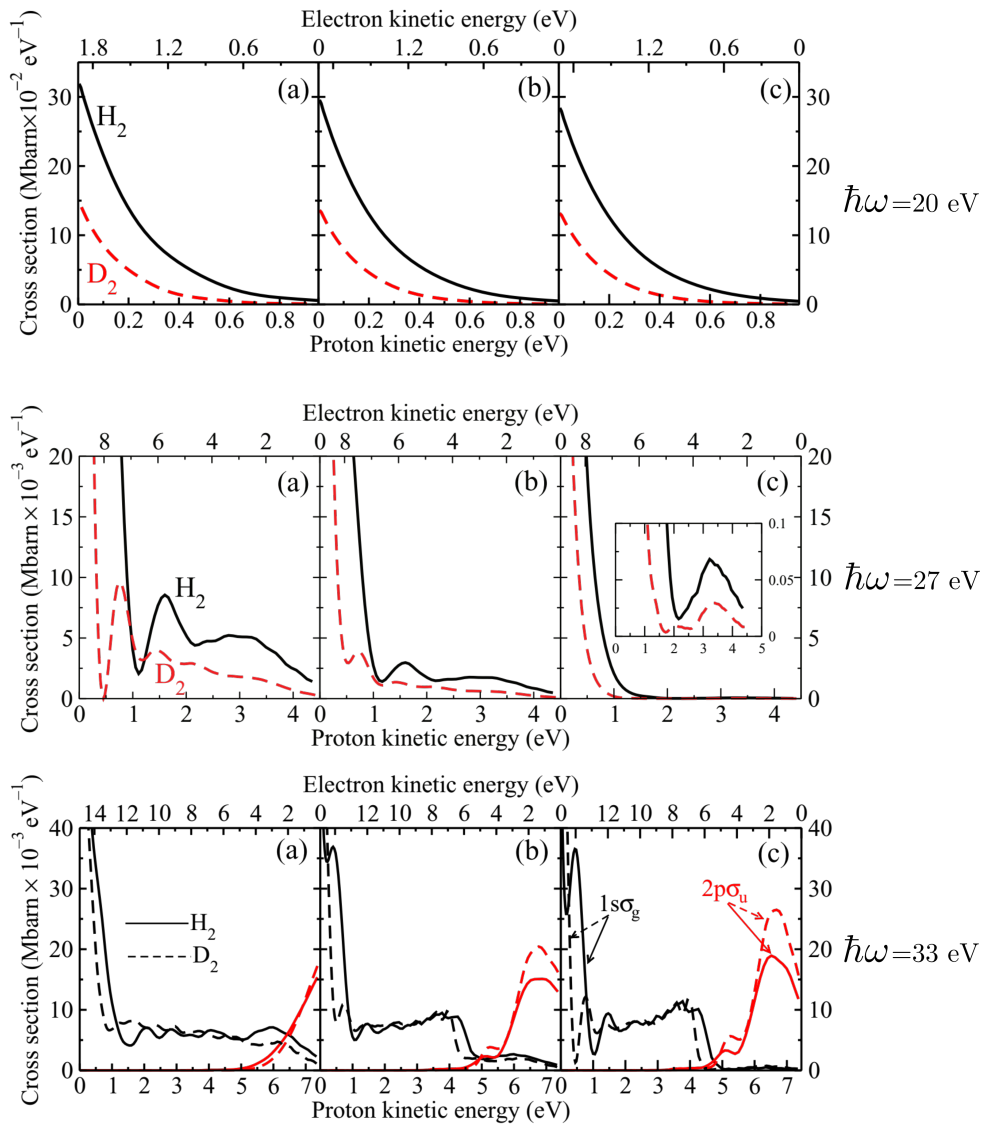


Figure 5.33: Cross section integrated over all electron emission angle as a function of proton kinetic energy for H₂ and D₂ for three different molecular orientations with respect to the polarization axis for photon energies 20, 27, and 33 eV. (a) θ = 0°, (b) θ = 54.7°, and (c) θ = 90°. Taken from [125]

Chapter 6

Electron Localization

As discussed in section 3.8, a left-right asymmetry of the electron emission in a dissociating molecule takes place when a coherent superposition of two molecular states with gerade and ungerade parities is present. This asymmetry is the localization of the electron on one of the two nuclei, and thus both "electron asymmetry", and "electron localization" can be used interchangeably. The localization is a function of the relative phases of the nuclear wavepacket within the two molecular states [19] as will be later demonstrated using a semi-classical simulation. In this chapter the experimentally observed localization of the electrons during photo-dissociation of H₂ and D₂ is presented. Firstly, experimental data is presented and the origin of the localization effect is discussed. Furthermore, a WKB simulation (carried out by Patrick Froß) which supports the observed phenomena is introduced. Finally, the localization as a function of the delay between the pump and probe pulses is addressed.

Before proceeding to molecular frame asymmetry, it is worthwhile to proof the validity of the experimental data. First and foremost, correction to the molecular frame (see section 4.3.6) by accounting for the electron recoil is essential, otherwise an artificial asymmetry will be produced. Secondly, since an asymmetry with respect to the molecular axis is of interest, any laboratory-frame related asymmetry must be removed. On this account, one can produce the asymmetry plot of KER vs electron energy with respect to the laboratory frame for both ions and electrons discussed in the following. The asymmetry parameter with respect to the laboratory frame for ions is defined $A = \frac{N_R^i - N_L^i}{N_R^i + N_L^i}$, where N_R^i is the number ions propagating in the right hemisphere in the lab frame (towards the ion detector), and N_L^i is the number of ions flying in the opposite hemisphere. The resulted asymmetry of the energy sharing is shown in the left panel of Fig. 6.1 for H₂. No obvious structure is present which depends on the emission direction of ions with respect to the lab frame. Regarding electrons, the same procedure is repeated. The asymmetry function $A = \frac{N_R^e - N_L^e}{N_R^e + N_L^e}$ is defined where N_R^e is the number of electrons with the emission angle in the hemisphere towards the ion detector, and N_L^e is the number of electrons going in

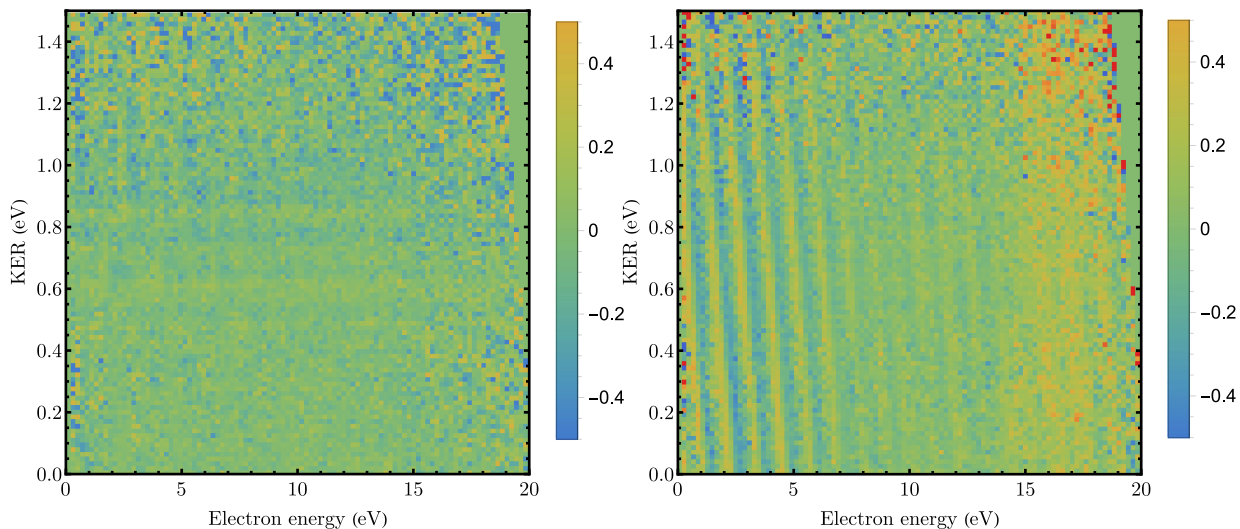


Figure 6.1: Asymmetry plot of KER vs electron energy for H_2 with respect to the laboratory frame. Left panel: Asymmetry parameter is shown with respect to ions. The orange color shows ions emitted in the hemisphere towards the ion detector (positive values) and the blue color shows the opposite. Right panel: Asymmetry parameter is shown with respect to the direction of electrons. The orange color shows electrons emitted in the hemisphere towards the ion detector (positive values) and the blue color shows the opposite.

the opposite direction. The asymmetry plot for energy sharing in this case is shown in the right panel of Fig. 6.1 in H_2 . Diagonal stripes for electron energies up to 7 eV are observed. This region moves by adjusting the longitudinal momentum of the electrons in post-analysis calibration but it does not have any influence on the molecular asymmetry presented in Fig. 6.2 and Fig. 6.4. Moreover, the central area (electron energies higher than 7 eV) shows an almost structureless region.

6.1 Molecular-Frame Asymmetry

The asymmetry parameter in the lab frame is defined as follows

$$A = \frac{N_{\alpha < 90} - N_{\alpha > 90}}{N_{\alpha < 90} + N_{\alpha > 90} - \delta}, \quad (6.1)$$

similar to Eq. 3.32, where δ , a small number, serves to avoid singularities in case $N_{\alpha < 90} + N_{\alpha > 90}$ vanishes. From now on, $N_{\alpha < 90}$ is referred to as *pro* and $N_{\alpha > 90}$ as *anti*.

The asymmetry of the energy sharing plot with respect to the molecular frame is shown in the right panel of Fig. 6.2 for H_2 molecules dissociating parallel to the polarization axis. The energy sharing plot for these molecules is shown in the left panel for reference. The

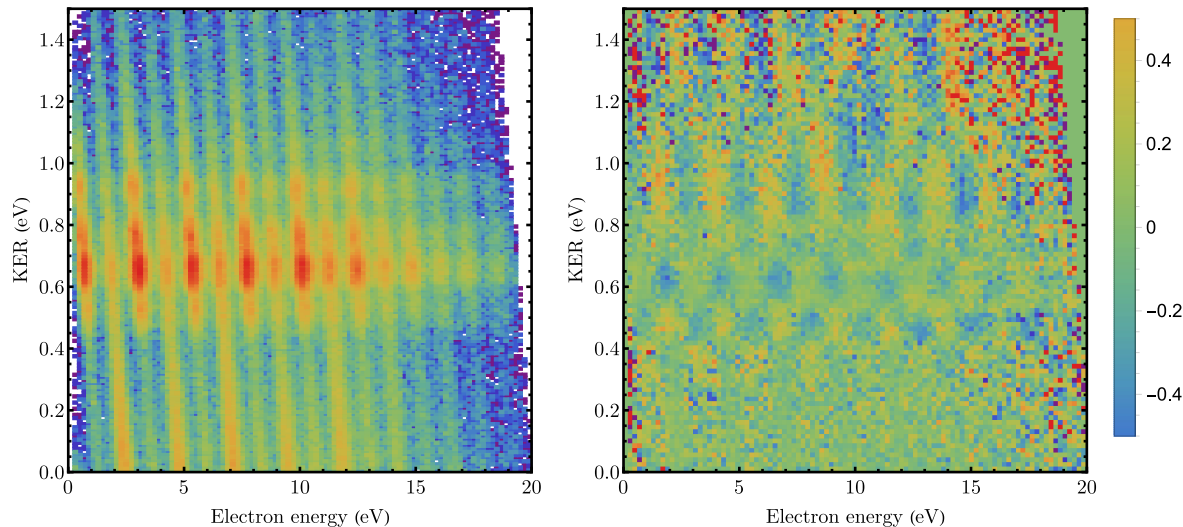


Figure 6.2: Left panel: Energy sharing plot in photo-dissociation of H_2 (coincidence $H^+ + e$) for KERs up to 1.5 eV for molecules dissociating parallel to the laser polarization. Right panel: The asymmetry plot of KER vs electron energy in H_2 for molecules dissociating parallel to the polarization axis. Positive values (red) show *pro* events, whereas negative values show *anti* events.

orange color shows a positive asymmetry (by definition according to Eq. 6.1). In this case, more electrons are to be found on the proton side, and the blue color shows the opposite case. As one can see, there is a striking pattern which is absent in Fig. 6.1. On a closer look, one can see that the lower region of the plot, which corresponds to KERs lower than 0.35 eV, is structureless. This region contains events related to the ground state dissociation (GD). On the other hand, for KERs higher than 0.35 eV, a noticeable oscillation between anti and pro as a function of electron energy as well as KER can be seen. The oscillation period is constant along the electron energy axis, whereas it changes as one moves vertically along a conservation line. For the purpose of visualization, one can make a projection of each energy conservation line (band) and plot the asymmetry. The results are shown in Fig. 6.3. As it is also visible in the left panel of Fig. 6.2, all high harmonic bands show the same trend in the asymmetry parameter. This is also true for sidebands. However, zero crossings are the same, as they are marked with vertical lines Fig. 6.3.

One can plot the same procedure for D_2 as well, resulting in Fig. 6.4, and Fig. 6.5. In this case, the effects are less pronounced, yet the overall structure is similar to that of H_2 . The physical reason of the observed asymmetry is given in the section that follows.

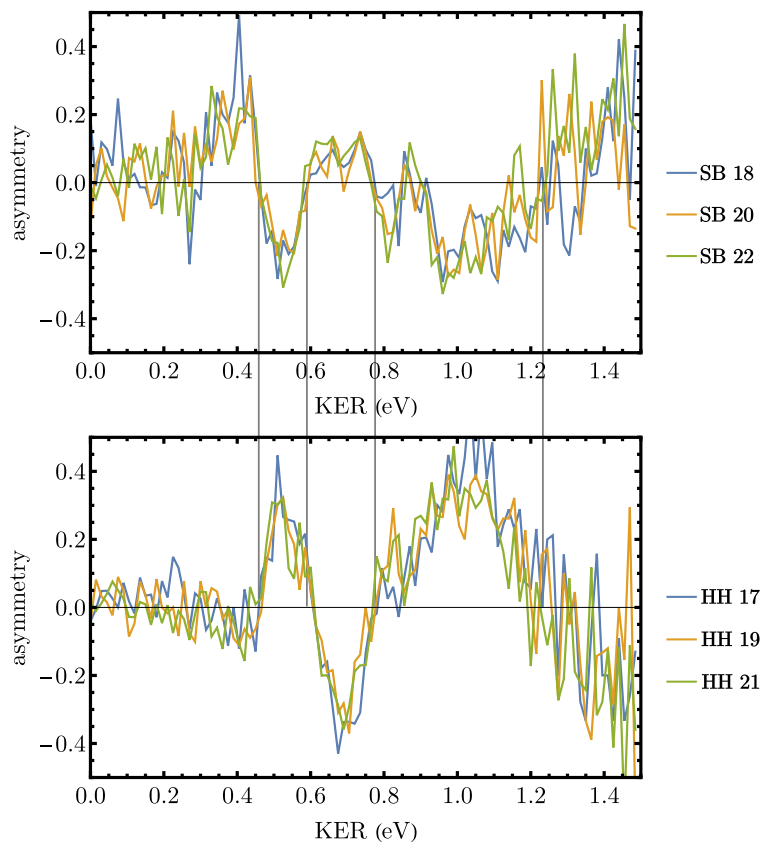


Figure 6.3: The asymmetry parameter for different energy conservation lines in Fig. 6.2 as a function of KER in the case of H_2 dissociating parallel to the polarization axis. The upper plot illustrates sideband (SB) 18, 20, and 22. The lower plot illustrates the higher harmonics (HH) 17, 19, and 21. Some of the zero crossings are shown with vertical gray lines.

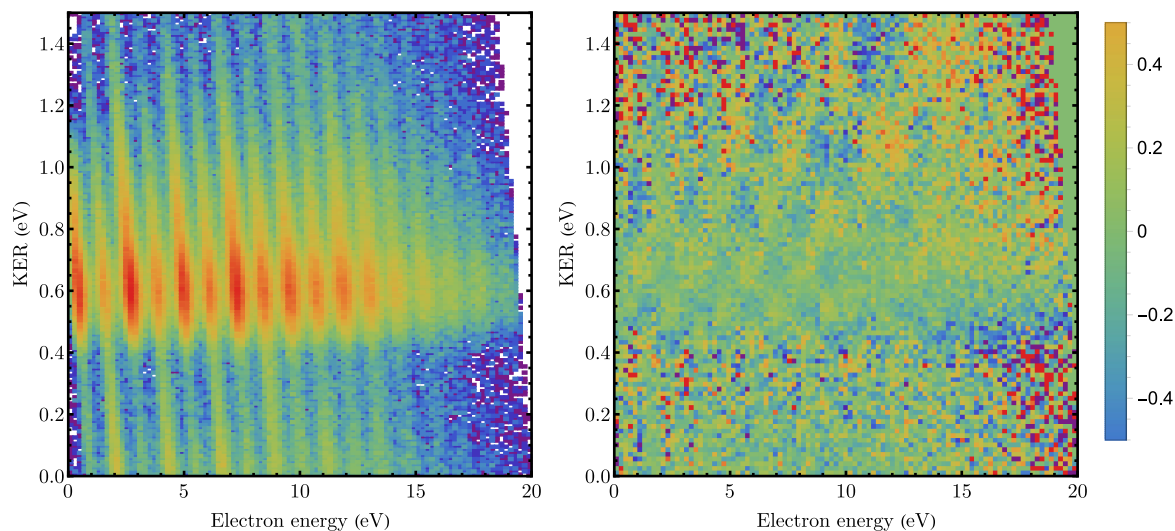


Figure 6.4: Left panel: Energy sharing plot in photo-dissociation of D_2 (coincidence $D^+ + e$) for KERs up to 1.5 eV for molecules dissociating parallel to the laser polarization. Right panel: Asymmetry plot of KER vs electron energy in D_2 for molecules dissociating parallel to the polarization axis. Positive values (red) show *pro* events, whereas negative values show *anti* events.

6.1.1 The Physical Origin of Asymmetry

In order to find out the mechanism responsible for the observed effects, one can look at the potential curves and the definition of asymmetry, namely, the superposition of two states with different parities leading to the same final state. As illustrated in Fig. 6.6, there are two paths which end in the same final KER and electron energy: bond softening (BS) and ground-state dissociation (GD). This region begins at around 0.35 eV in KER and extends up to 1.5 eV. This is the same region where an asymmetry is present. As discussed in section 5.2.1, the contribution of GD in case of D_2 is smaller compared to H_2 . This could be the reason why the structure in the asymmetry plot is less pronounced because the maximum asymmetry occurs when the contribution of the two pathways is the same.

In the following, the asymmetry in the energy sharing plots is presented for different intervals of the angle between the molecular axis with respect to the polarization of the laser field. As one expects, according to Fig. 6.7, the contrast of the asymmetry is more prominent when the dissociation orientation is parallel to laser field. If no angle condition is applied, as shown in the lowest right plot, the contrast is the smallest. Fig. 6.8 shows the symmetry plot from parallel to perpendicular, with the integration step of 15° . As one expects, the asymmetry structure gradually washes out as the orientation approaches 90° since the BS contribution disappears. In the next section, a semi-classical simulation is introduced that reproduces the observed effects.

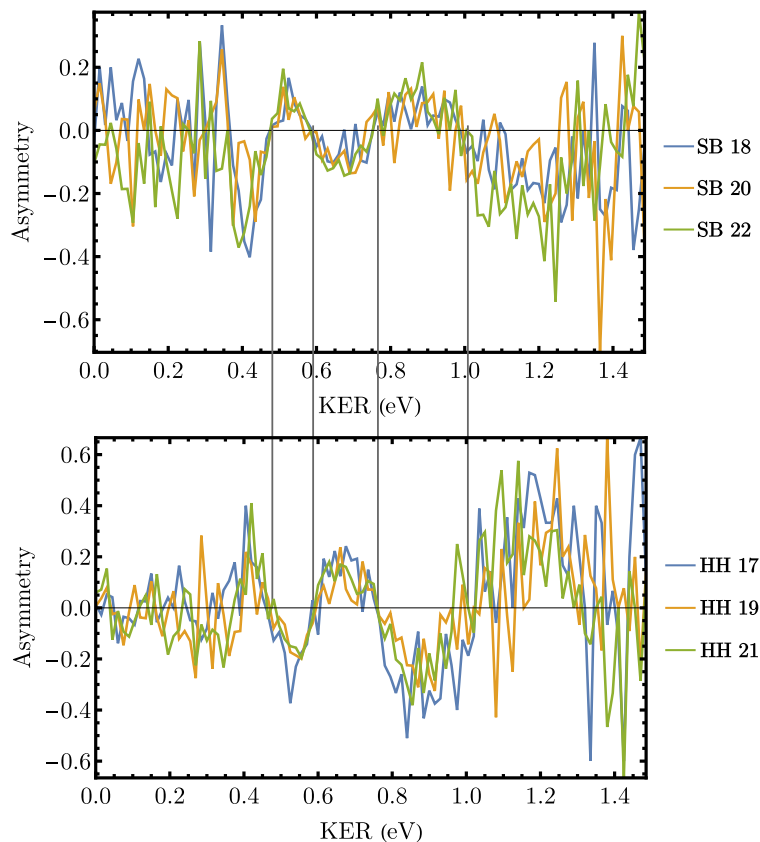


Figure 6.5: The asymmetry parameter for different energy conservation lines in Fig. 6.4 as a function of KER in the case of D_2 dissociating parallel to the polarization axis. The upper plot illustrates sidebands (SB) 18, 20, and 22. The lower plot illustrates the higher harmonics (HH) 17, 19, and 21. Some of the zero crossings are shown with vertical gray lines.

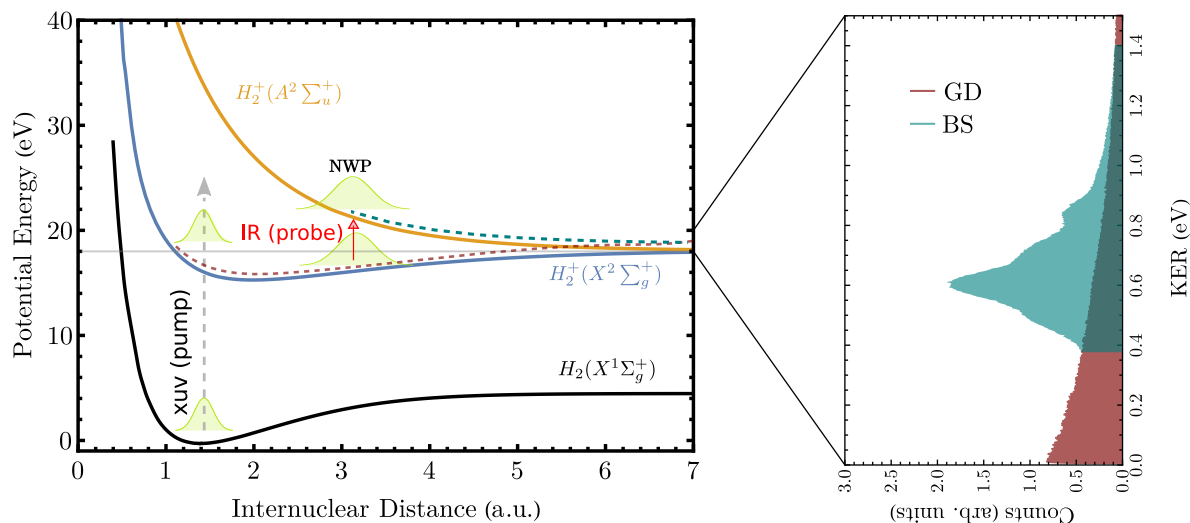


Figure 6.6: Asymmetry or localization is a result of the interference of two quantum paths leading to the same final state. First path: An XUV photon ionizes the H_2 molecule from $X^1\Sigma_g^+$ to the bound ground state of H_2^+ ($X^2\Sigma_g^+$). For photon energies higher than the dissociation potential, shown with the horizontal grey line at 18.1 eV, the molecule can dissociate following the brown dashed line. Second path: After the ionization with an XUV photon, the bound molecular wavepacket in the ground state of the molecular ion can absorb an additional IR photon (shown not to scale) as it propagates towards a higher internuclear distance, where the energy difference between $X^2\Sigma_g^+$ and $A^2\Sigma_u^+$ is accessible with an IR photon. $A^2\Sigma_u^+$ being a repulsive potential curve, the molecule dissociates at higher internuclear distances following the green dashed line. The panel on the right shows the KER distribution for two measurements. The brown area depicts a measurement done only with the XUV beam, whereas the green one with XUV+IR (pump and probe). The lower section (KER 0-0.38 eV) of the green area is removed so as to emphasis the overlap region.

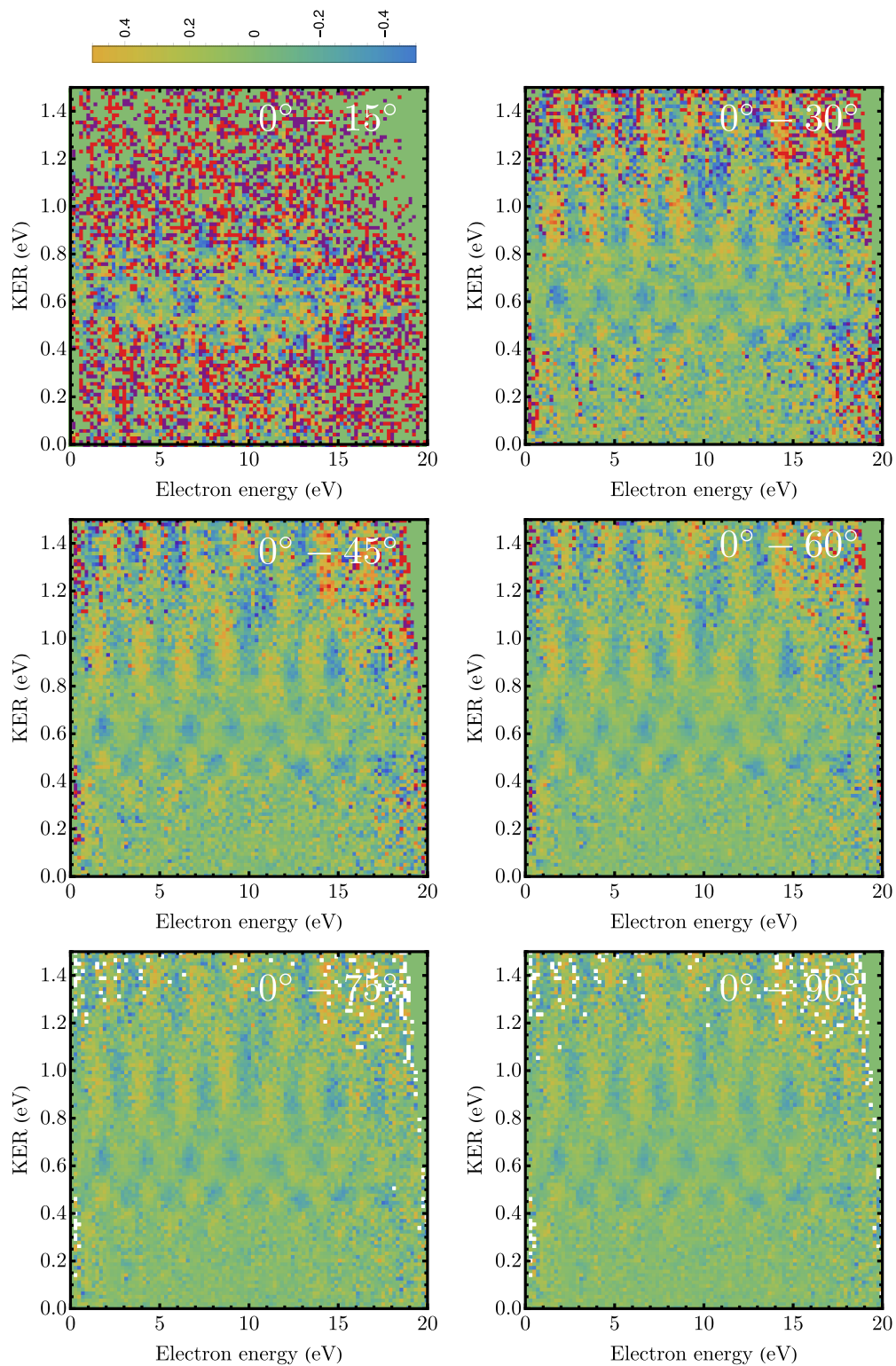


Figure 6.7: Asymmetry plots of KER vs electron energy for H₂ for different orientations of the molecule with respect to the polarization axis. Positive values (red) show *pro* events, whereas negative values show *anti* events.

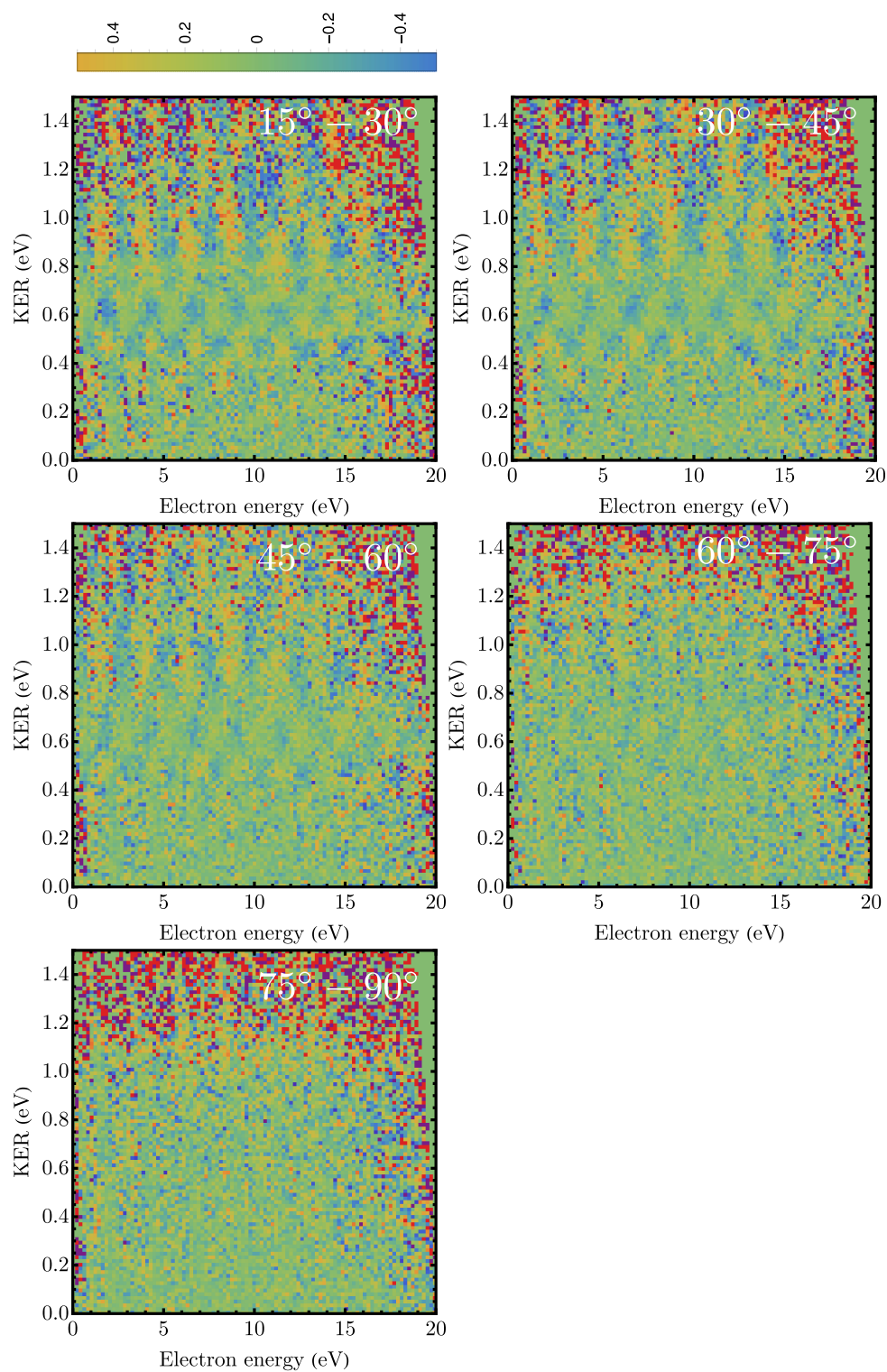


Figure 6.8: Asymmetry plots of KER vs electron energy for H₂ for different orientations of the molecule with respect to the polarization axis. Positive values (red) show *pro* events, whereas negative values show *anti* events.

6.2 Semi-Classical Simulation of Electron Localization

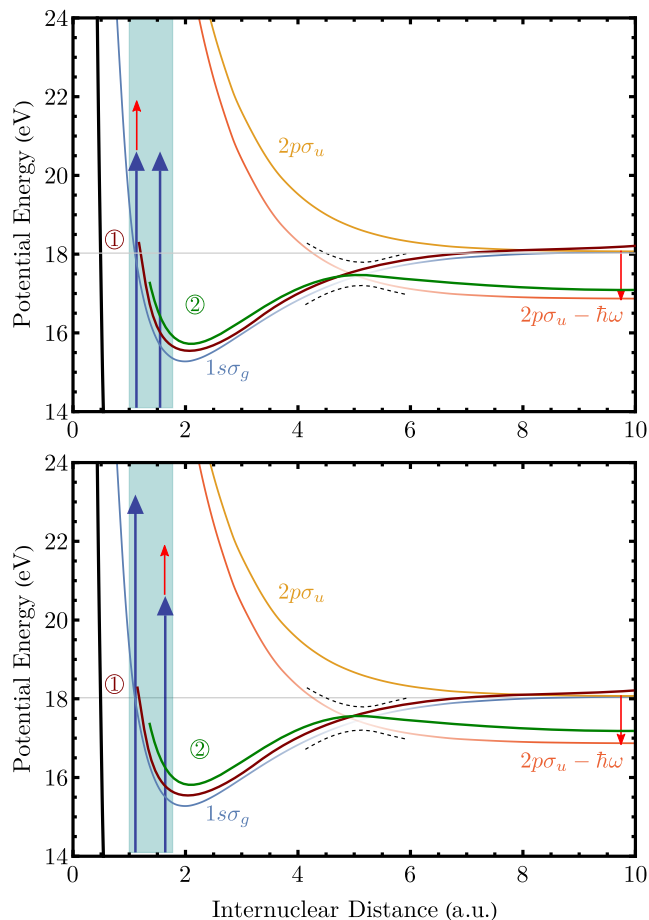


Figure 6.9: Schematic illustration of the relevant potential curves and their corresponding pathways used in the integration during the semi-classical simulation.

According to the semi-classical simulation (performed by P. Froß) based on [104][147] using WKB approximation introduced in section 3.6, one can model the classical motion of the nuclei on different potential curves to keep track of the quantum phases. The ultimate goal is to simulate Eq. 3.40 by calculating variables c_1 and c_2 corresponding to the two different pathways. Starting off with rewriting these variable in the polar form

$$c_1 = r_1 e^{i\xi_1}, \quad c_2 = r_2 e^{i\xi_2}, \quad (6.2)$$

where $r_{1,2}$ are the occupation amplitudes and $\xi_{1,2}$ phases of the states. Since $r_{1,2}$ determine only the magnitude of the asymmetry which can only be calculated using a full quantum mechanical approach, one can set them to unity. Phases are composed of two factors: ϕ is the phase of the nuclear wave packet accumulated along a potential curve, and χ is attributed to electronic transitions. Rewriting the asymmetry parameter Eq. 3.40

$$\begin{aligned}
A &= \frac{2\text{Re}[c_1 c_2^*]}{|c_1|^2 + |c_2|^2} \\
&= B \cos(\Delta\phi + \Delta\chi),
\end{aligned} \tag{6.3}$$

with $\Delta\phi = \phi_1 - \phi_2$ being the difference of the quantum phase for different pathways, whereas $\Delta\chi = \chi_1 - \chi_2$ is the phase difference of the electronic transitions. The former is calculated numerically using the WKB approximation, while the latter is derived using a quantum mechanical approach. The constant B is used to adapt the magnitude of the simulated asymmetry to the observed one, otherwise the above equation oscillates between -1 and 1. Nuclear phases can be calculated using Eq. 3.28

$$\phi = \int_R^\infty \sqrt{2m[E - V(R)]} dR, \tag{6.4}$$

where m is the reduced mass and the integrand is the nuclear momentum. Note that in the above equation, the term iEt is not included because this term eventually cancels out in the relative phase due to the fact that the final state has the same energy. The integral can be numerically evaluated for each pathway. In this case, the candidates are the ground state dissociation along the diabatic $1s\sigma_g$ of the cation and the adiabatic field-induced potential curve $2p\sigma_u - 1\omega$, as depicted in Fig. 6.9 with brown ① and green ②, respectively. The width of the one-photon avoided crossing is given by Eq. 3.30. Only pathways ① and ② can lead to the same electron energy and KER. In order to calculate the phase difference, the above equation is solved once for pathway ①. The starting point is chosen on the $1s\sigma_g$ curve, 0.6 eV above the dissociation limit, depicted by the gray horizontal line. The integral is solved numerically in the limit $R \rightarrow \infty$ resulting in ϕ_1 .

The starting point of the pathway ② is the starting point of ① $- 1\hbar\omega$ on the same $1s\sigma_g$ curve resulting in ϕ_2 . Eventually, the phase difference $\phi_1 - \phi_2$ is inserted in Eq. 6.3. Setting $\Delta\chi = 0$ and B to fit the observed amplitude results in the left panel of Fig. 6.10 in the case of H_2 . As for D_2 , one can use the same obtained value for H_2 and multiply them by $\sqrt{2}$ to account for the mass difference in Eq. 6.4. The results are shown in the right panel of Fig. 6.10. The first two zero crossings can be well simulated.

The derivation of the electronic phase χ is not included in this work but the interested reader can find it in [61][62]. This phase originates from the argument of the one-photon matrix element ($M^{(1)} \rightarrow \pi$) and two-photon matrix element ($M^{(2)} \rightarrow \pi/2$). In the case of the upper panel of Fig. 6.9

$$\begin{aligned}
\Delta\chi^1 &= \chi^{\text{①}} - \chi^{\text{②}}, \\
&= \frac{\pi}{2} - \pi = -\frac{\pi}{2},
\end{aligned} \tag{6.5}$$

and that of the lower panel

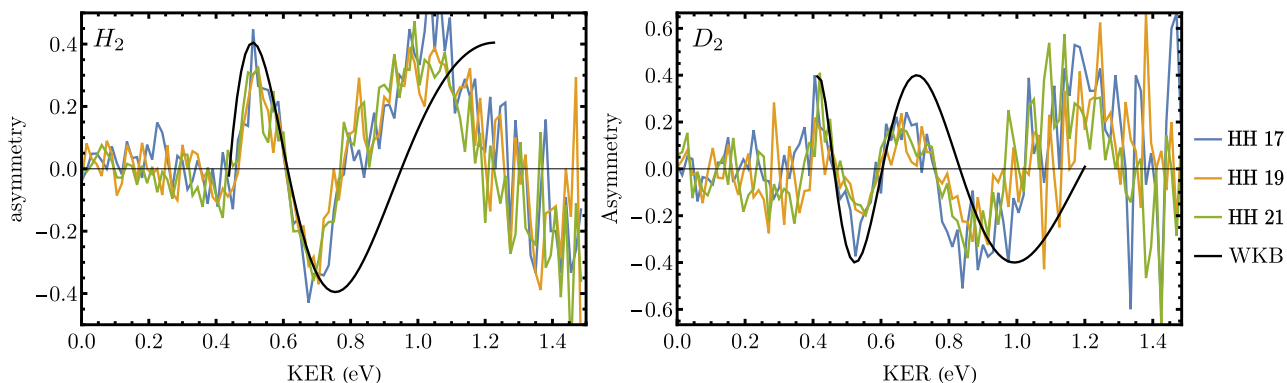


Figure 6.10: Comparison between experimental data and the results of the semi-classical simulation. The asymmetry parameter for conservation lines (HH) 17, 19, and 21 in the parallel orientation are shown. The WKB simulation is shown with the black curve. Left panel: H_2 . Right panel: D_2 .

$$\begin{aligned} \Delta\chi^2 &= \chi^{①} - \chi^{②}, \\ &= \pi - \frac{\pi}{2} = \frac{\pi}{2}, \end{aligned} \quad (6.6)$$

resulting in the relative phase of $\Delta\chi^1 - \Delta\chi^2 = \pi$ which explains the π phase jump in the asymmetry plot between one band and its adjacent ones. The results are shown in Fig. 6.11 for H_2 and D_2 . The electronic phase ($\Delta\chi$) in Eq. 6.3 takes only two values: 0 and π depending on the number of absorbed photons in each process.

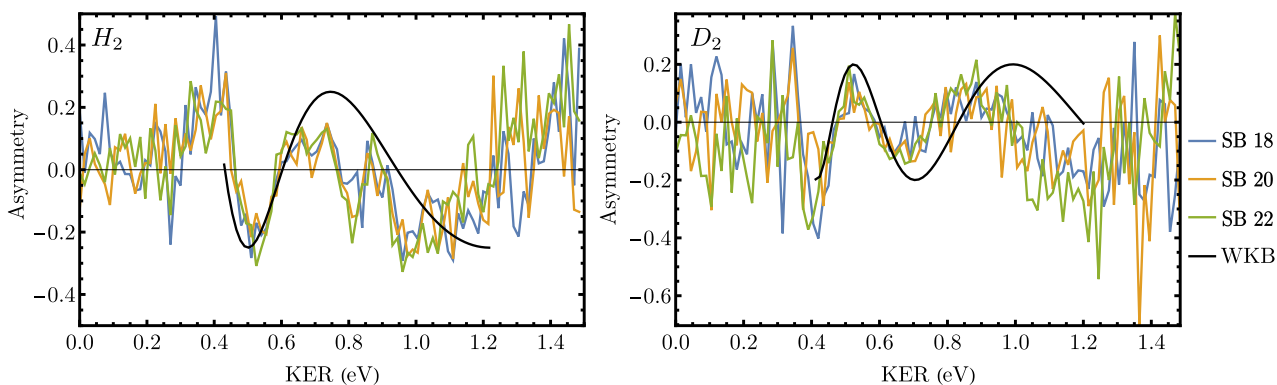


Figure 6.11: Comparison between experimental data and the results of the semi-classical simulation. The asymmetry parameter for energy conservation lines (SB) 18, 20, and 22 in the parallel orientation are shown. The WKB simulation is shown with the black curve. Left panel: H_2 . Right panel: D_2 .

Another feature is present in the asymmetry plot of energy sharing in both H_2 and D_2 at an electron energy of around 11 eV and KER of 1.1 eV. This region corresponds to

sideband 24 and high harmonic 25 with a photon energy of 28.8 and 30 eV, respectively, and exists only in the parallel transition, but the reason for this feature is not clear.

6.3 Probe Beam Intensity Dependence

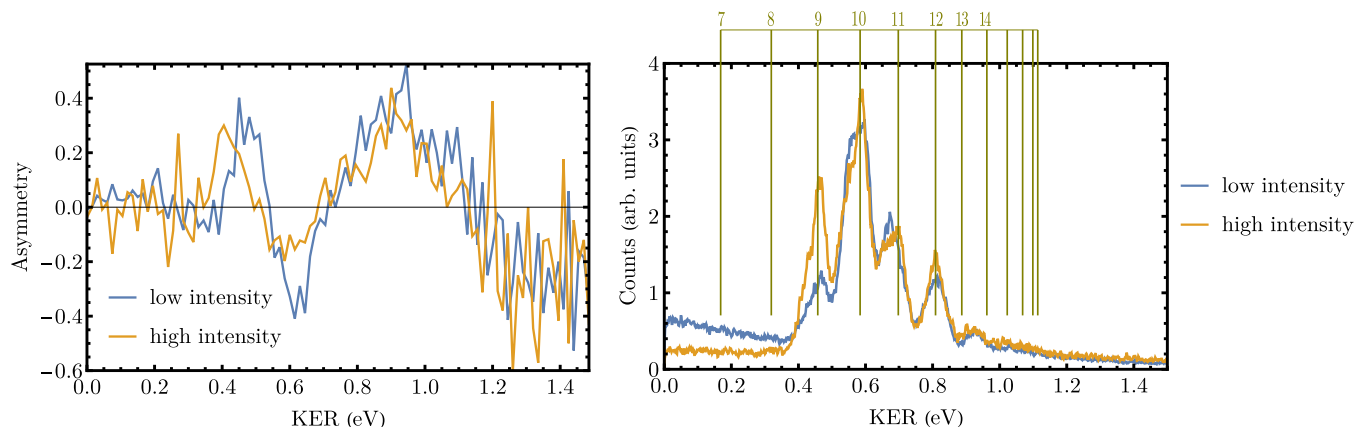


Figure 6.12: Right panel: KER distributions corresponding to two H_2 measurements where the intensity of the probe IR beam is different. In the brown curve, the contribution of vibrational level $\nu = 9$ is much higher compared to the blue curve where the intensity is lower. Left panel: The comparison of the asymmetry parameter of the second band (high harmonic (HH) 17) in the energy sharing plot for two measurements. The zero crossings in the brown curve which correspond to a higher probe beam intensity have shifted to lower KERs.

As discussed previously, by increasing the intensity of the probe IR beam, the gap of 1-photon avoided crossing becomes larger and, as a result, the KER distribution changes. The effect of the intensity also shifts the observed asymmetry zero crossings to smaller KER values. Fig. 6.12 shows two measurements with different probe intensities. The right panel illustrates the two KER distributions. The contribution of the vibrational level $\nu = 9$ is significantly larger in the brown curve due to a higher probe beam intensity. The left panel shows the asymmetry for high harmonic (HH) 17 in both measurements. Not only does the zero crossing shift to the left, but the periodicity also changes. The semi-classical simulation reproduces exactly the same trend as a function of intensity, as illustrated in Fig. 6.13.

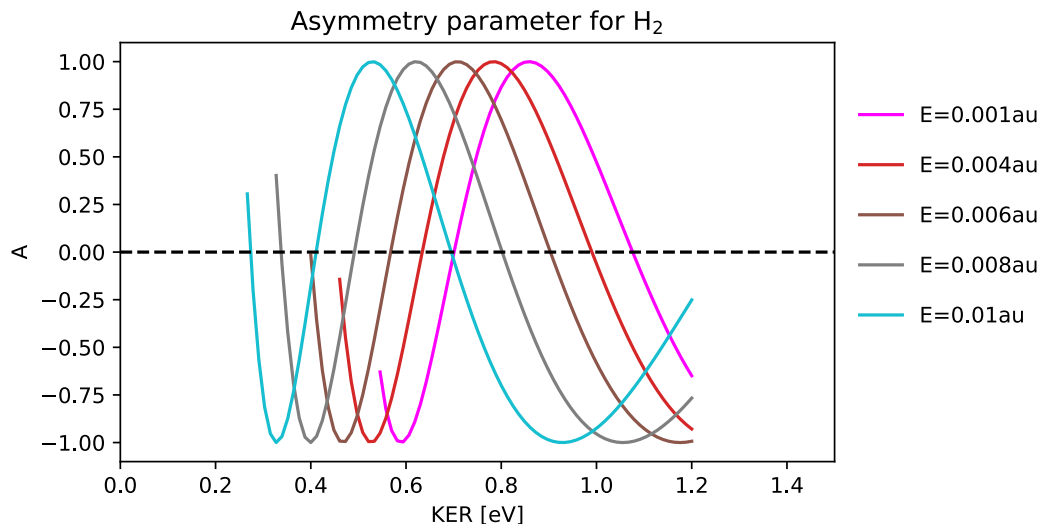


Figure 6.13: Semi-classical simulation of the asymmetry parameter for H_2 using the WKB approximation as a function of the intensity of the IR-probe beam. The zero crossings of the asymmetry parameter move towards lower KERs with increasing intensity. The simulation reproduces the same trend observed in the experimental data. Credits: Patrick Froß.

6.4 Attosecond time-resolved electron Asymmetry

The localization of the electron in the molecular frame as a function of the delay between the XUV and IR beam is briefly addressed in the section. A complete treatment of this topic, however is beyond the scope of this work. The results will be presented in other publications.

Delay dependence can be divided into two categories. Firstly, how the phase of the electronic wave-packet changes for pro and anti electrons. In other words, how the RABBIT phases of electrons propagating with the ion differ from those propagating with the neutral H atom. Second, the asymmetry parameter as a function of the delay. These two cases are similar but not the same. The sideband oscillation for pro electrons is given by

$$S_p = C_p \cos(\omega t - \theta_p) + D_p, \quad (6.7)$$

and for anti electrons

$$S_a = C_a \cos(\omega t - \theta_a) + D_a, \quad (6.8)$$

where C and D are constants, and θ_p and θ_a are the phases of pro and anti sidebands, respectively. By putting these two equations in Eq. 6.1, the asymmetry parameter becomes

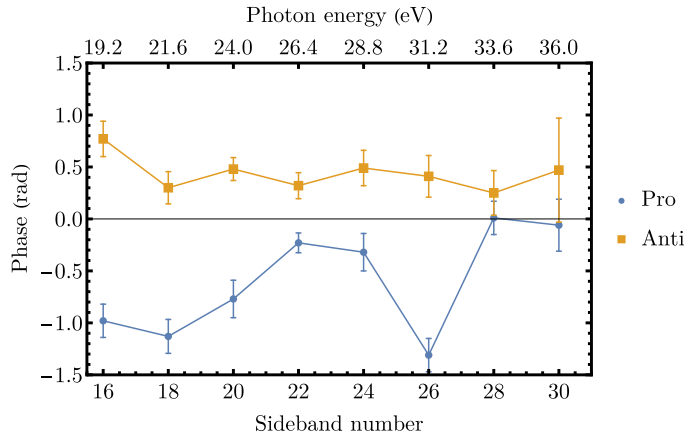


Figure 6.14: Sideband phases for anti and pro cases in H_2 for the KER region 0.5-.06 eV for molecules dissociating parallel with respect to the polarization axis.

$$A = \frac{S_p - S_a}{S_p + S_a}. \quad (6.9)$$

As one can see, the asymmetry parameter depends on the phases of the sidebands. This dependence is, however, more complicated than just the difference between RABBIT phases θ_p and θ_a since the amplitudes and offset values are also different. As an example, the RABBIT traces for pro and anti sidebands are given in Fig. 6.14 for the KER region of 0.5 to 0.6 eV. There are striking phase variations for SB phases in the pro and anti cases. The modulation of the asymmetry plot as a function of the delay between the XUV and IR pulses is illustrated in the upper panel of Fig. 6.15. A region where the modulation is the most pronounced is marked with a white box. The projection of the events in the box onto the delay axis is shown in the lower panel and a sinusoidal function with the a frequency of 2ω is fitted, where ω is the frequency of the probe beam.

In conclusion, both Fig. 6.14 and Fig. 6.15 show that the asymmetry parameter changes as a function of the delay between two pulses. In other words, one can manipulate the localization of the electron with respect to the molecular frame by varying the delay between the pump and the probe pulses.

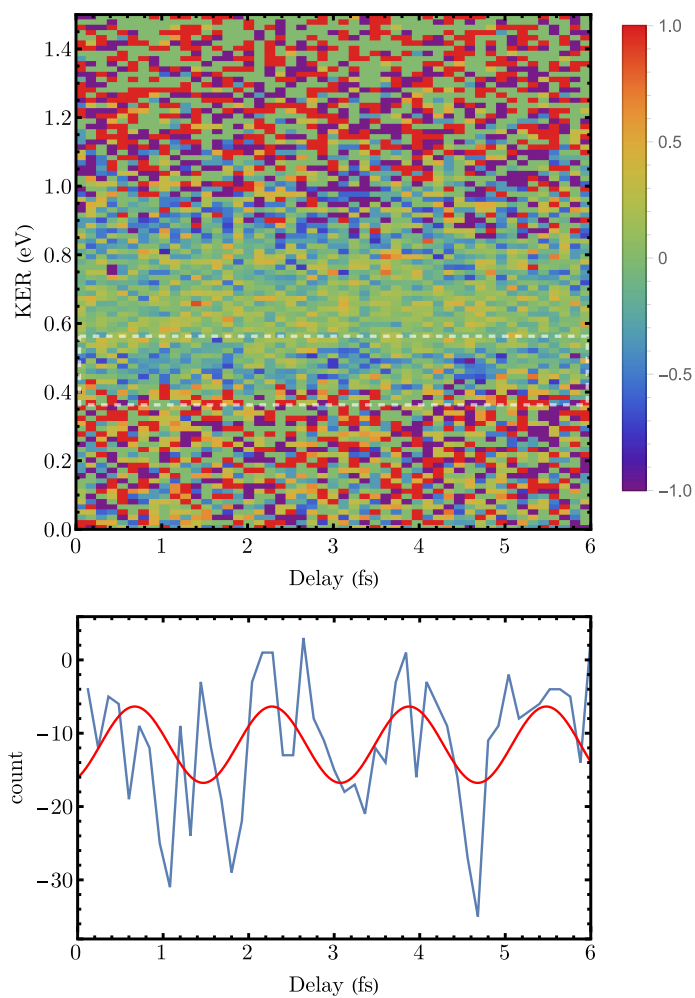


Figure 6.15: Upper panel: The asymmetry parameter as a function of the delay between the XUV-pump and IR-probe for sideband 16 in H_2 . Lower panel: The projection of the marked box in the upper plot onto the delay axis. A sinusoidal function with a frequency of 2ω is fitted to the experimental data.

6.5 Previous Measurements and Discussion

Generally, within a diatomic molecule, it is not inherently predetermined which atom loses its electron as a consequence of photodissociation. The average electron distribution is symmetric around the atoms. This symmetry can, however, be broken by introducing an artificial asymmetry, e.g., a strong asymmetric laser field. A neat example is the ground breaking experiment with a CEP stabilized laser pulse by Kling and co-workers [7]. Another example, is a complete kinematically coincidence measurement [148], where the asymmetry as a function of CEP phases was demonstrated, as well as the dependence of the asymmetry on the proton energy which was supported by TDSE calculations. Another example regarding the control of the electron localization was performed with an isolated attosecond pulse probed by a time-delayed NIR pulse [8]. For a comprehensive overlook on theoretical and experimental research regarding this topic refer to [15].

All above mentioned experiments have one feature in common, namely, a molecule which is symmetric in nature is influenced by an asymmetric distorting effect, that is the laser field, to introduce asymmetric electron emission during photo-dissociation in the **laboratory frame**. A time dependent control of the electron emission can then be controlled if one varies the artificial asymmetry (laser field) as a function of time. The experimental data presented in this work, however, shows an asymmetry in the localization of electrons in the **molecular frame** of reference which can be controlled by the number of absorbed photons as well as the delay between XUV-pump and IR-probe pulses.

Chapter 7

Summary and Outlook

An attosecond beamline was designed and constructed in the framework of this work. The light source is provided by a commercially-available high-power fiber laser made by Active Fiber Systems GmbH. A Mach-Zehnder-configuration interferometer was used to perform XUV-pump IR-probe experiments. The laser beam was split into two beams. The first beam (pump) used to produce an attosecond pulse train (APT) with high harmonic generation (HHG). A variable time delay was introduced in the second beam (probe) with respect to the pump beam with a piezo-driven delay stage. A reaction microscope used as the spectrometer to detect the fragments resulting from the interaction between laser pulses and the target. In a series of measurements H_2 and D_2 were investigated. Results are summarized as follows.

With photon energies higher than the ionization potential of H_2 and D_2 ($I_p=15.46$ eV) a transition from the ground state of the neutral molecule to the ground state of the molecular ion becomes possible. The resulted fragments are H_2^+ or D_2^+ and an electron. The photoelectron spectrum in $H_2^+/D_2^+ + e$ coincidence shows the peaks corresponding to harmonics in an APT. The same spectrum, resulting from an interaction with an APT in the presence of a weak dressing IR field, shows sidebands between high harmonic lines. By plotting the photoelectron spectrum as a function of the delay between the APT and IR pulse, one obtains the RABBIT traces where the sidebands oscillate as a function of the delay.

With energies higher than the dissociation limit of H_2 and D_2 ($I_D=18.1$ eV) one can dissociate the molecules. This channel has a much smaller cross section compared to single ionization. The detected fragments are H^+/D^+ and an electron. The detection of both fragments in coincidence allows one to retrieve the molecular orientation at the instance of the photon-molecule interaction. The photodissociation results from different mechanisms, such as direct dissociation composed of ground state dissociation (GD) and dissociation via the first excited state of the molecular ion, and indirect dissociation by

means of doubly-excited states (DEs). DERs being resonant states, they can be populated only in particular orientations of the molecule with respect to the polarization axis of the light. The ground state contribution to the overall events is much larger than other mechanisms.

The energy sharing between fragments of the dissociation can be reconstructed using the coincident detection ability of the ReMi. The energy sharing plot contains diagonal lines, known also as conservation lines, with a slope of -1 as a consequence of energy conservation. This plot allows one to uncover the mechanism responsible for the dissociation. In case of the dissociation with only an APT, the diagonal lines manifest the harmonic peaks in the APT. In case of dissociation with a combination of an APT and IR pulse, sidebands appear in the energy sharing plots. The presence of a dressing IR field also results in an enhancement of the dissociation known as bond softening (BS) in the Floquet picture. BS allows to resolve the vibrational levels of the ground state of the molecular ion.

Using an interferometric method, known as RABBIT, the dynamics of the dissociative photoionization of H_2 and D_2 on an attosecond timescale is studied. It is shown that the sideband phases manifest modulations if one of the pathways leading to a sideband hits a resonant state. These phase variations change as a function of the kinetic energy release (KER). By comparing H_2 and D_2 , one can see differences as a result of the heavier mass of D_2 . A next step following the presented results would be to compare them with TDSE calculations in order to uncover the exact origins of the phase variations. For instance which doubly-excited state exactly contribute to the phase jumps. As far as the experiments are concerned, one can extract the sideband phases for higher KERs by doing measurements with a much longer acquisition time.

In the final part of the thesis, the localization of the electron as a result of the interference of two molecular states with different symmetries leading to the same final state (same electron energy and KER) is presented. The asymmetry in the localization of the electron with respect to the molecular frame of reference was observed for the first time in both H_2 and D_2 . Using a semi-classical simulation based on the WKB approximation the observed effects were well simulated. And finally, it was shown that, the localization of the electron varies as a function of the delay between two pulses. In the future, one can try to obtain sideband phases for the asymmetry by plotting a so-called asymmetry RABBIT, where instead of event counts, the asymmetry parameter is plotted for a specific KER region.

Appendices

Appendix A

Atomic Units

For simplicity in atomic physics dimensions are expressed in atomic units, one can set all the constants in the electronic Schrödinger Equation equal to one atomic unit.

$$\hbar = m_e = e = 4\pi\epsilon_0 = 1a.u \quad (\text{A.1})$$

The atomic units correspond to the electron in the ground state of the Hydrogen atom. Other quantities can be calculated with the above definition:

Quantity	Definition	SI Value
Time	$a_0(\alpha c)^{-1}$	$2.41888433 \times 10^{-17} \text{s}$
Energy	$m_e(\alpha c)^2$	$44.3593 \times 10^{-34} \text{ J}$
Mass	m_e	$9.1093897 \times 10^{-31} \text{ kg}$
Charge	e	$1.6021773 \times 10^{-19} \text{ C}$
Length	Bohr Radius a_0	$5.29177249 \times 10^{-11} \text{ m}$
Momentum	p	$1.9929 \cdot 10^{-24} \text{ Kg m/s}$
Angular Momentum	\hbar	$1.0545887 \times 10^{-34} \text{ Js}$
Velocity	αc	$2.18769142 \times 10^8 \text{ m/s}$

Appendix B

H_2^+ and D_2^+ spectroscopic values

Quantity	Symbol	Value		Unit
		H_2^+	D_2^+	
reduced mass	μ	0.504	1.007	amu*
vibrational frequency	ω_e	4401.2	3115.5	cm ⁻¹
anharmonic constant	$\omega_e x_e$	66.2		cm ⁻¹
rotational constant	B_e	30.2	15.02	cm ⁻¹
centrifugal distortion constant	α_e	1.68	0.56	cm ⁻¹

* 1 atomic mass unit (amu) = 1.6605×10^{-27} kg.

Energies of vibrational levels:

$$E(v) = \omega_e \left(v + \frac{1}{2} \right) - \omega_e x_e \left(v + \frac{1}{2} \right)^2 + \dots \quad (\text{B.1})$$

Energies of rotational levels:

$$F(J) = B_v J(J+1) - \dots$$

$$B_v = B_e + \alpha_e \left(v + \frac{1}{2} \right) + \dots \quad (\text{B.2})$$

Table B.1: Eigenenergies and relative populations of vibrational states of H_2^+

vibrational level	energy [eV] [*]	population ^{**}
0	-2.646	0.119
1	-2.375	0.190
2	-2.119	0.188
3	-1.878	0.152
4	-1.652	0.111
5	-1.441	0.077
6	-1.244	0.053
7	-1.060	0.036
8	-0.891	0.024
9	-0.735	0.016
10	-0.593	0.011
11	-0.465	0.008
12	-0.351	0.005
13	-0.252	0.004
14	-0.168	0.003
15	-0.100	0.002
16	-0.049	0.001

^{*} Values taken from Cohen et al [149].

^{**} Values taken from von Busch and Dunn [150].

Table B.2: Eigenenergies and relative populations of vibrational states of D_2^+

vibrational level	energy [eV]	population
0	-2.687	0.045
1	-2.491	0.104
2	-2.304	0.141
3	-2.124	0.148
4	-1.952	0.134
5	-1.788	0.111
6	-1.630	0.086
7	-1.480	0.065
8	-1.337	0.047
9	-1.201	0.034
10	-1.072	0.024
11	-0.950	0.017
12	-0.835	0.012
13	-0.727	0.009
14	-0.625	0.006
15	-0.530	0.005
16	-0.444	0.003
17	-0.363	0.003
18	-0.290	0.002
19	-0.225	0.001
20	-0.167	0.001

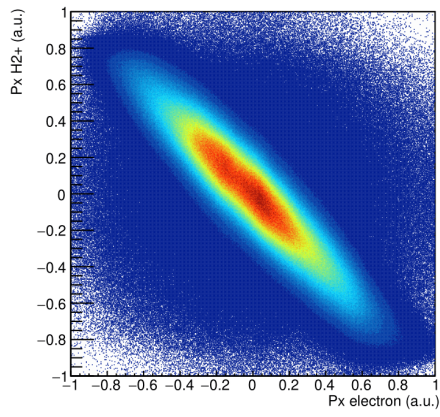
* Values taken from Dunn [118].

** Values taken from von Busch and Dunn [150].

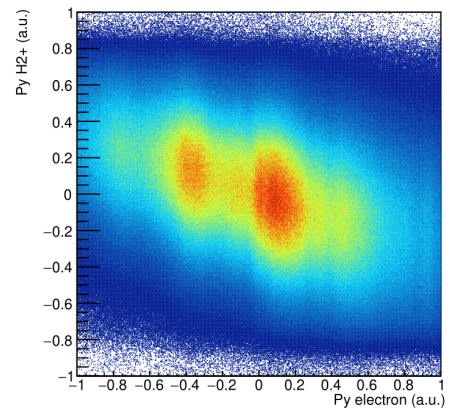
Appendix C

Raw data

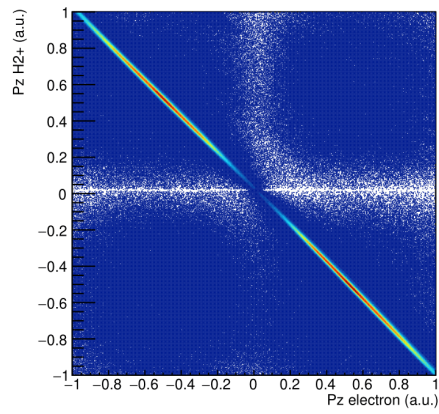
An example of a H₂ measurement is shown in the following figures.



(a)



(b)



(c)

Figure C.1: Momentum sum plots in $H_2^+ + e$ coincidence.

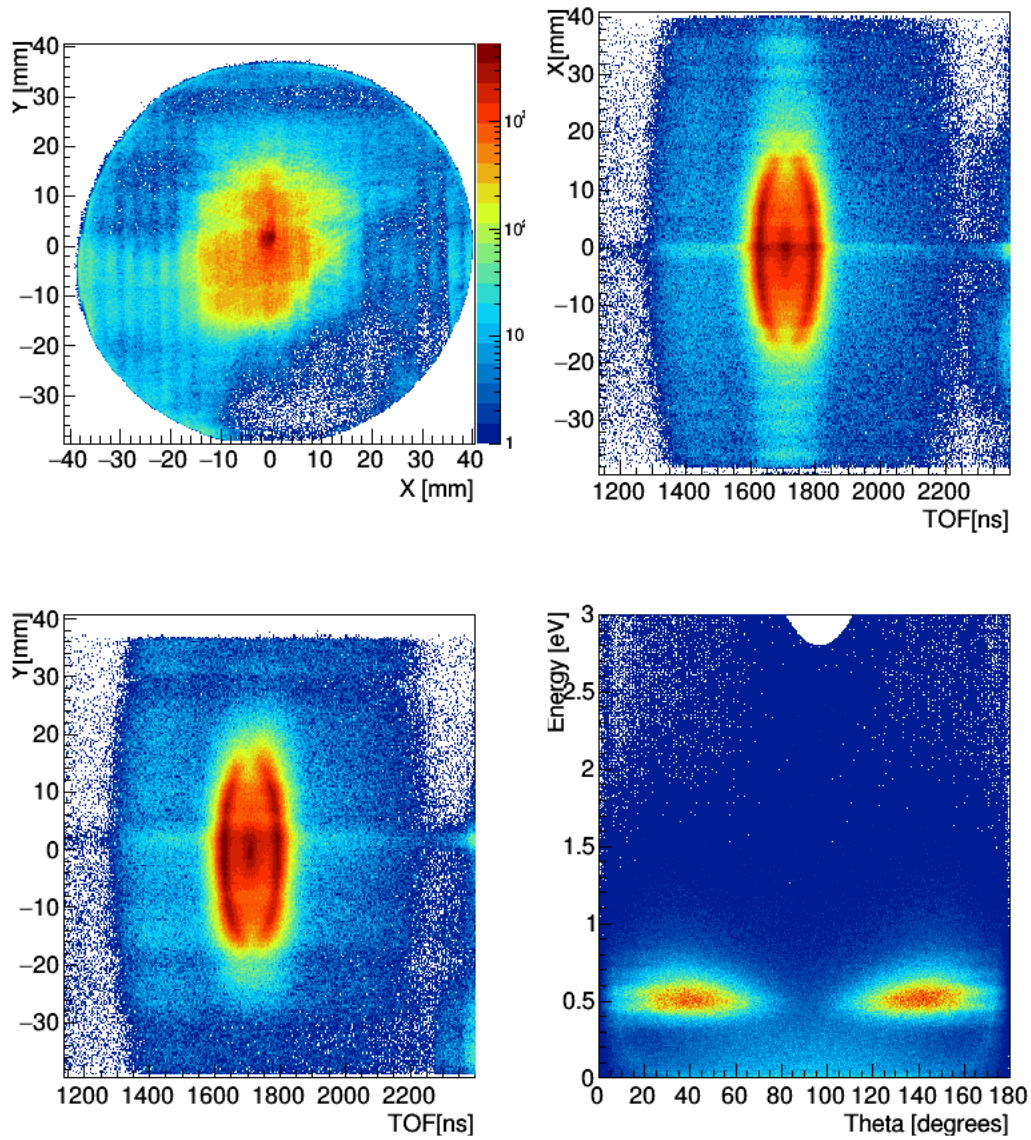


Figure C.2: Upper left: ion detector with a time of flight condition on H^+ . The TOF spectrum as a function of the detector position in upper right and lower left in y and x directions, respectively.

Appendix D

Fit procedure and Error bars

Since the sidebands oscillate with a sinusoidal function, a fit function of the form $A \cos(2\omega - \phi) + B$ is used with three fit parameters A , B , and ϕ . The frequency ω is determined once by fitting the same function with ω as a parameter. Once known, the frequency is fixed for the whole measurement. The fit uses the least squared method and error bars presented in the entire work is the standard error given by the fit.

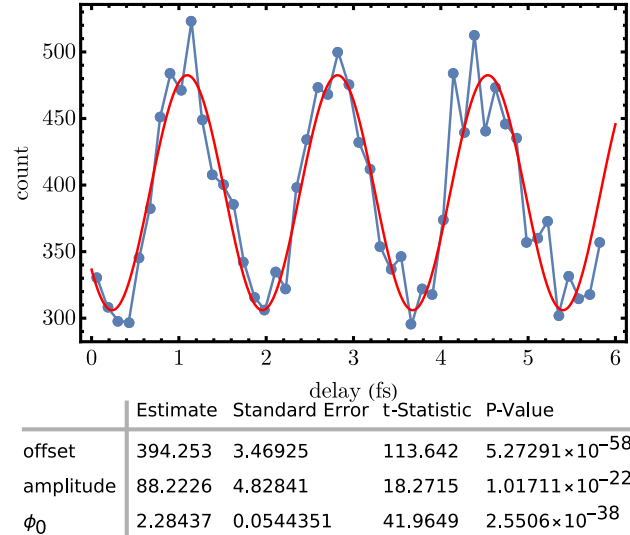


Figure D.1: Upper panel: a sinusoidal fit to the experimental data. Lower panel: the corresponding fit parameters with errors.

Appendix E

Toroidal mirror

The toroidal mirror used in the setup with a 2f-2f configuration and a quartz glass substrate with a length of 150 mm and a width of 30 mm. The coating material is B_4C with a thickness of 30 nm. The angle of incidence is 8 degrees. The reflection curves for both XUV and IR light is given in Fig. E.

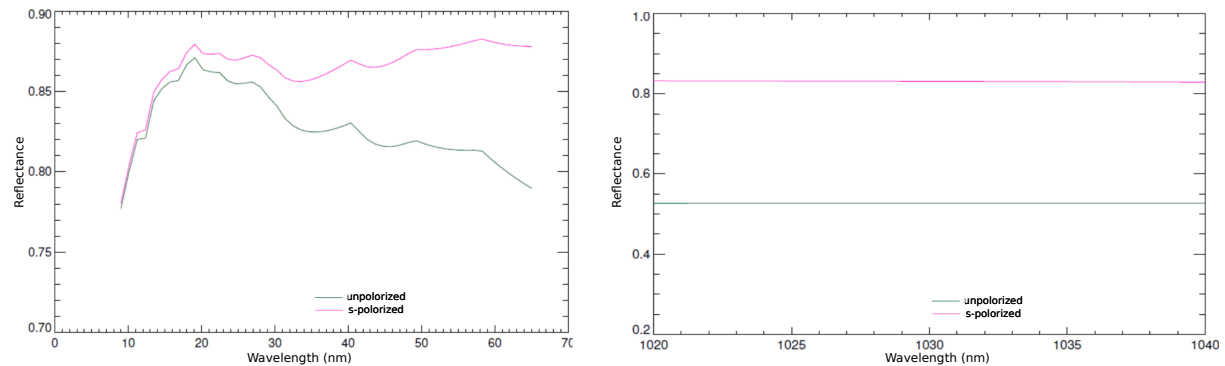


Figure E.1: Reflectance of the toroidal mirror as a function of wavelength.

Appendix F

Bandwidth of Doubly-excited states

In this chapter the bandwidth of the relevant doubly-excited states as a function of the internuclear distance is shown. All figures are taken from [133] and [151].

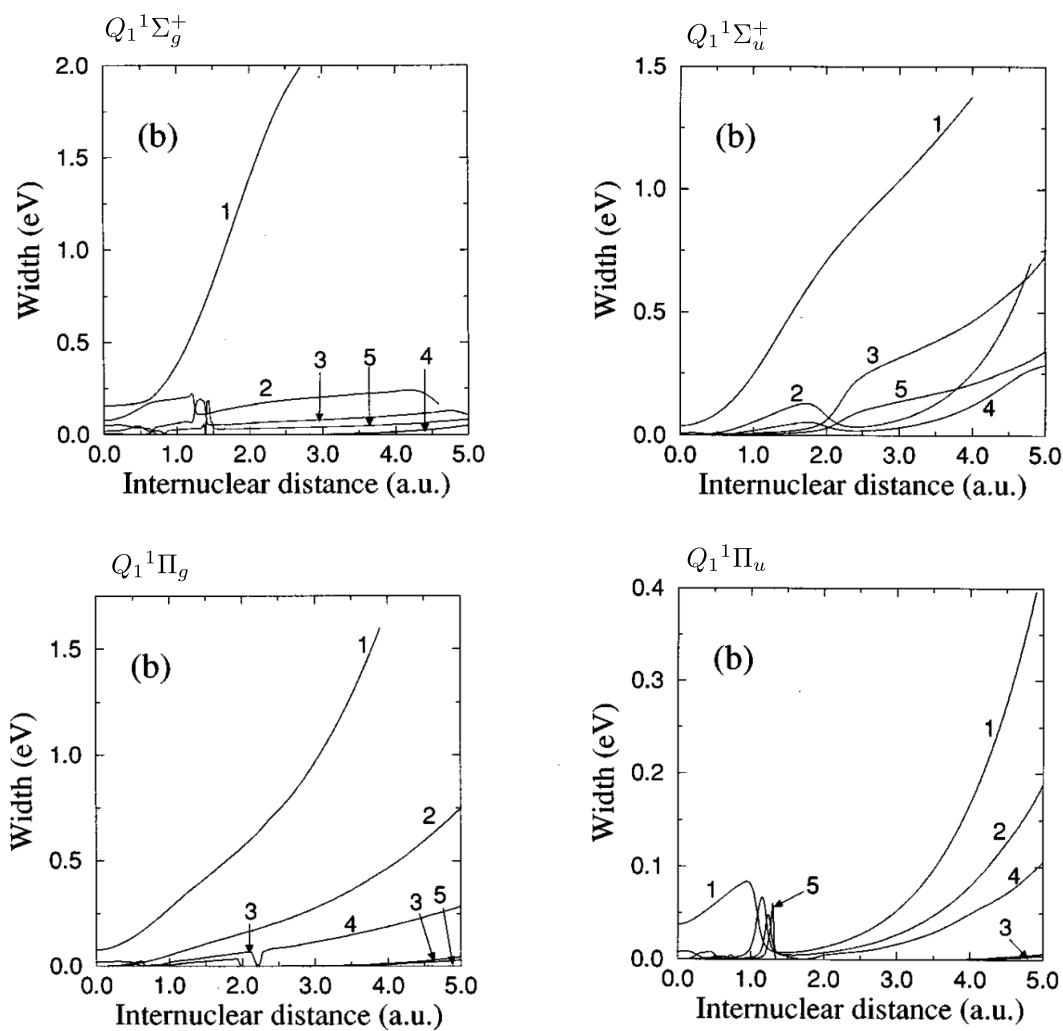


Figure F.1: Autoionization width of the five lowest states of Q_1 with different symmetries in H_2 .

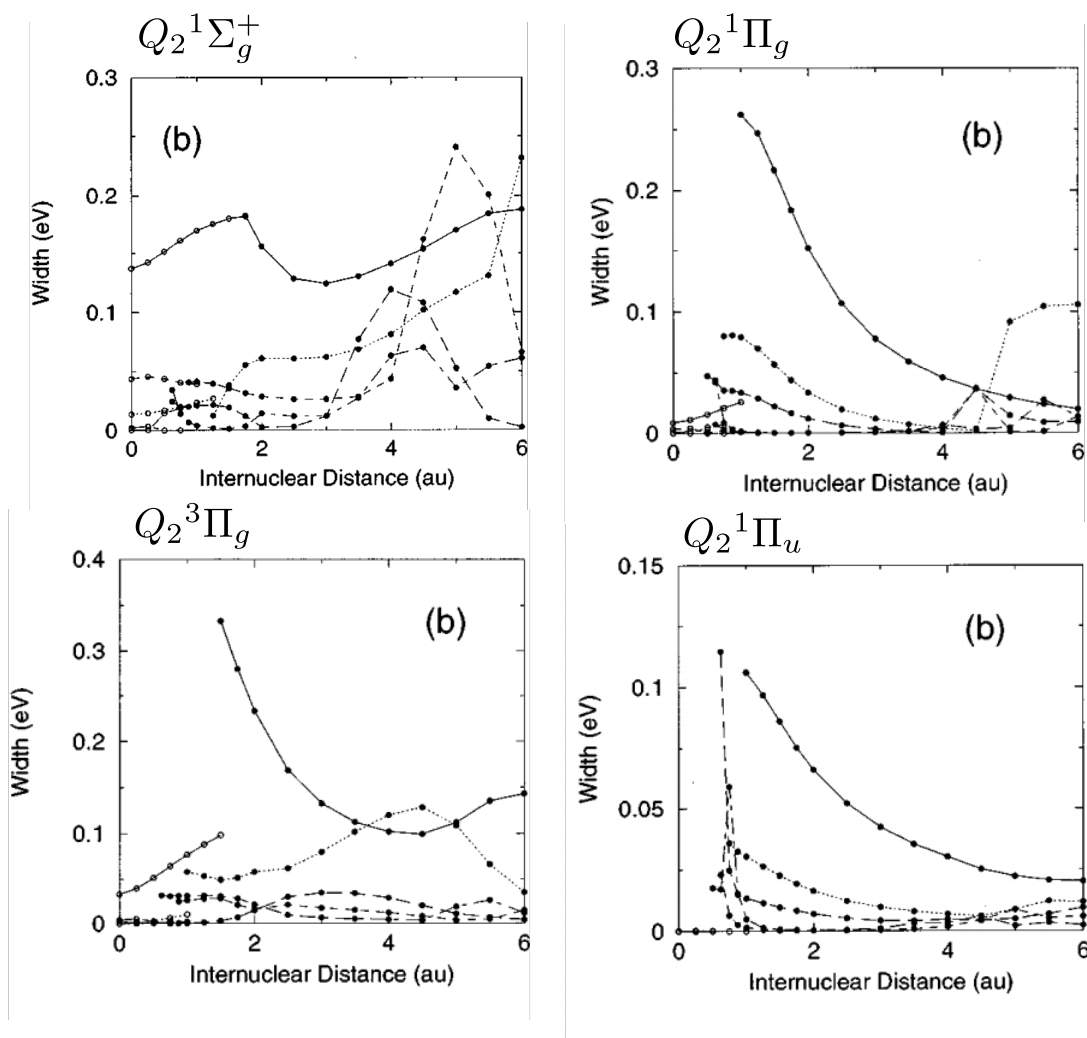


Figure F.2: Autoionization width of the five lowest states of Q_2 with different symmetries in H_2 . Full line: first state; dotted line: second state; short-dashed line: third state; long-dashed line: fourth state; chain line: fifth state.

Bibliography

- [1] Albert Stolow, Arthur E. Bragg, and Daniel M. Neumark. Femtosecond time-resolved photoelectron spectroscopy. *Chemical Reviews*, 104(4):1719–1758, 2004. PMID: 15080710. [1](#)
- [2] Ahmed H. Zewail. Laser femtochemistry. *Science*, 242(4886):1645–1653, 1988. [1](#)
- [3] Ahmed H. Zewail. *Femtochemistry*, pages 3–22. [1](#)
- [4] E. D. Potter, J. L. Herek, S. Pedersen, Q. Liu, and A. H. Zewail. Femtosecond laser control of a chemical reaction. *Nature*, 355(6355):66–68, Jan 1992. [1](#)
- [5] Alicia Palacios and Fernando Martín. The quantum chemistry of attosecond molecular science. *WIREs Computational Molecular Science*, 10(1):e1430, 2020. [1](#)
- [6] P. M. Paul, E. S. Toma, P. Breger, G. Mullot, F. Augé, Ph. Balcou, H. G. Muller, and P. Agostini. Observation of a train of attosecond pulses from high harmonic generation. *Science*, 292(5522):1689–1692, 2001. [1](#), [3](#), [12](#), [15](#)
- [7] M. F. Kling, Ch. Siedschlag, A. J. Verhoef, J. I. Khan, M. Schultze, Th. Uphues, Y. Ni, M. Uiberacker, M. Drescher, F. Krausz, and M. J. J. Vrakking. Control of electron localization in molecular dissociation. *Science*, 312(5771):246–248, 2006. [1](#), [3](#), [105](#)
- [8] G. Sansone, F. Kelkensberg, J. F. Pérez-Torres, F. Morales, M. F. Kling, W. Siu, O. Ghafur, P. Johnsson, M. Swoboda, E. Benedetti, F. Ferrari, F. Lépine, J. L. Sanz-Vicario, S. Zherebtsov, I. Znakovskaya, A. L’Huillier, M. Yu. Ivanov, M. Nisoli, F. Martín, and M. J. J. Vrakking. Electron localization following attosecond molecular photoionization. *Nature*, 465(7299):763–766, Jun 2010. [1](#), [3](#), [105](#)
- [9] Jan Rothhardt, Steffen Hädrich, Henning Carstens, Nicholas Herrick, Stefan Demmler, Jens Limpert, and Andreas Tünnermann. 1 mhz repetition rate hollow fiber pulse compression to sub-100-fs duration at 100 w average power. *Opt. Lett.*, 36(23):4605–4607, Dec 2011. [1](#)
- [10] Isao Matsushima, Hidehiko Yashiro, and Toshihisa Tomie. 10 khz 40 w ti:sapphire regenerative ring amplifier. *Opt. Lett.*, 31(13):2066–2068, Jul 2006. [1](#)

- [11] Clara J. Saraceno, Florian Emaury, Oliver H. Heckl, Cyrill R. E. Baer, Martin Hoffmann, Cinia Schriber, Matthias Golling, Thomas Südmeyer, and Ursula Keller. 275 w average output power from a femtosecond thin disk oscillator operated in a vacuum environment. *Opt. Express*, 20(21):23535–23541, Oct 2012. [1](#)
- [12] Tino Eidam, Stefan Hanf, Enrico Seise, Thomas V. Andersen, Thomas Gabler, Christian Wirth, Thomas Schreiber, Jens Limpert, and Andreas Tünnermann. Femtosecond fiber CPA system emitting 830 w average output power. *Opt. Lett.*, 35(2):94–96, Jan 2010. [1](#)
- [13] J Ullrich, R Moshhammer, A Dorn, R Dörner, L Ph H Schmidt, and H Schmidt-Böcking. Recoil-ion and electron momentum spectroscopy reaction-microscopes. *Reports on Progress in Physics*, 66(9):1463, 2003. [1](#)
- [14] R. Moshhammer, M. Unverzagt, W. Schmitt, J. Ullrich, and H. Schmidt-Böcking. A 4pi recoil-ion electron momentum analyzer: a high-resolution “microscope” for the investigation of the dynamics of atomic, molecular and nuclear reactions. *Nuclear Instruments and Methods in Physics Research Section B: Beam Interactions with Materials and Atoms*, 108(4):425 – 445, 1996. [1](#)
- [15] Heide Ibrahim, Catherine Lefebvre, André D Bandrauk, André Staudte, and François Légaré. H₂: the benchmark molecule for ultrafast science and technologies. *Journal of Physics B: Atomic, Molecular and Optical Physics*, 51(4):042002, Jan 2018. [2](#), [105](#)
- [16] H Li, X Gong, K Lin, R de Vivie-Riedle, X M Tong, J Wu, and M F Kling. Sub-cycle directional control of the dissociative ionization of H₂ in tailored femtosecond laser fields. *Journal of Physics B: Atomic, Molecular and Optical Physics*, 50(17):172001, Aug 2017. [2](#), [3](#)
- [17] Joseph M. Ajello, Isik Kanik, Syed M. Ahmed, and John T. Clarke. Line profile of H Lyman alpha from dissociative excitation of H₂ with application to Jupiter. *Journal of Geophysical Research: Planets*, 100(E12):26411–26420, 1995. [2](#)
- [18] Abigail Dobbyn, David Mordaunt, and Reinhard Schinke. *Molecular Photodissociation*, pages 535–546. Springer New York, New York, NY, 2006. [2](#)
- [19] F. Martin, J. Fernandez, T. Havermeier, L. Foucar, Th. Weber, K. Kreidi, M. Schoeffler, L. Schmidt, T. Jahnke, O. Jagutzki, A. Czasch, E. P. Benis, T. Osipov, A. L. Landers, A. Belkacem, M. H. Prior, H. Schmidt-Böcking, C. L. Cocke, and R. Dörner. Single photon-induced symmetry breaking of H₂ dissociation. *Science*, 315(5812):629–633, 2007. [2](#), [70](#), [89](#)
- [20] Ferenc Krausz and Misha Ivanov. Attosecond physics. *Rev. Mod. Phys.*, 81:163–234, Feb 2009. [2](#)
- [21] A. D. Bandrauk. *Molecules in Laser Fields*, pages 131–150. Springer Netherlands, Dordrecht, 1995. [3](#), [72](#)

- [22] B. Sheehy and L. F. DiMauro. Atomic and molecular dynamics in intense optical fields. *Annual Review of Physical Chemistry*, 47(1):463–494, 1996. [3](#)
- [23] J H Posthumus. The dynamics of small molecules in intense laser fields. *Reports on Progress in Physics*, 67(5):623–665, apr 2004. [3](#)
- [24] Rodrigo López-Martens, Katalin Varjú, Per Johnsson, Johan Mauritsson, Yann Mairesse, Pascal Salières, Mette B. Gaarde, Kenneth J. Schafer, Anders Persson, Sune Svanberg, Claes-Göran Wahlström, and Anne L’Huillier. Amplitude and phase control of attosecond light pulses. *Phys. Rev. Lett.*, 94:033001, Jan 2005. [3](#)
- [25] H.G. Muller. Reconstruction of attosecond harmonic beating by interference of two-photon transitions. *Applied Physics B*, 74(1):s17–s21, 2002. [3](#)
- [26] K. Klünder, J. M. Dahlström, M. Gisselbrecht, T. Fordell, M. Swoboda, D. Guénot, P. Johnsson, J. Caillat, J. Mauritsson, A. Maquet, R. Taïeb, and A. L’Huillier. Probing single-photon ionization on the attosecond time scale. *Phys. Rev. Lett.*, 106:143002, Apr 2011. [3](#), [12](#), [14](#), [78](#)
- [27] D. Guénot, K. Klünder, C. L. Arnold, D. Kroon, J. M. Dahlström, M. Miranda, T. Fordell, M. Gisselbrecht, P. Johnsson, J. Mauritsson, E. Lindroth, A. Maquet, R. Taïeb, A. L’Huillier, and A. S. Kheifets. Photoemission-time-delay measurements and calculations close to the $3s$ -ionization-cross-section minimum in ar. *Phys. Rev. A*, 85:053424, May 2012. [3](#), [12](#)
- [28] D Busto, L Barreau, M Isinger, M Turconi, C Alexandridi, A Harth, S Zhong, R J Squibb, D Kroon, S Plogmaker, M Miranda, Á Jiménez-Galán, L Argenti, C L Arnold, R Feifel, F Martín, M Gisselbrecht, A L’Huillier, and P Salières. Time–frequency representation of autoionization dynamics in helium. *Journal of Physics B: Atomic, Molecular and Optical Physics*, 51(4):044002, jan 2018. [3](#)
- [29] Claudio Cirelli, Carlos Marante, Sebastian Heuser, C. L. M. Petersson, Álvaro Jiménez Galán, Luca Argenti, Shiyang Zhong, David Busto, Marcus Isinger, Saikat Nandi, Sylvain Maclot, Linnea Rading, Per Johnsson, Mathieu Gisselbrecht, Matteo Lucchini, Lukas Gallmann, J. Marcus Dahlström, Eva Lindroth, Anne L’Huillier, Fernando Martín, and Ursula Keller. Anisotropic photoemission time delays close to a fano resonance. *Nature Communications*, 9(1):955, Mar 2018. [3](#)
- [30] Martin Huppert, Inga Jordan, Denitsa Baykusheva, Aaron von Conta, and Hans Jakob Wörner. Attosecond delays in molecular photoionization. *Phys. Rev. Lett.*, 117:093001, Aug 2016. [3](#), [79](#)
- [31] S. Nandi, E. Plésiat, S. Zhong, A. Palacios, D. Busto, M. Isinger, L. Neoričić, C. L. Arnold, R. J. Squibb, R. Feifel, P. Decleva, A. L’Huillier, F. Martín, and M. Gisselbrecht. Attosecond timing of electron emission from a molecular shape resonance. *Science Advances*, 6(31), 2020. [3](#), [79](#)

- [32] Andrei Kamalov, Anna L. Wang, Philip H. Bucksbaum, Daniel J. Haxton, and James P. Cryan. Electron correlation effects in attosecond photoionization of CO_2 . *Phys. Rev. A*, 102:023118, Aug 2020. [3](#), [79](#)
- [33] J. Vos, L. Cattaneo, S. Patchkovskii, T. Zimmermann, C. Cirelli, M. Lucchini, A. Kheifets, A. S. Landsman, and U. Keller. Orientation-dependent stereo wigner time delay and electron localization in a small molecule. *Science*, 360(6395):1326–1330, 2018. [3](#), [79](#)
- [34] L. Cattaneo, J. Vos, R. Y. Bello, A. Palacios, S. Heuser, L. Pedrelli, M. Lucchini, C. Cirelli, F. Martín, and U. Keller. Attosecond coupled electron and nuclear dynamics in dissociative ionization of H_2 . *Nature Physics*, 14(7):733–738, Jul 2018. [3](#), [79](#), [82](#)
- [35] Alejandro Saenz. Molecular hydrogen in strong laser fields: Bond softening, enhanced ionisation, and coherent control. *Physica Scripta*, 110:126, 2004. [3](#)
- [36] Ali S Alnaser and Igor V Litvinyuk. Subfemtosecond directional control of chemical processes in molecules. *Journal of Physics B: Atomic, Molecular and Optical Physics*, 50(3):032002, jan 2017. [3](#)
- [37] Gerard A. Mourou, Toshiki Tajima, and Sergei V. Bulanov. Optics in the relativistic regime. *Rev. Mod. Phys.*, 78:309–371, Apr 2006. [1](#)
- [38] Uwe Morgner. *Ultrafast Laser Oscillators and Amplifiers*, pages 17–36. 2014.
- [39] Roger Y. Bello, Sophie E. Canton, Denis Jelovina, John D. Bozek, Bruce Rude, Olga Smirnova, Mikhail Y. Ivanov, Alicia Palacios, and Fernando Martín. Reconstruction of the time-dependent electronic wave packet arising from molecular autoionization. *Science Advances*, 4(8), 2018.
- [40] James A. R. Samson and G. N. Haddad. Total photoabsorption cross sections of H_2 from 18 to 113 eV. *J. Opt. Soc. Am. B*, 11(2):277–279, Feb 1994.
- [41] S.K. Semenov and N.A. Cherepkov. Generalization of the atomic rpa method for diatomic molecules: H_2 photoionization cross-section calculation. *Chemical Physics Letters*, 291(3):375 – 380, 1998.
- [42] I. Sánchez and F. Martín. Resonant effects in photoionization of H_2 and D_2 . *The Journal of Chemical Physics*, 107(20):8391–8396, 1997. [66](#), [70](#), [71](#)
- [43] Alicia Palacios, José Luis Sanz-Vicario, and Fernando Martín. Theoretical methods for attosecond electron and nuclear dynamics: applications to the H_2 molecule. *Journal of Physics B: Atomic, Molecular and Optical Physics*, 48(24):242001, oct 2015. [52](#)
- [44] L’Huillier, Anne. Atoms in strong laser fields. *Europhysics News*, 33(6):205–207, 2002. [5](#)

- [45] A. McPherson, G. Gibson, H. Jara, U. Johann, T. S. Luk, I. A. McIntyre, K. Boyer, and C. K. Rhodes. Studies of multiphoton production of vacuum-ultraviolet radiation in the rare gases. *J. Opt. Soc. Am. B*, 4(4):595–601, Apr 1987. 6
- [46] M Ferray, A L’Huillier, X F Li, L A Lompre, G Mainfray, and C Manus. Multiple-harmonic conversion of 1064 nm radiation in rare gases. *Journal of Physics B: Atomic, Molecular and Optical Physics*, 21(3):L31–L35, feb 1988. 6
- [47] M Lewenstein, P Balcou, M Y Ivanov, A L’Huillier, and Corkum. Theory of high-harmonic generation by low-frequency laser fields. *Physical Review A*, 49(3), 3 1994. 6
- [48] P. B. Corkum. Plasma perspective on strong field multiphoton ionization. *Phys. Rev. Lett.*, 71:1994–1997, Sep 1993. 6
- [49] K. J. Schafer, Baorui Yang, L. F. DiMauro, and K. C. Kulander. Above threshold ionization beyond the high harmonic cutoff. *Phys. Rev. Lett.*, 70:1599–1602, Mar 1993. 6
- [50] Tenio Popmintchev, Ming-Chang Chen, Paul Arpin, Margaret M. Murnane, and Henry C. Kapteyn. The attosecond nonlinear optics of bright coherent x-ray generation. *Nat Photon*, 4(12):822–832, Dec 2010. 7
- [51] K Burnett, V C Reed, and P L Knight. Atoms in ultra-intense laser fields. *Journal of Physics B: Atomic, Molecular and Optical Physics*, 26(4):561–598, feb 1993. 7
- [52] P. H. Bucksbaum, R. R. Freeman, M. Bashkansky, and T. J. McIlrath. Role of the ponderomotive potential in above-threshold ionization. *J. Opt. Soc. Am. B*, 4(5):760–764, May 1987. 7
- [53] K. Varjú ||, Y. Mairesse, B. Carré, M. B. Gaarde, P. Johnsson, S. Kazamias, R. López-Martens, J. Mauritsson, K. J. Schafer, PH. Balcou, A. L’huillier, and P. Salières. Frequency chirp of harmonic and attosecond pulses. *Journal of Modern Optics*, 52(2-3):379–394, 2005. 8
- [54] C M Heyl, J GÜdde, A L’Huillier, and U Höfer. High-order harmonic generation with microj laser pulses at high repetition rates. *Journal of Physics B: Atomic, Molecular and Optical Physics*, 45(7):074020, mar 2012. 9
- [55] C. M. Heyl, H. Coudert-Alteirac, M. Miranda, M. Louisy, K. Kovacs, V. Tosa, E. Balogh, K. Varjú, A. L’Huillier, A. Couairon, and C. L. Arnold. Scale-invariant nonlinear optics in gases. *Optica*, 3(1):75–81, Jan 2016. 9
- [56] C M Heyl, C L Arnold, A Couairon, and A L’Huillier. Introduction to macroscopic power scaling principles for high-order harmonic generation. *Journal of Physics B: Atomic, Molecular and Optical Physics*, 50(1):013001, dec 2016. 9
- [57] Ph. Balcou and Anne L’Huillier. Phase-matching effects in strong-field harmonic generation. *Phys. Rev. A*, 47:1447–1459, Feb 1993. 9

- [58] Valérie Vénier, Richard Taïeb, and Alfred Maquet. Phase dependence of $(n+1)$ -color ($n>1$) ir-uv photoionization of atoms with higher harmonics. *Phys. Rev. A*, 54:721–728, Jul 1996. [12](#)
- [59] H.G. Muller. Reconstruction of attosecond harmonic beating by interference of two-photon transitions. *Applied Physics B*, 74(1):s17–s21, 2002. [12](#)
- [60] Erik P. Månsson, Diego Guénot, Cord L. Arnold, David Kroon, Susan Kasper, J. Marcus Dahlström, Eva Lindroth, Anatoli S. Kheifets, Anne L’Huillier, Stacey L. Sorensen, and Mathieu Gisselbrecht. Double ionization probed on the attosecond timescale. *Nature Physics*, 10(3):207–211, Mar 2014. [12](#)
- [61] J.M. Dahlström, D. Guénot, K. Klünder, M. Gisselbrecht, J. Mauritsson, A. L’Huillier, A. Maquet, and R. Taïeb. Theory of attosecond delays in laser-assisted photoionization. *Chemical Physics*, 414:53 – 64, 2013. Attosecond spectroscopy. [12](#), [14](#), [99](#)
- [62] J M Dahlström, A L’Huillier, and A Maquet. Introduction to attosecond delays in photoionization. *Journal of Physics B: Atomic, Molecular and Optical Physics*, 45(18):183001, 2012. [12](#), [78](#), [99](#)
- [63] M. Isinger, D. Busto, S. Mikaelsson, S. Zhong, C. Guo, P. Salières, C. L. Arnold, A. L’Huillier, and M. Gisselbrecht. Accuracy and precision of the rabbit technique. *Philosophical Transactions of the Royal Society A: Mathematical, Physical and Engineering Sciences*, 377(2145):20170475, 2019. [13](#)
- [64] Johan Mauritsson, Mette B. Gaarde, and Kenneth J. Schafer. Accessing properties of electron wave packets generated by attosecond pulse trains through time-dependent calculations. *Phys. Rev. A*, 72:013401, Jul 2005. [14](#)
- [65] Alfred Maquet, Jérémie Caillat, and Richard Taïeb. Attosecond delays in photoionization: time and quantum mechanics. *Journal of Physics B: Atomic, Molecular and Optical Physics*, 47(20):204004, oct 2014. [14](#)
- [66] M. Swoboda, T. Fordell, K. Klünder, J. M. Dahlström, M. Miranda, C. Buth, K. J. Schafer, J. Mauritsson, A. L’Huillier, and M. Gisselbrecht. Phase measurement of resonant two-photon ionization in helium. *Phys. Rev. Lett.*, 104:103003, Mar 2010. [14](#)
- [67] M. Kotur, D. Guénot, Á Jiménez-Galán, D. Kroon, E. W. Larsen, M. Louisy, S. Bengtsson, M. Miranda, J. Mauritsson, C. L. Arnold, S. E. Canton, M. Gisselbrecht, T. Carette, J. M. Dahlström, E. Lindroth, A. Maquet, L. Argenti, F. Martín, and A. L’Huillier. Spectral phase measurement of a fano resonance using tunable attosecond pulses. *Nature Communications*, 7(1):10566, Feb 2016. [14](#)
- [68] S. Haessler, B. Fabre, J. Higuier, J. Caillat, T. Ruchon, P. Breger, B. Carré, E. Constant, A. Maquet, E. Mével, P. Salières, R. Taïeb, and Y. Mairesse. Phase-resolved

- attosecond near-threshold photoionization of molecular nitrogen. *Phys. Rev. A*, 80:011404, Jul 2009. [14](#), [78](#)
- [69] Jérémie Caillat, Alfred Maquet, Stefan Haessler, Baptiste Fabre, Thierry Ruchon, Pascal Salières, Yann Mairesse, and Richard Taïeb. Attosecond resolved electron release in two-color near-threshold photoionization of n_2 . *Phys. Rev. Lett.*, 106:093002, Mar 2011. [14](#)
- [70] Ugo Fano and L. Fano. *Basic Physics of Atoms and Molecules* -. Wiley, New York, 1969.
- [71] Friedrich Engelke. *Aufbau der Moleküle - Eine einföhrung*. Springer-Verlag, Berlin Heidelberg New York, 2013.
- [72] M. Karplus and R. Porter. *Atoms and Molecules: An Introduction for Students of Physical Chemistry*. Benjamin-Cummings Pub Co, 1970. JILA Pub. 705.
- [73] M. Born and R. Oppenheimer. Zur quantentheorie der molekeln. *Annalen der Physik*, 389(20):457–484, 1927. [17](#)
- [74] I.V. Hertel and C.P. Schulz. *Atome, Moleküle und optische Physik 2: Moleküle und Photonen - Spektroskopie und Streuphysik*. Springer-Lehrbuch. Springer Berlin Heidelberg, 2010. [17](#)
- [75] W. Demtröder. *Atoms, Molecules and Photons: An Introduction to Atomic-, Molecular- and Quantum Physics*. Graduate Texts in Physics. Springer Berlin Heidelberg, 2010. [17](#)
- [76] T.E. Sharp. Potential-energy curves for molecular hydrogen and its ions. *Atomic Data and Nuclear Data Tables*, 2:119 – 169, 1970. [18](#), [54](#), [60](#)
- [77] M. Weissbluth. *Atoms and Molecules*. Academic Press, 1978. [20](#)
- [78] Anthony Starace. *Photoionization of Atoms*, pages 379–390. Springer New York, New York, NY, 2006. [20](#)
- [79] D. Willock. *Molecular Symmetry*. Wiley, 2009. [20](#)
- [80] P.W. Atkins and R.S. Friedman. *Molecular Quantum Mechanics*. OUP Oxford, 2011. [20](#)
- [81] H. Haken, H.C. Wolf, and W.D. Brewer. *Molecular Physics and Elements of Quantum Chemistry: Introduction to Experiments and Theory*. Advanced Texts in Physics. Springer, 2004. [20](#)
- [82] D.C. Harris and M.D. Bertolucci. *Symmetry and Spectroscopy: An Introduction to Vibrational and Electronic Spectroscopy*. Dover Books on Chemistry Series. Dover Publications, 1989. [22](#)

- [83] John Michael Hollas. *Symmetry in molecules*. CRC Press, 1972. [22](#)
- [84] Roger Grinter. *The Quantum in Chemistry: An Experimentalist's View*. Wiley, 2005. [24](#)
- [85] Shih-I Chu. Floquet theory and complex quasivibrational energy formalism for intense field molecular photodissociation. *The Journal of Chemical Physics*, 75(5):2215–2221, 1981. [26](#)
- [86] Shih-I Chu and Dmitry A. Telnov. Beyond the floquet theorem: generalized floquet formalisms and quasienergy methods for atomic and molecular multiphoton processes in intense laser fields. *Physics Reports*, 390(1):1 – 131, 2004. [26](#)
- [87] Philipp V. Demekhin and Lorenz S. Cederbaum. Light-induced conical intersections in polyatomic molecules: General theory, strategies of exploitation, and application. *The Journal of Chemical Physics*, 139(15):154314, 2013. [26](#)
- [88] Nimrod Moiseyev, Milan Šindelka, and Lorenz S Cederbaum. Laser-induced conical intersections in molecular optical lattices. *Journal of Physics B: Atomic, Molecular and Optical Physics*, 41(22):221001, nov 2008. [26](#)
- [89] L. D. LANDAU. Zur theorie der energieubertragung ii. *Z. Sowjetunion*, 2:46–51, 1932. [27](#)
- [90] Clarence Zener and Ralph Howard Fowler. Non-adiabatic crossing of energy levels. *Proceedings of the Royal Society of London. Series A, Containing Papers of a Mathematical and Physical Character*, 137(833):696–702, 1932. [27](#)
- [91] Nimrod Moiseyev. Quantum theory of resonances: calculating energies, widths and cross-sections by complex scaling. *Physics Reports*, 302(5):212 – 293, 1998.
- [92] Bettina Fischer. *Time resolved studies of H₂ dissociation with phase-stabilized laser pulses*. PhD thesis, 2010. [28](#)
- [93] M.V. Fedorov, O.V. Kudrevatova, V.P. Makarov, and A.A. Samokhin. On the separation of electronic and nuclear motion for molecules in an intense electromagnetic wave. *Optics Communications*, 13(3):299 – 302, 1975.
- [94] P. H. Bucksbaum, A. Zavriyev, H. G. Muller, and D. W. Schumacher. Softening of the h₂⁺ molecular bond in intense laser fields. *Phys. Rev. Lett.*, 64:1883–1886, Apr 1990. [27](#)
- [95] A. Zavriyev, P. H. Bucksbaum, H. G. Muller, and D. W. Schumacher. Ionization and dissociation of h₂ in intense laser fields at 1.064 μm, 532 nm, and 355 nm. *Phys. Rev. A*, 42:5500–5513, Nov 1990. [27](#)
- [96] G. Jolicard and O. Atabek. Above-threshold-dissociation dynamics of h₂⁺ with short intense laser pulses. *Phys. Rev. A*, 46:5845–5855, Nov 1992. [27](#)

- [97] A. Giusti-Suzor, X. He, O. Atabek, and F. H. Mies. Above-threshold dissociation of h_2^+ in intense laser fields. *Phys. Rev. Lett.*, 64:515–518, Jan 1990. [27](#)
- [98] Guanhua Yao and Shih-I Chu. Molecular-bond hardening and dynamics of molecular stabilization and trapping in intense laser pulses. *Phys. Rev. A*, 48:485–494, Jul 1993. [27](#)
- [99] A. Giusti-Suzor and F. H. Mies. Vibrational trapping and suppression of dissociation in intense laser fields. *Phys. Rev. Lett.*, 68:3869–3872, Jun 1992. [27](#)
- [100] L. J. Frasinski, J. H. Posthumus, J. Plumridge, K. Codling, P. F. Taday, and A. J. Langley. Manipulation of bond hardening in h_2^+ by chirping of intense femtosecond laser pulses. *Phys. Rev. Lett.*, 83:3625–3628, Nov 1999. [27](#)
- [101] Domagoj Pavicic, Theodor W. Hänsch, and Hartmut . Vibrationally resolved strong-field dissociation of d_2^+ in ion beams. *Phys. Rev. A*, 72:053413, Nov 2005. [27](#), [73](#), [75](#)
- [102] Eric E. Aubanel, Jean-Marc Gauthier, and André D. Bandrauk. Molecular stabilization and angular distribution in photodissociation of h_2^+ in intense laser fields. *Phys. Rev. A*, 48:2145–2152, Sep 1993. [27](#)
- [103] J H Posthumus, J Plumridge, L J Frasinski, K Codling, E J Divall, A J Langley, and P F Taday. Slow protons as a signature of zero-photon dissociation of h_2^+ in intense laser fields. *Journal of Physics B: Atomic, Molecular and Optical Physics*, 33(16):L563–L569, jul 2000. [27](#)
- [104] Patrick Fross. *Electron-nuclear correlation, singly-excited Rydberg states and electron emission asymmetry in multiphoton ionization of H_2* . PhD thesis, 2020. [31](#), [98](#)
- [105] Michael Müller, Marco Kienel, Arno Klenke, Thomas Gottschall, Evgeny Shestaeu, Marco Plötner, Jens Limpert, and Andreas Tünnermann. 1 kw 1 mj eight-channel ultrafast fiber laser. *Opt. Lett.*, 41(15):3439–3442, Aug ts. [33](#), [34](#)
- [106] Steffen Hädrich, Jan Rothhardt, Manuel Krebs, Stefan Demmler, Arno Klenke, Andreas Tünnermann, and Jens Limpert. Single-pass high harmonic generation at high repetition rate and photon flux. *Journal of Physics B: Atomic, Molecular and Optical Physics*, 49(17):172002, aug 2016. [33](#), [39](#)
- [107] G.V. Marr and J.B. West. Absolute photoionization cross-section tables for helium, neon, argon, and krypton in the vuv spectral regions. *Atomic Data and Nuclear Data Tables*, 18(5):497 – 508, 1976. [39](#)
- [108] J Ullrich, R Moshhammer, A Dorn, R Dörner, L Ph H Schmidt, and H Schmidt-Böcking. Recoil-ion and electron momentum spectroscopy: reaction-microscopes. *Reports on Progress in Physics*, 66(9):1463, 2003. [40](#)

- [109] R. Dörner, V. Mergel, O. Jagutzki, L. Spielberger, J. Ullrich, R. Moshammer, and H. Schmidt-Böcking. Cold target recoil ion momentum spectroscopy: a ‘momentum microscope’ to view atomic collision dynamics. *Physics Reports*, 330(2):95 – 192, 2000. [40](#)
- [110] Philipp Cörlin. *Tracing ultra-fast molecular dynamics in O 2 + and N 2 + with XUV-IR pump-probe experiments*. PhD thesis, Heidelberg Univeristy, 2015. [40](#)
- [111] G. Scoles. *Atomic and Molecular Beam Methods*. Number Bd. 1 in Atomic and Molecular Beam Methods. Oxford University Press, 1988. [41](#)
- [112] Ram Gopal. *Electron Wave Packet Interferences in Ionization with Few-Cycle Laser Pulses and the Dissociative Photoionization of D2 with Ultrashort Extreme Ultraviolet Pulses*. PhD thesis, Heidelberg Univeristy, 2010. [43](#)
- [113] Alexander Georg Sperl. *XUV-IR pump-probe experiments: Exploring nuclear and electronic correlated quantum dynamics in the hydrogen molecule*. PhD thesis, Heidelberg Univeristy, 2013. [43](#)
- [114] Joseph Ladislav Wiza. Microchannel plate detectors. *Nuclear Instruments and Methods*, 162(1):587 – 601, 1979. [43](#)
- [115] O Jagutzki, V Mergel, K Ullmann-Pfleger, L Spielberger, U Spillmann, R Dörner, and H Schmidt-Böcking. A broad-application microchannel-plate detector system for advanced particle or photon detection tasks: large area imaging, precise multi-hit timing information and high detection rate. *Nuclear Instruments and Methods in Physics Research Section A: Accelerators, Spectrometers, Detectors and Associated Equipment*, 477(1):244 – 249, 2002. 5th Int. Conf. on Position-Sensitive Detectors. [43](#)
- [116] M. Lampton, O. Siegmund, and R. Raffanti. Delay line anodes for microchannel-plate spectrometers. *Review of Scientific Instruments*, 58(12):2298–2305, 1987. [43](#)
- [117] Richard N. Zare. Photoejection dynamics,. *Mol. Photochem*, 1972. [48](#)
- [118] Gordon H. Dunn. Franck—condon factors for the ionization of h2 and d2. *The Journal of Chemical Physics*, 44(7):2592–2594, 1966. [54](#), [64](#), [115](#)
- [119] G. R. Cook and P. H. Metzger. Photoionization and absorption cross sections of h2 and d2 in the vacuum ultraviolet region. *J. Opt. Soc. Am.*, 54(8):968–972, Aug 1964. [56](#)
- [120] D. Shiner, J. M. Gilligan, B. M. Cook, and W. Lichten. h₂, d₂, and hd ionization potentials by accurate calibration of several iodine lines. *Phys. Rev. A*, 47:4042–4045, May 1993. [54](#)
- [121] A. R. W. McKellar and T. Oka. A study of the electric quadrupole fundamental band of d2 using an infrared difference frequency laser system. *Canadian Journal of Physics*, 56(10):1315–1320, 1978. [54](#)

- [122] T. J. Reddish, A. Padmanabhan, M. A. MacDonald, L. Zuin, J. Fernández, A. Palacios, and F. Martín. Observation of interference between two distinct autoionizing states in dissociative photoionization of h_2 . *Phys. Rev. Lett.*, 108:023004, Jan 2012. [60](#)
- [123] Z. X. He, J. N. Cutler, S. H. Southworth, L. R. Hughey, and J. A. R. Samson. Zero kinetic energy proton and deuteron production from photoionization of h_2 and d_2 . *The Journal of Chemical Physics*, 103(10):3912–3916, 1995. [61](#), [70](#)
- [124] Kenji Ito, Richard I. Hall, and Masatoshi Ukai. Dissociative photoionization of h_2 and d_2 in the energy region of 25–45 eV. *The Journal of Chemical Physics*, 104(21):8449–8457, 1996. [61](#), [66](#), [67](#)
- [125] Jorge Fernández and Fernando Martín. Electron and ion angular distributions in resonant dissociative photoionization of h_2 and d_2 using linearly polarized light. *New Journal of Physics*, 11(4):043020, apr 2009. [61](#), [70](#), [87](#)
- [126] R Browning and J Fryar. Dissociative photoionization of h_2 and d_2 through the $1\sigma_g$ ionic state. *Journal of Physics B: Atomic and Molecular Physics*, 6(2):364–371, feb 1973. [61](#)
- [127] Andreas Fischer. *Dissociative Photoionization of Molecular Hydrogen - A Joint Experimental and Theoretical Study of the Electron-Electron Correlations induced by XUV Photoionization and Nuclear Dynamics on IR-Laser Dressed Transition States*. PhD thesis, Heidelberg University, 2015. An optional note. [63](#)
- [128] Noriyuki Kouchi, Masatoshi Ukai, and Yoshihiko Hatano. Dissociation dynamics of superexcited molecular hydrogen. *Journal of Physics B: Atomic, Molecular and Optical Physics*, 30(10):2319–2344, may 1997. [65](#)
- [129] I. Sánchez and F. Martín. Dissociative photoionization of h_2 and d_2 by (30–37)-eV photons via $^1\Pi_u$ states. *Phys. Rev. A*, 60:2200–2206, Sep 1999. [66](#)
- [130] A Lafosse, M Lebech, J C Brenot, P M Guyon, L Spielberger, O Jagutzki, J C Houver, and D Dowek. Molecular frame photoelectron angular distributions in dissociative photoionization of h_2 in the region of the q_1 and q_2 doubly excited states. *Journal of Physics B: Atomic, Molecular and Optical Physics*, 36(23):4683–4702, nov 2003. [66](#), [70](#)
- [131] I. Sánchez and F. Martín. Origin of unidentified structures in resonant dissociative photoionization of H_2 . *Phys. Rev. Lett.*, 79:1654–1657, Sep 1997. [66](#)
- [132] Y. M. Chung, E.-M. Lee, T. Masuoka, and James A. R. Samson. Dissociative photoionization of h_2 from 18 to 124 eV. *The Journal of Chemical Physics*, 99(2):885–889, 1993. [66](#)
- [133] I. Sánchez and F. Martín. The doubly excited states of the h_2 molecule. *The Journal of Chemical Physics*, 106(18):7720–7730, 1997. [66](#), [70](#), [125](#)

- [134] Andreas Fischer, Alexander Sperl, Philipp Cörlin, Michael Schönwald, Sebastian Meuren, Joachim Ullrich, Thomas Pfeifer, Robert Moshhammer, and Arne Senfleben. Measurement of the autoionization lifetime of the energetically lowest doubly excited state in H_2 using electron ejection asymmetry. *Journal of Physics B: Atomic, Molecular and Optical Physics*, 47(2):021001, dec 2013. [66](#)
- [135] J. F. Pérez-Torres, F. Morales, J. L. Sanz-Vicario, and F. Martín. Asymmetric electron angular distributions in resonant dissociative photoionization of H_2 with ultrashort xuv pulses. *Phys. Rev. A*, 80:011402, Jul 2009. [70](#)
- [136] F. Kelkensberg, C. Lefebvre, W. Siu, O. Ghafur, T. T. Nguyen-Dang, O. Atabek, A. Keller, V. Serov, P. Johnsson, M. Swoboda, T. Remetter, A. L’Huillier, S. Zherebtsov, G. Sansone, E. Benedetti, F. Ferrari, M. Nisoli, F. Lépine, M. F. Kling, and M. J. J. Vrakking. Molecular dissociative ionization and wave-packet dynamics studied using two-color xuv and ir pump-probe spectroscopy. *Phys. Rev. Lett.*, 103:123005, Sep 2009. [70](#)
- [137] A. Rudenko, Th. Ergler, B. Feuerstein, K. Zrost, C.D. Schröter, R. Moshhammer, and J. Ullrich. Real-time observation of vibrational revival in the fastest molecular system. *Chemical Physics*, 329(1):193 – 202, 2006. Electron Correlation and Multi-mode Dynamics in Molecules. [70](#)
- [138] K. Sändig, H. Figger, and T. W. Hänsch. Dissociation dynamics of H_2^+ in intense laser fields: Investigation of photofragments from single vibrational levels. *Phys. Rev. Lett.*, 85:4876–4879, Dec 2000. [73](#), [75](#)
- [139] Vaibhav S. Prabhudesai, Uri Lev, Adi Natan, Barry D. Bruner, Adi Diner, Oded Heber, Daniel Strasser, D. Schwalm, Itzik Ben-Itzhak, J. J. Hua, B. D. Esry, Yaron Silberberg, and Daniel Zajfman. Tracing the photodissociation probability of H_2^+ in intense fields using chirped laser pulses. *Phys. Rev. A*, 81:023401, Feb 2010. [75](#)
- [140] Adi Natan, Uri Lev, Vaibhav S. Prabhudesai, Barry D. Bruner, Daniel Strasser, Dirk Schwalm, Itzik Ben-Itzhak, Oded Heber, Daniel Zajfman, and Yaron Silberberg. Quantum control of photodissociation by manipulation of bond softening. *Phys. Rev. A*, 86:043418, Oct 2012. [75](#)
- [141] Renate Pazourek, Stefan Nagele, and Joachim Burgdörfer. Attosecond chronoscopy of photoemission. *Rev. Mod. Phys.*, 87:765–802, Aug 2015. [78](#)
- [142] Lukas Medišauskas, Roger Y Bello, Alicia Palacios, Alberto González-Castrillo, Felipe Morales, Lev Plimak, Olga Smirnova, Fernando Martín, and Misha Yu Ivanov. A molecular clock for autoionization decay. *Journal of Physics B: Atomic, Molecular and Optical Physics*, 50(14):144001, jun 2017. [82](#)
- [143] U. Fano. Effects of configuration interaction on intensities and phase shifts. *Phys. Rev.*, 124:1866–1878, Dec 1961. [82](#)

- [144] J N Bardsley. Configuration interaction in the continuum states of molecules. *Journal of Physics B: Atomic and Molecular Physics*, 1(3):349–364, may 1968. [82](#)
- [145] Alicia Palacios, Johannes Feist, Alberto González-Castrillo, José Luis Sanz-Vicario, and Fernando Martín. Autoionization of molecular hydrogen: Where do the fano lineshapes go? *ChemPhysChem*, 14(7):1456–1463, 2013. [82](#)
- [146] Lukas Medišauskas, Felipe Morales, Alicia Palacios, Alberto González-Castrillo, Lev Plimak, Olga Smirnova, Fernando Martín, and Misha Yu Ivanov. Signatures of attosecond electronic–nuclear dynamics in the one-photon ionization of molecular hydrogen: analytical model versus ab initio calculations. *New Journal of Physics*, 17(5):053011, may 2015. [82](#)
- [147] Andreas Fischer, Alexander Sperl, Philipp Cörlin, Michael Schönwald, Helga Rietz, Alicia Palacios, Alberto González-Castrillo, Fernando Martín, Thomas Pfeifer, Joachim Ullrich, Arne Senftleben, and Robert Moshhammer. Electron localization involving doubly excited states in broadband extreme ultraviolet ionization of h_2 . *Phys. Rev. Lett.*, 110:213002, May 2013. [98](#)
- [148] Manuel Kremer, Bettina Fischer, Bernold Feuerstein, Vitor L. B. de Jesus, Vandana Sharma, Christian Hofrichter, Artem Rudenko, Uwe Thumm, Claus Dieter Schröter, Robert Moshhammer, and Joachim Ullrich. Electron localization in molecular fragmentation of h_2 by carrier-envelope phase stabilized laser pulses. *Phys. Rev. Lett.*, 103:213003, Nov 2009. [105](#)
- [149] Stanley Cohen, John R. Hiskes, and Robert J. Riddell. Vibrational states of the hydrogen molecular ion. *Phys. Rev.*, 119:1025–1027, Aug 1960. [114](#)
- [150] Friedrich von Busch and Gordon H. Dunn. Photodissociation of h_2^+ and d_2^+ : Experiment. *Phys. Rev. A*, 5:1726–1743, Apr 1972. [114](#), [115](#)
- [151] I. Sánchez and F. Martín. Doubly excited autoionizing states of h_2 above the second ionization threshold: the q_2 resonance series. *The Journal of Chemical Physics*, 110(14):6702–6713, 1999. [125](#)

Acknowledgement

I would like to express my deepest gratitude to you, Robert, for everything. This thesis wouldn't have been possible without your support. What I enjoyed the most during all these years is your logic and approach regarding physics related topics as well as general ones in life, the way you try to simplify most complex problems, your encouraging optimism, more importantly your kindness and endless patience even with my most naïve and stupid questions. I was always impressed by your intellectual abilities and skills in and outside the lab. You gave me the complete freedom during my PhD and the chance to have the most fruitful years of my life.

I am deeply grateful to you, Thomas, firstly, for introducing me to your division at MPIK, for your insightful discussion and mentoring in all these years. Your enthusiasm is exceptional. Even with your extremely busy schedule you always found time for interesting scientific discussions.

Claus Dieter, you were always extremely kind to me. I'll never forget you saying "nicht übertreiben!" every day late in the evening. Thanks a lot for all your support, particularly when I was working in the lab. I learned a great deal from you.

Andreas Wolf, thanks a lot for accepting to become my examiner.

Anne you supported me enormously in and outside the lab. I'm extremely grateful for the time and effort you put into proofreading my thesis.

Hem, I would like to thank you endlessly for your support in the lab in all these years. The state of this project would not be here if it was not for you.

Thanks a lot Daniel for proofreading and support. My special thanks goes also to you, Ferrydoon, for your limitless kindness and support. Patrick, thanks a lot for all the discussion and your help during this project, as well as correcting my thesis.

I would also thank all my colleagues at MPIK, Severin Meister, Frans Schotch, Hannes Lindenblatt, Patrizia Schoch, Christian Ott, Alexander von der Dellen, Divya Bharti, Christian Kaiser, Nickola Camus, and Nikkola Molov.

I would also like to thank all people in different sections of the MPIK, such as, electronics, mechanical workshop.